Self-Assembled Biomimetic Conductive Fibers as a Novel Functional Materials Platform

Allon Hochbaum
UNIVERSITY OF CALIFORNIA IRVINE

06/28/2019
Final Report

REPORT DOCUMENTATION PAGE

Form Approved
OMB No. 0704-0188

The public reporting burden for this collection of information is estimated to average 1 hour per response, including the time for reviewing instructions, searching existing data sources, gathering and maintaining the data needed, and completing and reviewing the collection of information. Send comments regarding this burden estimate or any other aspect of this collection of information, including suggestions for reducing the burden, to Department of Defense, Washington Headquarters Services, Directorate for Information Operations and Reports (0704-0188), 1215 Jefferson Davis Highway, Suite 1204, Arlington, VA 22202-4302. Respondents should be aware that notwithstanding any other provision of law, no person shall be subject to any penalty for failing to comply with a collection of information if it does not display a currently valid OMB control number.
PLEASE DO NOT RETURN YOUR FORM TO THE ABOVE ADDRESS.

1. REPORT DATE *(DD-MM-YYYY)*	2. REPORT TYPE	3. DATES COVERED *(From - To)*
06-18-2019	Final	9/15/2014-3/14/2018

4. TITLE AND SUBTITLE	5a. CONTRACT NUMBER

Self-Assembled Biomimetic Conductive Fibers as a Novel Functional Materials Platform

5b. GRANT NUMBER

FA9550-14-1-0350

5c. PROGRAM ELEMENT NUMBER

6. AUTHOR(S)

Allon Hochbaum

5d. PROJECT NUMBER

5e. TASK NUMBER

5f. WORK UNIT NUMBER

7. PERFORMING ORGANIZATION NAME(S) AND ADDRESS(ES)

The Regents of the University of California, Irvine
141 Innovation Drive, Suite 250
Irvine, CA 92697-7600

8. PERFORMING ORGANIZATION REPORT NUMBER

FA9550-14-1-0350

9. SPONSORING/MONITORING AGENCY NAME(S) AND ADDRESS(ES)

Air Force Office of Science and Research
875 Randolph Street
Suite 325 Room 3112
Arlington, VA 22203

10. SPONSOR/MONITOR'S ACRONYM(S)

AFOSR

11. SPONSOR/MONITOR'S REPORT NUMBER(S)

12. DISTRIBUTION/AVAILABILITY STATEMENT

Approved for Public Release; Distribution is Unlimited.

13. SUPPLEMENTARY NOTES

14. ABSTRACT

Electronic transport is conventionally the domain of man-made materials and devices, but anaerobic respiration by some sediment microbes requires shuttling electrons from the cell to remote electron acceptors. The model bacterium Geobacter sulfurreducens produces electrically conductive, protein fiber appendages, representing a new class of materials with electronic properties at the intersection of intermolecular electron transfer and solid-state electron transport physics. These materials also serve as natural inspiration for new bioelectronics interface materials. Based on fundamental differences

15. SUBJECT TERMS

Conductivity, protein nanostructures, biomolecules, supramolecular, self-assembly, enzymatic catalysis

16. SECURITY CLASSIFICATION OF:			17. LIMITATION OF ABSTRACT	18. NUMBER OF PAGES	19a. NAME OF RESPONSIBLE PERSON
a. REPORT	b. ABSTRACT	c. THIS PAGE	UU		Allon Hochbaum
unclassified	unclassified	unclassified		107	**19b. TELEPHONE NUMBER** *(Include area code)* 949-824-1194

DISTRIBUTION A: Distribution approved for public release

Standard Form 298 (Rev. 8/98)
Prescribed by ANSI Std. Z39.18

AFOSR Young Investigator Program

FINAL REPORT

Program: Natural Materials, Systems, and Extremophiles
Program Managers: Dr. Hugh C. DeLong, Dr. J. Aura Gimm

Grant number: FA9550-14-1-0350

Self-Assembled Biomimetic Conductive Fibers as a Novel Functional Materials Platform

Prof. Allon Hochbaum

University of California, Irvine
Department of Materials Science and Engineering
Department of Chemistry

CONTENTS:

PROJECT SUMMARY

Electronic transport is conventionally the domain of man-made materials and devices, but anaerobic respiration by some sediment microbes requires shuttling electrons from the cell to remote electron acceptors. The model bacterium *Geobacter sulfurreducens* produces electrically conductive, protein fiber appendages, representing a new class of materials with electronic properties at the intersection of intermolecular electron transfer and solid-state electron transport physics. These materials also serve as natural inspiration for new bioelectronics interface materials. Based on fundamental differences between the protein building blocks of these assemblies and the canonical building blocks of inorganic and organic conductors and semiconductors, it is clear that Nature has developed its own design principles for long-range electronic conducting systems. The biomolecular identity and supramolecular order underpinning biological conductive materials are poorly understood, as are the mechanisms by which these structures support electron transport. This report summarizes research in the Hochbaum lab funded by the AFOSR YIP on the characterization of charge transport mechanisms and structure-property relationships in conductive protein nanowires. These efforts establish distinctive biomolecular design principles for long-range electron transport in self-assembling peptide nanofibers and native bacterial appendages. Such materials serve as an experimental platform to understand long-range charge transport in biological materials in general, and as promising technological platforms for bioelectronic interfaces.

PROJECT OBJECTIVES:

Objective 1: To characterize the electronic conductivity of bacterial protein filaments in natural environments and to establish a mechanism for their unique electronic transport properties.

Objective 2: To characterize structure-property relationships for conductive protein fibers and synthetic, supramolecular biomaterials.

Objective 3: To construct hybrid biotic-abiotic interfaces based on protein and synthetic peptide nanofibers.

OVERVIEW OF PROJECT FINDINGS:

Overview of Objective 1 findings: Protein appendages from *G. sulfurreducens* are electronically conductive. However, the mechanism of electronic charge conduction in *G. sulfurreducens* filaments is disputed in the literature, and as of the initiation of this project there was no atomic-resolution structure of these filaments, precluding transport mechanism insights. The main findings of research efforts under Objective 1 were:

(*1*) Purified protein appendages from *G. sulfurreducens* are electronically conductive under physiologically-relevant conditions and that the conductivity is ohmic, meaning that charge carriers appear to transport through the filaments as they do in metallic abiotic materials.

(*2*) While the conductive *G. sulfurreducens* filaments were thought to be type IV pili, a common bacterial appendage conserved across many species, cryo-electron microscopy (cryoEM) data shows that they are in fact polymerized cytochromes, iron-porphyrin (heme) containing enzyme filaments. These structures are unprecedented in biology and the resulting one-dimensional chaining of heme along the filament axis provides a molecular structure basis for understanding charge transport in these filaments.

Overview of Objective 2 findings: While the biosynthetic self-assembly mechanism of bacterial cytochrome filaments is yet unknown, we designed metal-free synthetic peptides to arrange redox-active amino acid side-chains in long range periodic sequences. The main findings of research efforts under Objective 2 were:

(*1*) Self-assembling peptide fibers based on α-helical coiled-coil oligomers can also be designed to exhibit electronic conductivity. These fibers are more conductive than the bacterial filaments, are similarly ohmic in transport behavior, and lack metal species.

(*2*) Our structural characterization of both the conductive bacterial cytochrome filaments and the synthetic peptide fibers suggests that, while not inherently conductive themselves, proteins can precisely position degenerate redox species in closely spaced, long-range periodic arrangements that facilitate charge transport.

Overview of Objective 3 findings: We constructed bioelectronic interfaces for enzymatic electrocatalysis from laccase immobilized on synthetic conducting peptide nanofibers. Charge transport was characterized through peptide nanofiber mats and between nanofibers and laccase reaction sites. The main findings of research efforts under Objective 3 were:

(*1*) Conductive synthetic peptide nanofibers can serve as direct electron transfer scaffolds for electron transfer to/from electrocatalytic enzyme reaction sites. Nanofiber-decorated electrodes show increased electroactive surface area, confirming inherent electronic conductivity measurements by other methods in Obj. 2, and read out electronic signals as a result of the biochemical activity of immobilized laccase enzyme.

(*2*) Constructed completely from amino acids, the peptide nanofibers and laccase enzyme are components that can in principle be expressed in engineered organisms, establishing a critical step toward bio-manufactured circuits.

PROJECT FINDINGS:

Objective 1: Assembly and Transport Characterization of Conductive Bacterial Appendages
Status: COMPLETE (pivot)

The original objective proposed to study conductive *G. sulfurreducens* pili by acellular self-assembly of the recombinantly expressed and purified pilin building block protein PilA (objective 1.1), recombinant expression and biosynthetic assembly of PilA in a suitable host (objective 1.2), and the development of electronic transport characterization methods for such supramolecular protein materials (objective 1.3).

The originally planned objectives 1.1 and 1.2 were unsuccessful – there was no evident self-assembly of purified recombinant PilA into homogeneous fiber structures, and the type IV pilus biosynthetic machinery in several host strains was not as promiscuous to variations in PilA sequence as several literature studies had suggested. Both of these results attest to the complexity of the type IV pilus biosynthetic mechanism, which, while generally conserved across many species of bacteria, is required for the proper assembly of pilins like PilA and is sensitive to subtle sequence variations of the PilA building blocks. Objective 1.3 was successful, in which we developed several methods for the property characterization of the purified native bacterial fibers. These methods are uniquely suited to study the electronic transport properties of supramolecular biomaterials, in which the hydrated state of the material is critical to deriving structure-property relationships of electronic conductivity. Consequently, these techniques were also used in several collaborations we initiated with other groups studying electronic properties of biomolecular materials. See Chapter 1 for details of these characterization methods and Chapter 7 for descriptions of these collaborations.

As part of objectives 1.1 and 1.2, we tried to determine the atomic structure of *G. sulfurreducens* protein appendages to better understand the structural and chemical underpinnings of their transport properties. In the course of these efforts, we found that the conductive appendages of *G. sulfurreducens* are likely not type IV pili at all, but rather a unique and novel structure of polymerized iron porphyrin (heme) containing proteins, called cytochromes. Not only are these unprecedented structures in biology as a whole, but they also provide a new understanding of the structural basis for conductivity in *G. sulfurreducens* appendages, namely by electron hopping between heme sites. In addition, our transport characterization of these protein fibers from objective 1.3 indicated band-like electronic conduction, which is not readily explained by the heme arrangement within the cytochrome polymers. Rather, conduction in these materials represents an interesting intersection of short range electron transfer theory and long range condensed matter transport theory. Details of the cytochrome polymer structure are in Chapter 2.

To create synthetic conductive protein fibers, we pivoted objectives 1.1 and 1.2 to focus on self-assembling *de novo* peptides – chemically synthesized short amino acid sequences. We designed the peptides to self-assemble into one-dimensional fibers based on well-understood coiled coil interactions, whereby hydrophobic interfaces of α-helical coils aggregate in an

ordered manner in aqueous buffer. Before our discovery of the cytochrome wire appendages, the prevailing theory of electron transport in *G. sulfurreducens* appendages was through close packing of aromatic amino acid side chains. Taking inspiration from these structures, we incorporated aromatic phenylalanine residues into the hydrophobic interface of our coiled coil peptides. The designed peptides self-assembled into defined coiled-coil aggregates – antiparallel hexamers (ACC-Hex), the first report of such symmetry structures in both natural protein structures and other *de novo* designed peptide oligomers (Chapter 3). These peptides assembled into homogeneous fibers that exhibited conductive properties. Because of their defined oligomeric building blocks, we know the structure of these fibers with high confidence, from X-ray crystal structures and solution structure characterization by chromatography and small-angle X-ray scattering, and they appeared promising for further structure-property relationship studies. Consequently, these peptide fibers were used in place of the *G. sulfurreducens* appendages for the remainder of the project.

Objective 2: Structure-Property Relationships in Conductive Protein Fibers
Status: COMPLETE

The conductive peptide fibers generated as part of objective 1 served as platforms for studying the determinants of electronic conductivity in natural proteinogenic materials. Instead of the genetic methods of amino acid residue mutation originally proposed in objectives 2.1 and 2.2, the *de novo* peptides are easily mutated by altering the identity or sequence of amino acids incorporated into the peptides during solid-phase peptide synthesis. By mutating various amino acids with side chains involved in the hydrophobic interactions at the ACC-Hex core or on the polar, solvent-exposed surface of the ACC-Hex structure, we developed an in-depth chemical understanding of the nature and stability of peptides assembling into the ACC-Hex structure (Chapter 4). The interactions leading to the peptide oligomerization, the phenylalanine-isoleucine (Phe-Ile) zipper, are novel and without precedent in natural or designed proteins. Moreover, mutation of both the interior and exterior residues result in tunable stability of the ACC-Hex structure from peptides variants that fail to form ACC-Hex (unstable) to peptides that result in ACC-Hex with some of the greatest thermodynamic stabilities of any natural or designed protein aggregates on a molecular weight basis. These mutagenic studies demonstrated the generality of the Phe-Ile zipper motif in driving oligomer self-assembly and established it as an appropriate scaffold for protein scaffold design.

Using many of the same methods developed in objective 1 to measure transport properties of biological supramolecular materials, we characterized the electronic conductivity of fibers formed from ACC-Hex building blocks (objective 2.3). Not only were the resulting fibers electrically conductive, but they were an order of magnitude more conductive than the purified *G. sulfurreducens* appendages (Chapter 5). The conductivity results are significant for several reasons. First, they demonstrate metallic-like electronic conductivity in a supramolecular protein material. Previously published studies showed semiconducting behavior in dipeptide crystals or extremely poor conductivity in protein filaments, such as amyloid fibers. Second, the peptide fibers exhibited conductivity despite lacking metals and porphyrin components apparently required for conductivity in the *G. sulfurreducens* cytochrome wires. These structural differences suggest distinct mechanisms by which protein supramolecular materials can mediate significant electronic conductivity in biological systems. Lastly, spectroscopic and structural data of the

ACC-Hex building blocks indicate that the aromatic side chains of the Phe residues in the hydrophobic core are not π-stacked, meaning that explicit orbital overlap is not necessary to produce protein materials that exhibit metallic-like conduction properties.

While we originally planned to mutate various residues in the peptide sequence to study the effects of side chain substitutions on electronic conductivity (objective 1.2), these mutations caused defective assembly of the fiber morphology even though they resulted in structurally identical ACC-Hex building blocks in aqueous buffer. We do not yet understand why relatively minor mutations, for example Phe->para-fluorophenylalanine (a single H to F substitution), inhibits fiber formation, but these studies, and the development of fibrilization strategies that are more robust to mutation, are part of ongoing research in the lab.

Objective 3: Conductive Protein Fibers as Electrocatalytic Enzyme Scaffolds
Status: COMPLETE (pivot)

The original goal of objective 3 was to incorporate a hydrogenase from *Clostridium acetobutylicum* onto conductive protein fiber scaffolds and demonstrate electrocatalytic hydrogen production. Due to the low yield and extreme air sensitivity of the proposed hydrogenase, and hydrogenases in general, we pivoted to focus on electrocatalytic interfaces with more easily manageable enzymes. We chose laccases, electrocatalytic enzymes that oxidize phenolic compounds and are commercially available, air stable, and the electrochemical properties of which have been studied extensively. Instead of the cloning, expression, and maturation of a hydrogenase (objectives 3.1, 3.2 and 3.3), purified laccase from the fungus *Trametes versicolor* was immobilized by physical adsorption (objective 3.4) or chemical cross-linking (objective 3.5) onto films of conductive peptide fibers. Fibers without the laccase were shown to dramatically increase the electroactive surface area of glassy carbon electrodes, a definitive validation of their conductive properties and demonstration as reversible redox scaffolds. With the immobilized laccase, these fibers accomplished direct electron transfer from the enzyme in the presence of phenolic compounds, such as catechol. These studies, described in detail in Chapter 6, showed that our peptide fibers could be used to electrocatalytically sense or actuate chemical transformations (objective 3.5) in electrochemical cells. Moreover, this electrocatalysis was accomplished with components made from proteinogenic amino acids, suggesting that such biological circuits can be made autonomously from engineered organisms.

CHAPTER 1:

Mechanism of Electronic Conductivity of *Geobacter sulfurreducens* Appendages

1.1 SUMMARY

The bacterium *Geobacter sulfurreducens* is a model biological catalyst in microbial electrochemical devices. *G. sulfurreducens* forms electrically conductive, electrode-associated biofilms, but the biological structures mediating electrical conduction from cells to the electrodes are a matter of debate. Bacteria in these communities produce a network of fiber-like Type IV pili, which have been proposed to act either as inherent, protein-based electronic conductors, or as electronically inert scaffolds for cytochromes mediating long-range charge transport. Previous studies have examined pilus conduction mechanisms under vacuum and in dry conditions, but their conduction mechanism under the physiologically relevant conditions has yet to be characterized. In this work, we isolate *G. sulfurreducens* pili, and compare the electronic conduction mechanism of both live biofilms and purified pili networks under dry and aqueous conditions. Solid-state *I-V* characteristics indicate that electronic transport in films of purified pili is representative of conduction in a fiber percolation network. Electrochemical gating measurements in a bipotentiostat device configuration confirm previous results suggesting redox currents dominate live biofilm conduction. Purified pili films, however, exhibit non-redox electronic conduction under aqueous, buffered conditions, and their conductivity increases with decreasing temperature. These findings show that isolated pili possess inherent, non-redox-mediated conductivity consistent with a metallic-like model of charge carrier transport. The results demonstrate an experimental platform for studying electronic transport in biomaterials and suggest that pili serve as an exemplary model for designing bioelectronic interfaces.

1.2 INTRODUCTION

Electronic charge transport in biological molecules, from DNA to photosynthetic enzymes, typically follows a donor-bridge-acceptor model[1–4]. In this model, electrons either tunnel through the molecule over nanometer distances or use thermally-activated hopping to traverse longer distances, using active sites such as immobilized redox cofactors [5,6]. The maximum length scales for redox-mediated, biological electron transport have been expanded since the discovery of electronic conduction over microns to centimeters in communities of anaerobic sediment microbes [7–9]. One such bacterium, *Geobacter sulfurreducens*, has been extensively studied for its production of Type IV pili, a class of filamentous protein appendages, required for long-range electron transport in the environment. While nanowires produced by other sediment microbes, such as *Shewenella oneidensis,* have demonstrated long-range conductivity via redox-activated cytochrome hopping [10], pili purified from *G. sulfurreducens* exhibit temperature dependent transport inconsistent with thermally-activated hopping [11], suggesting a novel paradigm for long-range biological electronic transport.

 Structural homology models suggest that the peptide monomer of pili, PilA, has aromatic residues that cluster to from conduction conduits when assembled into the molecular wire [12–15,15]. Electronic conduction in pili occurs over several micrometers, a length-scale comparable to those observed for thermally activated redox hopping in biological systems [5] but mechanistically distinct. In contrast to the hopping mechanism, the individual pili [16] and dry pili films [11] exhibit a

metallic-like temperature-dependence [13]. Claims of metallic-like transport have been contested for several reasons [17]. Firstly, the crystal structure of the intact pilus has not been determined to verify the aromatic clustering hypothesis. Rather, the conductive contribution of aromatics has been suggested by deletion experiments, where the removal of aromatic residues from PilA lead to a decrease in current production of electrode-associated communities [18]. However, homology-based structural models present conflicting results regarding the possibility and spacing of aromatic residue overlap, and several studies imply that delocalized electron transport through the aromatics is unlikely [12–15,19,15,20,21].

Secondly, although pili have been implicated in current production in *G. sulfurreducens* biofilms thicker than 10 μm [22], measurements of electronic transport through biofilm are dominated by faradaic currents at the redox potentials of biofilm-associated cytochromes, as opposed to the linear response expected metallic-like electronic transport models [23–25]. Lastly, biofilms oxidize the electron donor acetate at a finite rate and grow to a thickness limited by the rate of electron transfer between cytochromes, consistent with the idea that these redox active proteins mediate charge transport [26]. Regardless, the contributions of *G. sulfurreducens* cytochromes, which localize along the pilus, have not been conclusively separated from pili conductivity measurements [27]. Further insights into the conduction mechanism of extracted pili in conditions resembling the environment of the live biofilm would provide several key theoretical contributions in addition to potential design principles for technological applications. If pili exhibit metallic-like conductivity, in which charge carriers behave as classical point charges, they defy the standard donor-bridge-acceptor model and suggest the need for a better understanding of long-range biological electron transport [11,13]. As a biological material with electronically conductive properties, these protein wires may function as useful bioelectronics interface materials.

In this study, we isolate native *G. sulfurreducens* pili by salt precipitation of pili from culture supernatants and cast pili films onto solid-state and electrochemical transport devices for the characterization of their electronic properties. Solid-state measurements indicate that pili mats are conducting percolation networks orders of magnitude more conductive than globular protein, *Pseudomonas aeruginosa* pili films, and amyloid-β (Aβ) fiber film controls. Distinct from previous measurements on *G. sulfurreducens* pili [11,28], our electrochemical measurements are performed in a bipotentiostat configuration with controlled, reference gating of the electrode potentials [25,29,30]. These measurements show that purified pili films exhibit conductivity independent of electrochemical gating potential, and an inverse relationship between temperature and conductivity in aqueous conditions, further supporting a metallic-like rather than cytochrome-mediated charge transport mechanism.

1.3 RESULTS
1.3.1 Analytical characterization of purified *G. sulfurreducens* appendages:
Native pili from *G. sulfurreducens* cultures were isolated from supernatant using a modified magnesium chloride precipitation protocol. Purified pili were then spin cast onto silicon wafers for imaging or onto interdigitated electrodes for electronic characterization and subsequent imaging. The atomic force microscope (AFM) image in Fig 1*A* shows the typical morphology of intact pili fibers in the purified product. Height profile measurements from small area scans (Fig 1*B*) reveal that the fibers are approximately 4-6 nm in diameter, consistent with previous findings [31] and existing homology models [14,15,19,32]. The globular debris may be aggregated

pilins, cytochromes, or non-proteinaceous cell material that is not detected by the analytical methods discussed below.
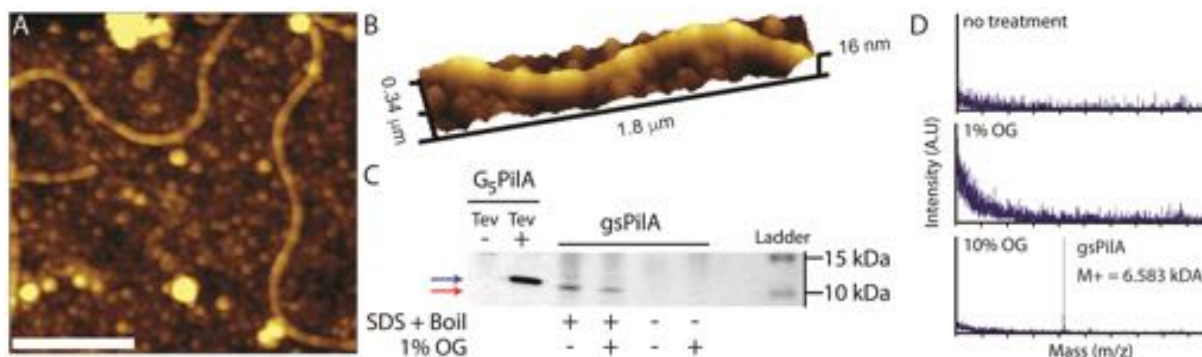
Figure. 1. Imaging and molecular analysis of purified *G. sulfurreducens* pili. (*A*) Plan and (*B*) perspective view AFM images of isolated pili. (*C*) SDS-PAGE gel of purified pili under different denaturation conditions. Red and blue arrows indicate the migration height of gsPilA and the engineered pilin, G$_5$PilA, respectively. G$_5$PilA is appended to a solubility and affinity tag until cleavage by TEV protease. (*D*) MALDI-TOF spectra of purified pili under non-denaturing (no treatment, 1% OG) and denaturing (10% OG, diluted to 1% prior to MALDI analysis) conditions. gsPilA appears at the expected m/z = 6.5 kDa for the singly charged species. Scale bar in (*A*) is 1 μm.

Polyacrylamide gel electrophoretic separation (SDS-PAGE) was used to identify the major protein component of purified *G. sulfurreducens* pili preparations. *G. sulfurreducens* pili are resistant to routine denaturing conditions, but they disassemble into their constituent pilin protein building blocks after extended boiling in aqueous sodium-dodecyl sulfate (SDS) or incubation in sufficiently high concentrations of octyl β-D glucopyranoside (OG) [33]. The major pilin component of *G. sulfurreducens* pili, PilA (gsPilA), migrates through the gel after pilus denaturation. gsPilA runs higher on the gel relative to its expected 6.5 kDa molecular weight (Fig 1*C*), possibly due to retention of its α-helical secondary structure in the low SDS concentration running buffer. To help identify gsPilA in the pili extract from silver stained gels, an engineered pilin standard (G$_5$PilA) with the mature (secreted) gsPilA sequence and a Gly$_5$ C-terminal spacer was expressed, purified, and separated from its solubility and affinity tags at a TEV protease cleavage site. gsPilA from purified pili aliquots subjected to different denaturing conditions runs at a similar height to the engineered pilin after cleavage by TEV protease (Fig 1*C*). gsPilA bands migrate through the gels just below the G$_5$PilA band, commensurate with the added molecular weight of the Gly$_5$ spacer in the engineered pilin.

The molecular weight of gsPilA in the intact pili was confirmed by matrix-assisted laser desorption/ionization time-of-flight (MALDI-TOF) mass spectrometry. Mass spectra of the pili extracts were collected from samples without denaturation treatment (Fig 1*D, Top*), exposed to 1% OG (Fig 1*D, Middle*), and exposed to 10% OG diluted to 1% before casting on the MALDI plate (Fig 1*D, Bottom*). gsPilA appears in the mass spectrum near the expected 6572 m/z [14] of the singly charged species only when the purified pili were denatured with 10% OG [33]. The dilution of the 10% OG denatured pili solutions to a final OG concentration of 1% was necessary to prevent signal interference caused by the denaturant. Consistent with findings in our SDS-PAGE gel analysis (Fig 1*C*), 1% OG alone is not enough to denature pili into gsPilA monomers (Fig 1*D, Middle*). The presence of gsPilA in OG denatured pili samples was confirmed by protein sequencing via LC-MS/MS after a tryptic digest.

1.3.2 Solid-state I-V characterization of conductive *G. sulfurreducens* appendages:

Pili films spun coat onto interdigitated electrode devices showed a resistance of 470 Ω at an applied bias of ± 0.8 V, with linear current response throughout the applied voltage range. These films were four orders of magnitude more conductive than an equivalent amount of the globular protein bovine serum albumin (BSA), six orders of magnitude more conductive than cell-free growth media (NBAF) processed in an identical manner to the pili, and seven orders of magnitude more conductive than fibers of amyloid β (Aβ)-forming peptides [34] (Fig 2*A*). *G. sulfurreducens* pili are five orders of magnitude more conductive than Type IV pili purified from *P. aeruginosa* strain PAO1, which have previously been demonstrated to be non-conductive [18]. Pili in the device channel had diameters ranged from 4-6 nm, as determined by height profiles of AFM micrographs, and an average length of 4.57 ± 0.26 μm.

Pili film conduction was measured as a function of interdigitated electrode spacing (Fig. 2*B*). Identical films were spun coat onto devices with the inter-electrode spacing ranging from 5 to 35 μm. The reduced channel dimension on the independent axis, L/w, is the electrode separation normalized to the width of the channel. The upper and lower bounds for hypothetical continuous film conduction are shown by the red and black traces in Fig 2*B*. The upper limit (red) was obtained by extrapolating the conductivity of the most conductive measurement to the normalized conductance across all L/w, assuming a continuous film conduction channel. The lower limit (black) was determined in a similar manner, extrapolating the conductivity of the least conductive measurement to all L/w, assuming a continuous film conduction channel. The experimental data does not follow the conductivity trend of either the red or black curve. Rather, it transitions between the upper and lower limits as the reduced channel dimensions increase. The dashed black line represents a percolation network conduction model fit to the experimental data, as described in the discussion below.
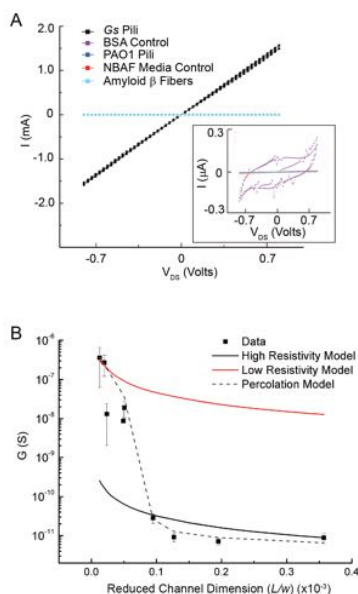
Figure. 2. Solid state electronic transport characterization of purified *G sulfurreducens* pili films. (*A*) *I-V* characteristics of *G. sulfurreducens* pili films and controls. Inset shows the low current *I-V* characteristics of the control films. *P. aeruginosa* (PA01) pili, NBAF, and Aβ fibers are overlapping near-baseline data in the main panel and inset. (*B*) The conductance of pili films in solid state devices varies with reduced channel dimensions. The solid lines model the behavior of the higher (red) and lower (black) limits for continuous film conduction, extrapolated from the high and low conductance values of the pili film at the reduced channel dimension extremes.

1.3.3 Electrochemical transport measurements of *G. sulfurreducens* conductive appendages:

Electrochemical measurements were conducted with a bipotentiostat gated cyclic voltammetry (CV) setup previously used to demonstrate redox-mediated charge transport in *G. sulfurreducens* biofilms [23,25,29]. The measurement setup sweeps the global (gate) potential of both source and drain electrodes relative to the reference at a fixed potential offset between source and drain. Using this setup, we analyzed the current response from a live *G. sulfurreducens* biofilm (Fig. 3*A*) and three distinct conduction controls: a solution of the soluble redox couple potassium ferro-/ferricyanide (Fig. 3*B*), a redox-active conducting polymer film of polyvinylferrocene (PVF) (Fig. 3*C*), and an ohmic, band-like conducting polymer film of PEDOT:PSS (Fig. 3*D*). The redox-active potassium ferricyanide and PVF film exhibit characteristic faradaic current responses to swept gate potential, similar to those observed in the *G. sulfurreducens* biofilm, where conduction across the device manifests as distinct reduction and oxidation peaks dependent on the value of the swept gate potential. The band-like conductor, PEDOT:PSS, however, shows a current response that is independent of the gate potential but whose magnitude is dependent on the difference between source and drain electrode potentials, V_{DS}, signifying at non-redox-mediated conduction. Bipotentiostat measurements of purified *G. sulfurreducens* pili films show a similarly featureless source-drain current, I_{DS}, that is devoid of the redox peaks associated with cytochrome-mediated charge transfer and is only dependent on V_{DS} (Fig. 4*A*). These constant current features are observed in water at neutral pH and at pH 4.0, at which cytochromes should be denatured [35].
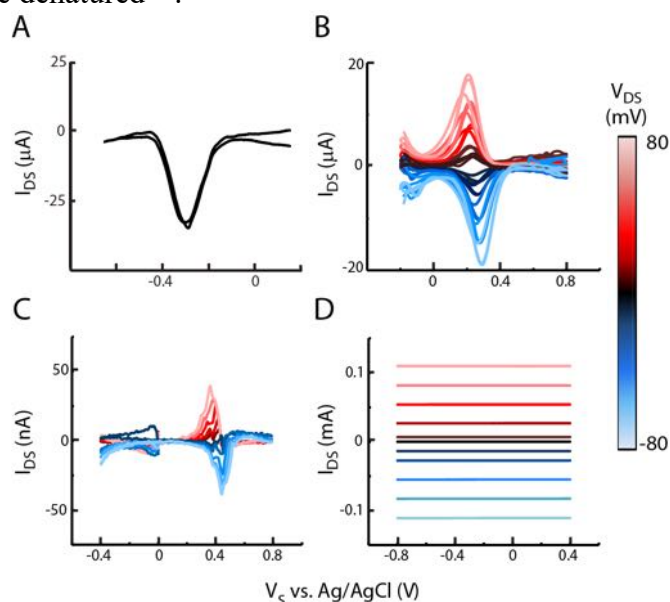
Figure. 3. Electrochemical transfer characteristics of a live *G. sulfurreducens* biofilm and abiotic controls. The source electrode potential is swept relative to the reference electrode at different V_{DS} values according to the color scale at the right. (*A*) Total source-drain current of a live *G. sulfurreducens* biofilm channel, at V_{DS} = 10 mV, shows prominent redox peak as a function of gate voltage, V_S. (*B*) A solution redox mediator, $K_3[Fe(CN)_6]$, and (*C*) a solid state, thin film redox conductor, PVF, exhibit similar faradaic current responses. (*D*) A solid state, thin film band conductor, PEDOT:PSS, shows the current response of an ohmic conduction channel in the bipotentiostat devices. Electrode spacing = 5 μm.

The temperature dependence of pili film conductance was measured with the bipotentiostat cell immersed in a temperature-controlled water bath. I_{DS} was measured at a fixed V_{DS} of 60 mV. Throughout the temperature range measured (2 - 65° C), pili films in aqueous conditions exhibit increasing conductance with decreasing temperature (Fig. 4B). The Arrhenius plot of temperature-dependent conductance exhibit two apparent linear regimes, both with positive slopes, that cross over near room temperature.
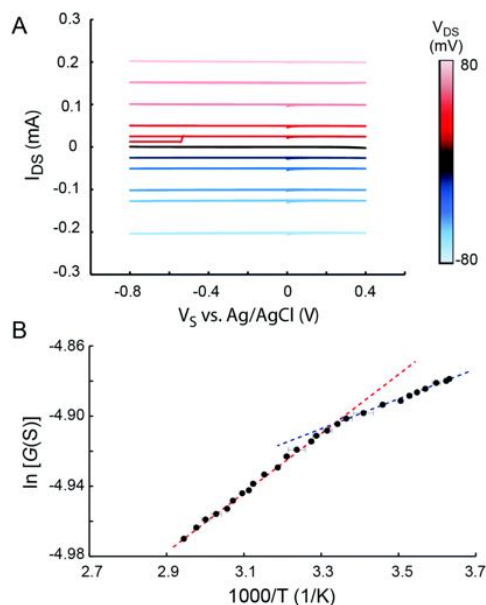
Figure. 4. Electronic transport in purified *G. sulfurreducens* pili in aqueous buffered conditions. (*A*) Electrochemical transfer characteristics of pili film, at different V_{DS} values according to the color scale at the right, in phosphate citrate buffer at pH 7.0. (*B*) Temperature-dependent conductance (*G*) of pili film at V_{DS} = 60 mV and V_S = 0 vs. Ag/AgCl in phosphate citrate buffer pH 7.0. Dashed red and blue lines indicate linear regimes in the Arrhenius plot above and below room temperature (1000/T = 3.39 K^{-1}), respectively. Electrode spacing = 5 μm.

1.4 DISCUSSION

Gel electrophoresis (Fig.1*C*) and mass spectrometry (Fig. 1*D*) confirm the presence of *G. sulfurreducens* pili from the above preparation methods. Under strong denaturing conditions, such as extended boiling in SDS or high concentrations of OG, pili are disassembled into gsPilA monomers that run alongside a TEV protease-cleaved G$_5$PilA control. Native gsPilA and G$_5$PilA bands run above the predicted 6.5 kDa MW, possibly due to their tight α-helical structure in the running buffer, which can interfere with SDS binding [36] and increase the steric bulk of the protein while migrating in the gel. If not treated with strong denaturants, pili remain intact at the top of the gel lane, such as in previously reported preparative gels [33], and do not fly in MALDI-TOF.

Electronic characterization of *G. sulfurreducens* pili was conducted on interdigitated micro-electrode arrays, similar to those used to examine conductivity in polymer films [37] and, more recently, in living *G. sulfurreducens* biofilms [23,29]. *I-V* characteristics of dry films show that pili films are at least four orders of magnitude more conductive than controls, suggesting that conductivity is specific to the purified pili fibers. The two protein controls account for the presence of arbitrary protein on the interdigitated electrodes and the aromaticity and secondary structure of gsPilA: film conductivity of BSA, a well-characterized protein with mixed α helical

and β sheet structure [38], confirmed that a generalized protein deposited on the interdigitated electrodes did not produce appreciable current; comparison with Aβ fiber suggests that the pili possess unique sequence or structural features responsible for electronic conduction.

Aβ fibers have similar diameter and length scales to isolated pili[34] and contain aromatic amino acid residues, which have been suggested to confer conductivity to the pili fibers [12–15,18]. In Aβ fibers, these aromatics are essential for assembly and are located between adjacent sheets at distances < 6.5 Å [39–41]. These distances are comparable to those predicted for the aromatic clusters in some *G. sulfurreducens* pilus homology models [12,14,15]. Despite these structural similarities, Aβ fibers and *G. sulfurreducens* pili are comprised of monomer units assembled in distinctly different secondary structures: Aβ monomers are folded in β sheets [34,40], whereas the gsPilA monomer assembles into a tight α-helix [12,14,15]. The drastic difference in conductivity between the two fibers may be due to the difference in secondary structure or relative positioning of aromatic residues. Indeed, modeling and measurements of homopeptide monolayers suggest that both aromatics residues and α-helical structure independently contribute to peptide conductance [15,42–47].

Purified pili film conductivity follows a percolation network model (Fig. 2*B*). In percolating systems, conductance follows a power law dependence centered about a critical threshold value φ_c, which represents a progression of the network topology with increasing component concentration to a point at which the system undergoes a sharp transition in conductivity. This value is used to distinguish percolation transitions at critical volume fractions, density fractions, concentrations, or mass fractions [48–52] and the conductance of a network composed of conductive elements varies as:

$$G \propto (\varphi - \varphi_c)^t \tag{1}$$

where *t* is the critical exponent, having a theoretical value of 1.3 and 2 for two- and three-dimensional random, resistive wire networks, respectively.

Pili film conductivity experiments were conducted with identical preparation conditions on interdigitated electrodes of varying dimensions. As a result, the conductance of a given pili film can be expressed in terms of an independent device variable, the reduced channel dimension $\frac{L}{w}$. The conductance of the films can thus be expressed as:

$$G \propto \left(\frac{L}{w} - \frac{L}{w_c}\right)^n \tag{2}$$

where $\frac{L}{w_c}$ is the threshold reduced channel dimension and *n* is the percolation exponent, which is not necessarily identical to *t*, given that Equation (2) pertains to percolation onset due to network geometry on the device as opposed onset at a particular size or volume of sample [53]. The electrode spacing serves as a proxy for the length scale of continuous pili network conduction for fixed volumes and concentrations of sample. Fitting Equation (2) to the data (Fig. 2*B*), the threshold reduced channel dimension is $\frac{L}{w_c}$ = 9.08 x 10^{-5}, corresponding to an electrode spacing between 10-15 μm. The mean statistical length of individual pili obtained through our purification was 4.57 μm, suggesting that, on average, at least three pili are involved in the formation of each conductive bridge between electrodes. From the above model, the percolation exponent is *n* = 3.23. Although *n* deviates from theoretical values [50–53], it is consistent with experimental values of *n* for networks of high aspect ratio elements, which range from 0.5 to 4.0

[53]. Deviation from theoretical values is attributed to a distribution of junction resistances at conductor-conductor interfaces within the network [54–57], which may be present in the random networks of pili comprising the channel in our devices. The above percolation network conduction modeling is agnostic of the mechanism (i.e. charge hopping or ohmic transport) of electronic conduction through each pilus fiber. Instead, it describes a dependence of film conduction on the density of junctions and fiber length.

To gain a better understanding of charge transport mechanisms in purified pili films, interdigitated electrodes were modified for electrochemical gating in anaerobic, aqueous electrolyte. A bipotentiostat was used to perform these measurements, as this setup can distinguish between redox and non-redox charge transport mechanisms between the electrodes. The source and drain electrodes are each swept with respect to a Ag/AgCl reference at a fixed source-drain offset potential, V_{DS}, is maintained. Background currents are sunk through a common platinum wire counter electrode, allowing for simultaneous monitoring of oxidation/reduction at each electrode, as well as current between the two electrodes. This experimental setup was previously used to demonstrate redox-mediated conduction in live *G. sulfurreducens* biofilms [23,25,29], and our measurement show a similar response. Except for a faradaic current peak near the redox potential of the cytochromes, no significant current passes between the source and drain electrodes (Fig. 3*A*), suggesting that redox currents dominate long-range electron transport in live *G. sulfurreducens* biofilms.

Measurements with soluble and solid-state redox mediators, potassium ferricyanide and PVF, respectively, show that redox-mediated transport across the device channel exhibits the expected faradaic current peaks (Fig. 3*B* & *C*). I_{DS} is dependent on the gate potential, as current is only observed at potentials associated with redox states of the mediator. The same measurements were conducted for PEDOT:PSS films (Fig. 3*D*) over a gate potential range in which the conducting polymer is not oxidized, as evidenced by a lack of color change [58,59]. In this range, the polymer exhibits ohmic or band-like conduction characteristic of a degenerately-doped semiconductor [60–62]. As opposed to the redox mediator controls, the PEDOT:PSS film exhibits constant current in this range, independent of the gate potential but strongly dependent on the V_{DS}, characteristic of a non-redox current response.

Similar to PEDOT:PSS, isolated pili films exhibit a constant current with respect to gate potential, with no apparent redox-mediated transport activity, and current through the channel is determined by V_{DS}. This current response is similar at neutral pH (Fig. 4*A*) and at pH 4.0, at which cytochromes denature due to protonation of the histidine ligand, thus interfering with heme coordination [35,63]. These findings provide further evidence that cytochromes, while dominating the current response in living biofilm, do not contribute to charge transport through films of purified pili, and that purified pili are inherently electronically conductive in buffered aqueous solutions resembling physiologically-relevant conditions. Previous studies have used β-mercaptoethanol to control for a cytochrome contribution to electronic conduction, but the mechanism of inactivation has been contested due to a lack of precedent [27]. Nevertheless, these electrochemical studies show that charge transport through purified *G. sulfurreducens* pili is dominated by a non-redox mechanism, regardless of any residual cytochromes that may be present in the pili sample.

Temperature-dependent conductance measurements provide further confirmation of an inherent, non-redox-mediated transport mechanism in pili. In vacuum, conductance in pili increases exponentially upon cooling to a point [11], a trend likened to quasi-one-dimensional organic metals [64–67]. The Arrhenius plot of conductance from purified pili films in our

experiments shows two linear regimes, both with a shallow positive slope, in aqueous buffer and physiologically relevant temperatures (Fig 8). Pili conductance increases monotonically with decreasing temperature, a trend consistent with particle-like charge carrier transport in band-like conductors. In such conductors, the Drude model suggests the cross-over between linear regimes indicates distinct scattering rates above and below room temperature. Although the trend of increased conductivity with decreasing temperature is characteristic of metals and metallic-like materials [64–67], other effects may explain this temperature dependence in organic systems. True band conduction in organic materials is typically observed only in molecular crystals [68]. Additionally, isolated pili exhibit a weak temperature dependence, with conductance changing by 10% over a range of 70 K, which is distinct from the exponential temperature dependence observed in isolated pili under vacuum and in metallic-like organic conductors [11,64,65]. Whether the proximity and symmetry of residues responsible for electron transport in pili are adequate for the creation of an electronic energy band is an open question that requires, among other things, a *G. sulfurreducens* pilus crystal structure, to resolve. Instead, it is possible that temperature-dependent conformational changes of the pili are responsible for the observed conduction trend [42,69]. Such fluctuations of molecular structure have been observed to facilitate flickering resonance (transient degeneracy) among electronic states in biomolecules. Because thermal disorder may diminish the probability of energetic state coupling, charge transfer rates are predicted to decrease with increasing temperature[70–72]. Although flickering resonance has not been demonstrated over the micron length scales associated with electron transport along pili, this mechanism may explain the weak temperature-dependence of pili and the ohmic transport observed in *I-V* measurements[71].

Nevertheless, the trend of increasing conductivity with decreasing temperature observed in aqueous buffer confirms the lack of cytochrome involvement in long-range conduction through isolated pili, as redox hopping is a thermally activated process [11,29]. Based on these data, we hypothesize that the inherent conductivity and temperature-dependent behavior observed in purified pili films is due to a combination of aromatic amino acid content and the α-helical nature of the gsPilA monomer, consistent with recent experimental and theoretical work. α-Helical homopeptides support electron transport by increasing electronic coupling between the outer-valence states in peptides [42], possibly due to dipole alignment between peptides [15,73]. Furthermore, this hypothesis is consistent with the seven orders of magnitude difference in conductance of purified pili and the Aβ fiber mats, as well as recent tunneling conductance measurements of individual pili in vacuum, which reveal no observable band gap between conduction states of the pilus at room temperature [31]. These tunneling measurements quantify radial charge transport through *G. sulfurreducens* pili into a conductive substrate in vacuum, as opposed to our experiments which measure charge transport along the axial length of pili and across neighboring pili junctions in the cast films between electrodes in aqueous solution, a configuration that is more relevant to their functional role in living biofilms. Although both adsorption on substrates and vacuum conditions may change the conformation of the pilus [15], these previous observations of activation-less transport at room temperature are corroborated by our measurements of hydrated pili in aqueous buffer . If a hopping transport mechanism exists along the protein backbone of our purified pili films, it is indistinguishable from band conduction and does not exhibit an observable activation energy within the range of biologically-relevant temperatures explored in the present study. In such a case, our results suggest hydrated pili maintain a conformation in which thermal energy (at a minimum of about 24 meV at 0° C) is

sufficient to overcome any putative activation energy required for hopping between isolated states.

1.5 CONCLUSIONS
The data from electrochemically gated *G. sulfurreducens* biofilms corroborate previous findings attributing long-range electron transport to multistep electron hopping between cytochromes. However, identical gating of purified pili films show that pili exhibit an inherent conductivity under conditions similar to those encountered by the source bacterium, and this conductivity is independent of a putative redox hopping mechanism. Together, these results support the hypothesis that pili play a crucial role in mediating conduction through biofilm, demonstrating that although the signature of charge transport through the biofilm is distinct of cytochromes, isolated pili, which are also present in the biofilm, are intrinsically conductive in an environment resembling conditions encountered by the live biofilm . The intrinsic, non-redox-mediated conduction of isolated *G. sulfurreducens* pili suggests a rethinking of models for long-range electron transport in amino acid-based systems. Moreover, the electronic conductivity characteristic of pili in hydrated environments may serve as biological inspiration for the study of structure-property relationships in conductive biomaterials and the development of novel bioelectronics interfaces.

1.6 MATERIALS AND METHODS
Strains and cell culture: All *G. sulfurreducens* cultures (PCA wild type, DSMZ strain 12127) for pili purification were grown anaerobically at 25° C [9] from shaken culture tubes in 1 liter cultures of sterilized and degassed NBAF medium [74]: 0.04 g/L calcium chloride dihydrate, 0.1 g/L magnesium sulfate heptahydrate, 1.8 g/L sodium bicarbonate, 0.5 g/L sodium carbonate, 0.42 g/L potassium phosphate monobasic, 0.22 g/L potassium phosphate dibasic, 0.2 g/L ammonium chloride, 0.38 g/L potassium chloride, 0.36 g/L sodium chloride, vitamins and minerals as listed in ref. [75], and 20mM acetate as the electron donor and 40 mM fumerate as the electron acceptor. Resazurin was omitted and 1mM cysteine was added as an electron scavenger. All chemicals obtained from Fisher Scientific unless otherwise noted.

Purification of *G. sulfurreducens* appendages: After reaching stationary phase, *G. sulfurreducens* cells were pelleted from cultures by centrifugation at 5000 g for 20 min at 4° C. *G. sulfurreducens* pili were purified from this initial supernatant using a 1:10 ratio of 1.1 M aqueous $MgCl_2$ to supernatant. Supernatants were precipitated overnight at 4° C and centrifuged at 50,000 g for 1 h at 4° C to obtain pili. Pili pellets were resuspended with ultrapure water passaged through 0.2 μm filters and additional contaminants were removed with 30-50kDa dialysis tubing. After three 1 L exchanges of ultrapure water, the dialyzed sample was collected for use and stored at 4° C. Cytochrome-containing proteins precipitated during storage and pili were collected from the clear supernatant. Purified *G. sulfurreducens* pili were characterized by SDS-PAGE, peptide mass spectrometry, and MALDI-TOF as described in the Supporting Information.

Measurement of electronic conductance of bacterial appendages: Pili and control films were spun coat onto interdigitated electrode devices in 10μL intervals to obtain a total mass of 115 μg protein per device. For solid state measurements, films were measured (Keithley Model 2612B)

under ambient conditions at room temperature, with voltage swept between -0.8 and 0.8 V. Data in Fig. 2*B* are averages of $n = 3$ conductance values from independent *I-V* measurements.

For electrical transfer characteristics experiments, all measurements were conducted in 0.1 M phosphate-citrate buffer, with the pH varied by changing the relative amounts of sodium phosphate dibasic and sodium citrate, except the $K_3[Fe(CN)_6]$ control and live biofilms. $K_3[Fe(CN)_6]$ transfer characteristic data were collected using 20 mM $K_3[Fe(CN)_6]$ in 0.1 M KCl. Biofilm experiments were conducted in growth media under turnover conditions. Electrolyte solutions were degassed and electrochemical cells were assembled in an anaerobic chamber. Electrochemical cells were 100 mL sealed glass containers with wire connections mediated through rubber septa. Two Gamry potentiostats (series PCI4/300), linked through a bipotentiostat cable, were used to conduct cyclic voltammetry sweeps where the source and drain serve as two working electrodes. Both were referenced to the same Ag/AgCl reference electrode and shared a platinum wire counter electrode. The source electrode was swept for two cycles from 0.4 to 0.8 V with respect to the Ag/AgCl reference electrode, and the drain was swept over the same range at a fixed V_{DS} relative to the source. After subtracting any background catalytic current present at $V_{DS} = 0$, the difference currents between the source and the drain were plotted as the conducting current I_{con}. Voltages were scanned at a rate of 10 mV/s.

For temperature-dependent studies, the electrochemical cells were placed in a stirred water bath, and the temperature was regulated using a hot plate with a thermocouple fixed in the water bath. Cooling was achieved by adding ice to the water bath. Bipotentiostat chronoamperometry measurements were performed temperature equilibration for several minutes. Currents from the source and drain were independently monitored while the drain was held at $V_{DS} = 60$ mV offset from the source. The steady-state currents at the source and drain were averaged over 1 min acquisition. The total current was taken to be half the difference between the source and drain currents, which were symmetric but with opposite polarity.[29] Measurements were performed with 0.1 M phosphate citrate buffer at pH 7.0 as the supporting electrolyte.

1.7 REFERENCES

1   H. B. Gray and J. R. Winkler, *Proc. Natl. Acad. Sci. U. S. A.*, 2005, **102**, 3534–3539.
2   V. N. Kharkyanen, E. G. Petrov and I. I. Ukrainskii, *J. Theor. Biol.*, 1978, **73**, 29–50.
3   J. Jortner, M. Bixon, T. Langenbacher and M. E. Michel-Beyerle, *Proc. Natl. Acad. Sci.*, 1998, **95**, 12759–12765.
4   H. B. Gray and J. R. Winkler, *Q. Rev. Biophys.*, 2003, **36**, 341–372.
5   S. S. Skourtis, *Pept. Sci.*, 2013, **100**, 82–92.
6   H. B. Gray and J. R. Winkler, *Biochim. Biophys. Acta*, 2010, **1797**, 1563–1572.
7   L. P. Nielsen, N. Risgaard-Petersen, H. Fossing, P. B. Christensen and M. Sayama, *Nature*, 2010, **463**, 1071–1074.
8   C. Pfeffer, S. Larsen, J. Song, M. Dong, F. Besenbacher, R. L. Meyer, K. U. Kjeldsen, L. Schreiber, Y. A. Gorby, M. Y. El-Naggar, K. M. Leung, A. Schramm, N. Risgaard-Petersen and L. P. Nielsen, *Nature*, 2012, **491**, 218–221.
9   G. Reguera, K. D. McCarthy, T. Mehta, J. S. Nicoll, M. T. Tuominen and D. R. Lovley, *Nature*, 2005, **435**, 1098–1101.
10 S. Pirbadian, S. E. Barchinger, K. M. Leung, H. S. Byun, Y. Jangir, R. A. Bouhenni, S. B. Reed, M. F. Romine, D. A. Saffarini, L. Shi, Y. A. Gorby, J. H. Golbeck and M. Y. El-Naggar, *Proc. Natl. Acad. Sci.*, 2014, **111**, 12883–12888.
11 N. S. Malvankar, M. Vargas, K. P. Nevin, A. E. Franks, C. Leang, B.-C. Kim, K. Inoue, T. Mester, S. F. Covalla, J. P. Johnson, V. M. Rotello, M. T. Tuominen and D. R. Lovley, *Nat. Nanotechnol.*, 2011, **6**, 573–579.
12 K. Xiao, N. S. Malvankar, C. Shu, E. Martz, D. R. Lovley and X. Sun, *Sci. Rep.*, 2016, **6**, 23385.
13 N. S. Malvankar, M. Vargas, K. Nevin, P.-L. Tremblay, K. Evans-Lutterodt, D. Nykypanchuk, E. Martz, M. T. Tuominen and D. R. Lovley, *mBio*, 2015, **6**, e00084-15.
14 P. N. Reardon and K. T. Mueller, *J. Biol. Chem.*, 2013, **288**, 29260–29266.
15 G. T. Feliciano, A. J. R. da Silva, G. Reguera and E. Artacho, *J. Phys. Chem. A*, 2012, **116**, 8023–8030.
16 N. S. Malvankar, S. E. Yalcin, M. T. Tuominen and D. R. Lovley, *Nat. Nanotechnol.*, 2014, **9**, 1012–1017.
17 S. M. Strycharz-Glaven, R. M. Snider, A. Guiseppi-Elie and L. M. Tender, *Energy Environ. Sci.*, 2011, **4**, 4366–4379.
18 M. Vargas, N. S. Malvankar, P.-L. Tremblay, C. Leang, J. A. Smith, P. Patel, O. Synoeyenbos-West, K. P. Nevin and D. R. Lovley, *mBio*, 2013, **4**, e00105–e00113.
19 T. Boesen and L. P. Nielsen, *mBio*, 2013, **4**, e00270-13.
20 H. Yan, C. Chuang, A. Zhugayevych, S. Tretiak, F. W. Dahlquist and G. C. Bazan, *Adv. Mater.*, 2015, **27**, 1908–1911.
21 G. T. Feliciano, R. J. Steidl and G. Reguera, *Phys. Chem. Chem. Phys.*, 2015, **17**, 22217–22226.
22 R. J. Steidl, S. Lampa-Pastirk and G. Reguera, *Nat. Commun.*, 2016, **7**, 12217.
23 R. M. Snider, S. M. Strycharz-Glaven, S. D. Tsoi, J. S. Erickson and L. M. Tender, *Proc. Natl. Acad. Sci.*, 2012, **109**, 15467–15472.
24 D. R. Bond, S. M. Strycharz-Glaven, L. M. Tender and C. I. Torres, *ChemSusChem*, 2012, **5**, 1099–1105.

25 M. D. Yates, S. M. Strycharz-Glaven, J. P. Golden, J. Roy, S. Tsoi, J. S. Erickson, M. Y. El-Naggar, S. C. Barton and L. M. Tender, *Nat. Nanotechnol.*, 2016, **11**, 910–913.

26 Y. Liu, H. Kim, R. R. Franklin and D. R. Bond, *ChemPhysChem*, 2011, **12**, 2235–2241.

27 S. M. Strycharz-Glaven and L. M. Tender, *Energy Environ. Sci.*, 2012, **5**, 6250–6255.

28 N. S. Malvankar, M. T. Tuominen and D. R. Lovley, *Energy Environ. Sci.*, 2012, **5**, 8651.

29 M. D. Yates, J. P. Golden, J. Roy, S. M. Strycharz-Glaven, S. Tsoi, J. S. Erickson, M. Y. El-Naggar, S. C. Barton and L. M. Tender, *Phys. Chem. Chem. Phys.*, 2015, **17**, 32564–32570.

30 S. M. Strycharz, A. P. Malanoski, R. M. Snider, H. Yi, D. R. Lovley and L. M. Tender, *Energy Environ. Sci.*, 2011, **4**, 896–913.

31 S. Lampa-Pastirk, J. P. Veazey, K. A. Walsh, G. T. Feliciano, R. J. Steidl, S. H. Tessmer and G. Reguera, *Sci. Rep.*, 2016, **6**, 23517.

32 P. S. Bonanni, D. Massazza and J. P. Busalmen, *Phys. Chem. Chem. Phys.*, 2013, **15**, 10300–10306.

33 D. L. Cologgi, S. Lampa-Pastirk, A. M. Speers, S. D. Kelly and G. Reguera, *Proc. Natl. Acad. Sci.*, 2011, **108**, 15248–15252.

34 R. N. Rambaran and L. C. Serpell, *Prion*, 2008, **2**, 112–117.

35 L. Wang and D. H. Waldeck, *J. Phys. Chem. C*, 2008, **112**, 1351–1356.

36 A. Rath, M. Glibowicka, V. G. Nadeau, G. Chen and C. M. Deber, *Proc. Natl. Acad. Sci.*, 2009, **106**, 1760–1765.

37 M. J. Natan and M. S. Wrighton, in *Progress in Inorganic Chemistry*, ed. S. J. Lippard, John Wiley & Sons, Inc., 1989, pp. 391–494.

38 B. Jachimska and A. Pajor, *Bioelectrochemistry*, 2012, **87**, 138–146.

39 R. Cukalevski, B. Boland, B. Frohm, E. Thulin, D. Walsh and S. Linse, *ACS Chem. Neurosci.*, 2012, **3**, 1008–1016.

40 E. Gazit, *FASEB J.*, 2002, **16**, 77–83.

41 A. Reymer, K. K. Frederick, S. Rocha, T. Beke-Somfai, C. C. Kitts, S. Lindquist and B. Nordén, *Proc. Natl. Acad. Sci.*, 2014, **111**, 17158–17163.

42 L. Sepunaru, S. Refaely-Abramson, R. Lovrinčić, Y. Gavrilov, P. Agrawal, Y. Levy, L. Kronik, I. Pecht, M. Sheves and D. Cahen, *J. Am. Chem. Soc.*, 2015, **137**, 9617–9626.

43 J. Pawlowski, J. Juhaniewicz, D. Tymecka and S. Sek, *Langmuir*, 2012, **28**, 17287–17294.

44 A. Atanassov, Z. Hendler, I. Berkovich, G. Ashkenasy and N. Ashkenasy, *Pept. Sci.*, 2013, **100**, 93–99.

45 M. Amit, S. Appel, R. Cohen, G. Cheng, I. W. Hamley and N. Ashkenasy, *Adv. Funct. Mater.*, 2014, **24**, 5873–5880.

46 N. Amdursky, *ChemPlusChem*, 2015, **80**, 1075–1095.

47 Y. K. Shin, M. D. Newton and S. S. Isied, *J. Am. Chem. Soc.*, 2003, **125**, 3722–3732.

48 B. Kim, S. Pfeifer, S.-H. Park and P. R. Bandaru, in *Materials Research Society Proceedings*, 2011, vol. 1312, pp. 281–286.

49 M. Jagota and N. Tansu, *Sci. Rep.*, 2015, **5**, 10219.

50 G. Khanarian, J. Joo, X.-Q. Liu, P. Eastman, D. Werner, K. O'Connell and P. Trefonas, *J. Appl. Phys.*, 2013, **114**, 24302.

51 B. P. Grady, D. J. Arthur and J. Ferguson, *Polym. Eng. Sci.*, 2009, **49**, 2440–2446.

52 S. I. White, R. M. Mutiso, P. M. Vora, D. Jahnke, S. Hsu, J. M. Kikkawa, J. Li, J. E. Fischer and K. I. Winey, *Adv. Funct. Mater.*, 2010, **20**, 2709–2716.

53 S. De, P. J. King, P. E. Lyons, U. Khan and J. N. Coleman, *ACS Nano*, 2010, **4**, 7064–7072.

54 N. Johner, C. Grimaldi, I. Balberg and P. Ryser, *Phys. Rev. B*, 2008, **77**, 174204.

55 I. Balberg, *Phys. Rev. B*, 1998, **57**, 13351–13354.

56 I. Balberg, *Phys. Rev. Lett.*, 1987, **59**, 1305–1308.

57 S. Vionnet-Menot, C. Grimaldi, T. Maeder, S. Strässler and P. Ryser, *Phys. Rev. B*, 2005, **71**, 64201.

58 H.-S. Park, S.-J. Ko, J.-S. Park, J. Y. Kim and H.-K. Song, *Sci. Rep.*, , DOI:10.1038/srep02454.

59 Q. Pei, G. Zuccarello, M. Ahlskog and O. Inganäs, *Polymer*, 1994, **35**, 1347–1351.

60 X. Crispin, F. L. E. Jakobsson, A. Crispin, P. C. M. Grim, P. Andersson, A. Volodin, C. van Haesendonck, M. Van der Auweraer, W. R. Salaneck and M. Berggren, *Chem. Mater.*, 2006, **18**, 4354–4360.

61 D. J. Gaspar and E. Polikarpov, *OLED Fundamentals: Materials, Devices, and Processing of Organic Light-Emitting Diodes*, CRC Press, 2015.

62 A. Elschner, S. Kirchmeyer, W. Lovenich, U. Merker and K. Reuter, *PEDOT: Principles and Applications of an Intrinsically Conductive Polymer*, CRC Press, 2010.

63 H. R. Drew and R. E. Dickerson, *J. Biol. Chem.*, 1978, **253**, 8420–8427.

64 P. Dallas, D. Stamopoulos, N. Boukos, V. Tzitzios, D. Niarchos and D. Petridis, *Polymer*, 2007, **48**, 3162–3169.

65 A. B. Kaiser, *Adv. Mater.*, 2001, **13**, 927–941.

66 A. J. Heeger, N. S. Sariciftci and E. B. Namdas, *Semiconducting and Metallic Polymers*, Oxford University Press, 2010.

67 T. A. Skotheim and J. R. Reynolds, *Handbook of Conducting Polymers*, CRC Press, 2007, vol. 2.

68 V. May and O. Kuhn, *Charge and energy transfer dynamics in molecular systems*, Wiley, Weinheim, Germany, 3rd edn., 2011.

69 H. Shpaisman, O. Seitz, O. Yaffe, K. Roodenko, L. Scheres, H. Zuilhof, Y. J. Chabal, T. Sueyoshi, S. Kera, N. Ueno, A. Vilan and D. Cahen, *Chem. Sci.*, 2012, **3**, 851–862.

70 Y. Zhang, C. Liu, A. Balaeff, S. S. Skourtis and D. N. Beratan, *Proc. Natl. Acad. Sci. U. S. A.*, 2014, **111**, 10049–10054.

71 D. N. Beratan, C. Liu, A. Migliore, N. F. Polizzi, S. S. Skourtis, P. Zhang and Y. Zhang, *Acc. Chem. Res.*, 2015, **48**, 474–481.

72 C. Liu, L. Xiang, Y. Zhang, P. Zhang, D. N. Beratan, Y. Li and N. Tao, *Nat. Chem.*, 2016, **8**, 941–945.

73 F. Rissner, A. Natan, D. A. Egger, O. T. Hofmann, L. Kronik and E. Zojer, *Org. Electron.*, 2012, **13**, 3165–3176.

74 M. V. Coppi, C. Leang, S. J. Sandler and D. R. Lovley, *Appl. Environ. Microbiol.*, 2001, **67**, 3180–3187.

75 D. R. Lovley, R. C. Greening and J. G. Ferry, *Appl. Environ. Microbiol.*, 1984, **48**, 81–87.

CHAPTER 2:

Cryo-Electron Microscopy Structure of Conductive *Geobacter sulfurreducens* Filaments

2.1 SUMMARY

Long-range (> 10 μm) transport of electrons along networks of *Geobacter sulfurreducens* protein filaments, known as microbial nanowires, has been invoked to explain a wide range of globally-important redox phenomena. These nanowires were previously thought to be type IV pili composed of PilA protein, including in our work in the preceding chapter. Here we report a 3.7 Å resolution cryo-electron microscopy structure which surprisingly reveals that, rather than PilA, *G. sulfurreducens* nanowires are assembled by micrometer-long polymerization of the hexaheme cytochrome OmcS, with hemes packed within ~3.5-6 Å of each other. The inter-subunit interfaces show unique structural elements such as inter-subunit parallel-stacked hemes and axial coordination of heme by histidines from neighbouring subunits. Wild-type OmcS filaments show 100-fold greater conductivity than other filaments from an Δ*omcS* strain, highlighting the importance of OmcS to conductivity in such structures. This structure explains the remarkable capacity of soil bacteria to transport electrons to remote electron acceptors for respiration and energy sharing.

2.2 INTRODUCTION

Conductive filamentous appendages of common soil bacteria *Geobacter* (Reguera et al., 2005), referred to as microbial nanowires, play a critical role in long-range extracellular electron transfer for respiration (Malvankar et al., 2011) and interspecies electron exchange (Summers et al., 2010). These nanowires have been invoked to explain a wide range of globally-important redox phenomena that influence carbon and mineral cycling in soils and sediments, bioremediation, corrosion, and anaerobic conversion of organic wastes to methane or electricity (Malvankar and Lovley, 2014; Malvankar et al., 2011). However, these filament's composition, structure and underlying conduction mechanism have remained uncertain because the filaments are difficult to solubilize for studies using traditional biochemical methods and X-ray crystallography. *Geobacter sulfurreducens* serves as a model organism for the broader phenomenon of extracellular electron transfer because it produces these conductive filaments (Tan et al., 2017), has a fully sequenced genome and well-developed genetic system (Reguera et al., 2005). In contrast to other electron-transferring bacteria (Marsili et al., 2008), *G. sulfurreducens* does not use diffusing shuttle molecules but requires direct contact with an electron acceptor via conductive filaments for long-range extracellular electron transfer (Reguera et al., 2005).

    G. sulfurreducens outer-surface *c*-type cytochromes, including the hexaheme cytochrome OmcS (Qian et al., 2011), are known to play a critical role in bacterial growth on insoluble electron acceptors, including Fe (III) oxide and electrodes (Holmes et al., 2006; Mehta et al., 2005). Nonetheless, previous studies proposed conductive *Geobacter* filaments were type IV pili composed of PilA protein for a number of reasons: i) electron-transferring cells showed high levels of messenger RNA for PilA (Childers et al., 2002); ii) the amino acid sequence of *G. sulfurreducens* PilA is similar to the N-terminal sequence of PilA from other type IV pili-producing bacteria (Reguera et al., 2005); iii) genomic organization of *G. sulfurreducens* pilus biosynthesis genes was also similar to other type IV pili-producing bacteria (Reguera et al.,

2005); iv) a *pilA* deletion mutant strain lacked filaments and could not transfer electrons extracellularly (Reguera et al., 2005); v) point mutations in *pilA* caused cells to produce filaments with different conductivities than wild-type (WT) filaments (Adhikari et al., 2016; Tan et al., 2016a; Tan et al., 2017; Vargas et al., 2013). Because of these extensive literature data, previous studies, presumed that conductive filaments were type IV PilA pili. Despite these data, there has never been any direct evidence that conductive *Geobacter* extracellular filaments are composed of PilA. Instead, the filament composition was inferred from indirect evidence, including the presence of PilA in biochemical analyses (Tan et al., 2016b) or from low-resolution imaging by atomic force microscopy (AFM) and negative-staining transmission electron microscopy that suggested filament dimensions similar to type IV pili (Reguera et al., 2005).

On the other hand, alternative functional roles have been suggested for PilA (Reguera et al., 2007). PilA is associated with the secretion of OmcS to the outer surface (Liu et al., 2018; Richter et al., 2012), and overexpression of PilA is accompanied by overproduction of OmcS and extracellular filaments (Leang et al., 2013; Summers et al., 2010). Here, we show that the conductive extracellular appendages of wild-type *G. sulfurreducens* strain are primarily OmcS filaments. These appendages are polymerized filaments of OmcS with unique structural features that also provide a new basis for understanding long-range electronic transport in proteins. Gel electrophoresis, mass spectrometry, AFM, and conductivity measurements show that these nanowires are the same filaments that were previously thought to be type IV pili. Data from these studies are consistent with the previous studies, and our results establish a new class of bacterial nanowires based on cytochrome polymerization.

2.3 RESULTS AND DISCUSSION

The following results reconcile previous observations by directly identifying the composition and structure of conductive filaments using cryo-electron microscopy (Cryo-EM). We grew WT cultures using anodes of microbial fuel cells as the sole electron acceptors (O'Brien and Malvankar, 2017). These growth conditions promote production of conductive biofilms and filaments as well as overexpression of PilA in comparison with growth on soluble electron acceptors such as fumarate. (Malvankar et al., 2011). Consistent with previous studies (Tan et al., 2016b), we confirmed the presence of both PilA and OmcS with expected molecular weights of ~ 6.5 kDa and ~ 45 kDa respectively in our filament preparations using polyacrylamide gel electrophoresis (SDS-PAGE), peptide mass spectrometry and western immunoblotting.

Cryo-EM images of filaments purified from the WT strain showed a sinusoidal morphology with a period of ~ 200 Å (Fig. 1A). Averaged power spectra from multiple filaments show a meridional layer line at $\sim 1/(47$ Å$)$, establishing that there are ~ 4.3 subunits per turn of a ~ 200 Å pitch 1-start helix (Fig. 1B). Using the iterative helical real space reconstruction (IHRSR) approach (Egelman, 2000a), we were able to reach a resolution where the handedness of α-helices was clearly visible. The 1-start filament helix was left-handed, with a rise per subunit of 46.7 Å and a rotation of -83.1° (Fig. 1B), which was substantially different than type IV pili that typically show a rise of ~ 10 Å and a right-handed helix (Wang et al., 2017). The tracing of a C_α backbone of the protein subunit at this resolution revealed that the asymmetric unit contained at least 380 residues, which contrasts with the 61 residues present in PilA (Reardon and Mueller, 2013; Reguera et al., 2005). Further, there was no apparent internal symmetry that would arise in the asymmetric unit if it contained multiple copies of identical chains. The NMR structure of PilA (Reardon and Mueller, 2013) also failed to fit into the observed EM density map.
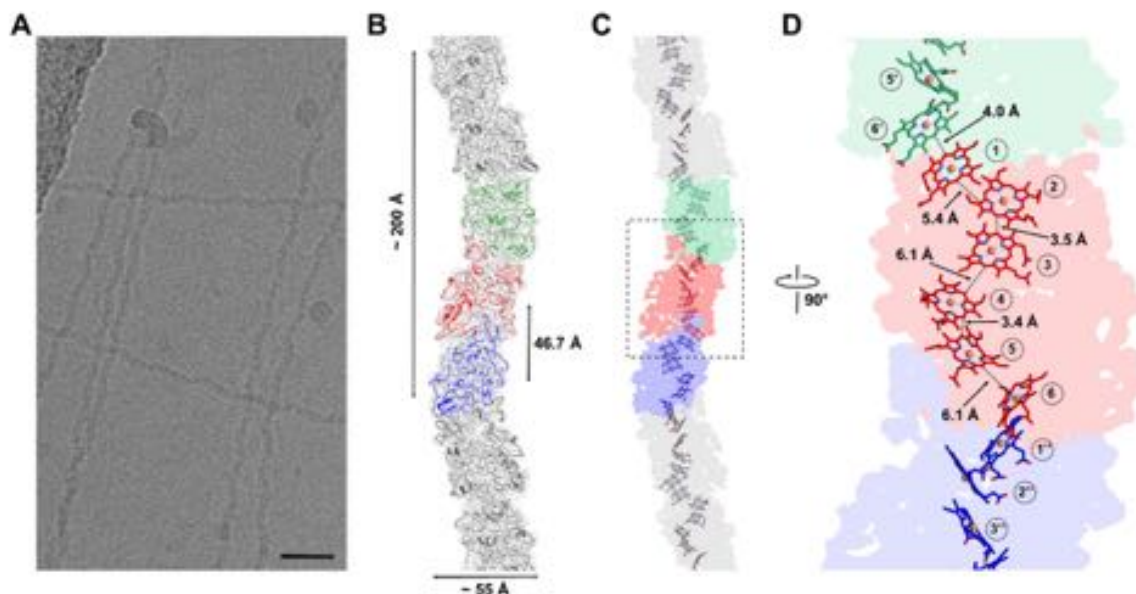
Figure 1. Structure of microbial nanowires reveals closely-stacked hemes in an OmcS filament. (A) Cryo-EM image of the purified wild-type electrically-conductive filaments showing a sinusoidal undulation with a pitch of ~ 200 Å. Scale bar, 200 Å. **(B)** The surface of the reconstruction (transparent gray) with superimposed ribbon models of the OmcS subunits with three subunits in the center in three different colors. **(C)** Each subunit contains six hemes closely stacked over the micrometer-lengths of the filaments. **(D)** A zoomed region of the box shown in (C) with the minimum observed edge-to-edge distances indicated between hemes numbered in circles. The distance between two hemes in adjacent subunits (heme 1 and heme 6′) is comparable to the distances between parallel stacked hemes within a subunit (heme 2:heme 3 and heme 4:heme 5).

Surprisingly, we found that there were six hemes per asymmetric unit, with the highest densities in the volume at the centres of these hemes, suggesting the presence of metal atoms. Given that the protein contains at least 380 residues and would therefore have a likely molecular weight between 40-50 kDa, we used SDS-PAGE and cut out the strongest band in the gel, which was at ~ 45 kDa and analysed this band by mass spectrometry. Five proteins were identified, four of which had heme-binding motifs (CXXCH) and had masses between 45 and 49 kDa. Three of these proteins (OmcS, OmcT and GSU2501) had a very similar pattern of heme-binding motifs that approximately matched the initial C_α trace (Fig. 2B), and their sequences could be easily aligned (Fig. 2A). These three proteins had between 45-63% sequence identity with each other. Another protein found in mass spectrometry, OmcZ (Inoue et al., 2010), contained ~ 30 additional residues compared to the other three, and thus its sequence could not be aligned to the others, and furthermore the pattern of eight heme-binding motifs in OmcZ did not match that found in the map. The remaining protein OmpJ contains no heme (Afkar et al., 2005). Of the three possible candidates, only the OmcS sequence could be threaded through the map without any conflicts (Figure 2C,D). There are nine regions of OmcT, GSU2501, or both which prevented their sequences from being fitted into the map (Fig. 2A highlighted in blue). In addition, the pattern of bulky amino acids established clearly that only the OmcS sequence was consistent with the map. For example, the elongated density from Arginine (R) 256 is clearly seen in the map (Fig. 2D). But in the sequences of OmcT and GSU2501, this residue would be a valine (Fig. 2A, highlighted in purple) and could not explain the map density. These studies show that the only cytochrome found by mass spectrometry in our filament preparations that is consistent with the cryo-EM map is OmcS.
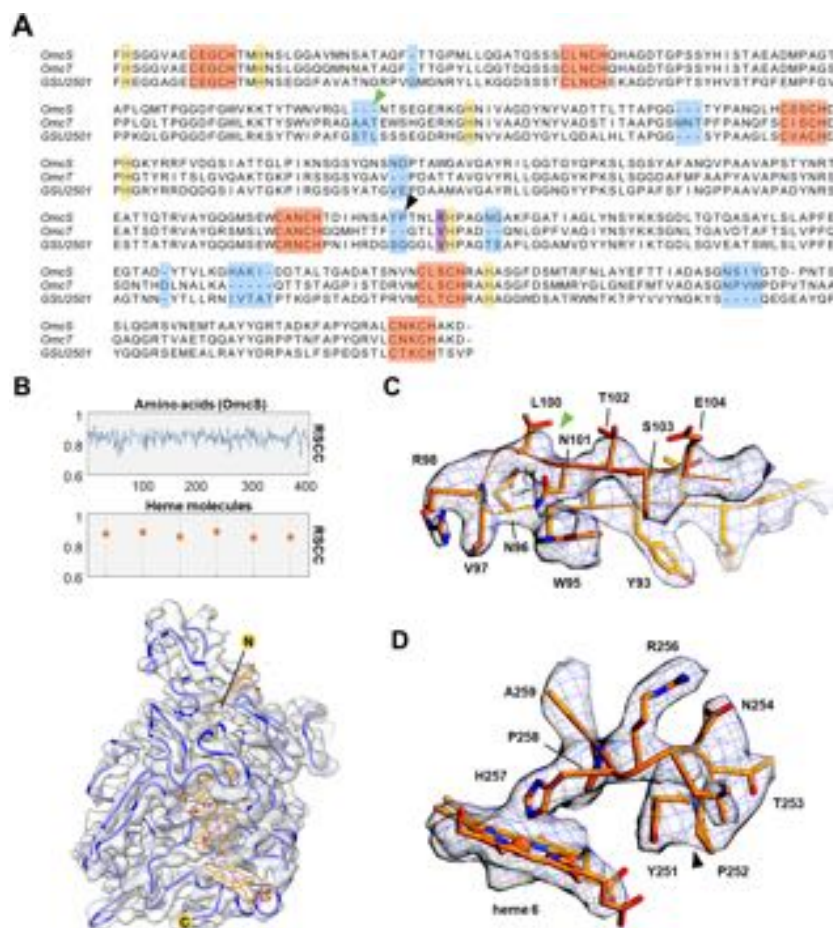
Figure 2. *De novo* atomic model building of OmcS filaments. (A) Sequence-based alignment of OmcS and two other *c*-type cytochromes with similar molecular weight detected by mass spectroscopy. The six conserved CXXCH motifs responsible for heme binding are highlighted in red. The histidine residues paired with the CXXCH motifs in heme binding are highlighted in yellow. Regions with insertions or deletions compared to the OmcS sequence are highlighted in blue. **(B)** The per-residue real space correlation coefficient (RSCC) plot of the atomic model against the 3.7 Å cryo-EM map (top), with protein and ligand displayed separately. The protein C_α trace in blue with ligands (bottom), with N- and C-termini labeled. **(C)** and **(D)** Zoomed view of the regions indicated in (A) by green and black arrowheads, respectively, with the OmcS atomic model fit into the cryo-EM map. The green arrowhead in (C) indicates the location where the two other cytochromes (OmcT, GSU2501) show a three-residue insertion, not compatible with the map. The black arrowhead in (D) indicates a region where OmcT has a two-residue deletion, and GSU2501 has a serine and glycine rather than the tyrosine and proline found in OmcS. The map has extra density that could not be explained by a two-residue deletion or serine and glycine.

We built an *ab initio* atomic model of OmcS, which was then used to refine a filament model. We directly estimated its resolution using a map:model comparison (Neumann et al., 2018; Subramaniam et al., 2016) which yielded an estimate of 3.7 Å. Strikingly, the "gold standard" measure of resolution employed by Relion (Scheres, 2012), which is based upon reproducibility, yielded an estimate of 3.2 Å. Comparing the Relion map (filtered to 3.2 Å) and our map generated in Spider (filtered to 3.6 Å) showed no significant differences, suggesting that the Relion estimate of resolution is overly optimistic. Overall, the fit of the model to the map, the good density for many sidechains, and the refinement statistics (Table 1) all validate our model of the OmcS filament.

**Table 1: Refinement statistics for the OmcS model**

	OmcS model
Helical symmetry	
Rise (Å)	46.7
Rotation (°)	-83.1
Resolution (Å)	**3.7**
Model to map CC	**0.82**
Clash score, all atoms	**12.8**
Protein geometry	
Ramachandran favored (%)	88.2
Ramachandran outliers (%)	0.4
Rotamer outliers (%)	**0.0**
Cβ deviations > 0.25 Å	**0**
RMS deviations	
Bond (Å)	0.01
Angles (°)	1.36
PDB ID	**6EF8**
EMDB ID	**EMD-9046**

While it has been known for more than half a century that cytochromes can polymerize in ethanolic solutions (Margoliash and Lustgarten, 1962) and structures have been determined for aggregates up to tetramers (Hirota et al., 2010), natural polymerization of the type we observe here has not been previously described to our knowledge. Stacking arrangements of aromatic rings generally prefer parallel (offset face-to-face) or perpendicular (T-shaped) conformations (Janiak, 2000). The parallel stacking yields the highest electronic coupling, which maximizes electron transfer (Jiang et al., 2017), whereas the T-shape enhances structural stability (Janiak, 2000). Hemes in the OmcS nanowires form parallel-stacked pairs, with each pair perpendicular to the next, forming a continuous chain over the entire length of the filament (Fig. 1D). The minimum edge-to-edge distances between the parallel hemes is 3.4 to 4.1 Å, and 5.4 to 6.1 Å between the perpendicular stacked pairs. For all hemes in OmcS nanowires, two histidines axially coordinate iron at the centre of each heme and the vinyl groups of each heme form covalent thioether bonds with cysteines (Fig. 3). The bis-histidine axial ligation of the heme iron atoms are consistent with the coordination found in other *c*-type cytochromes (Clarke et al., 2011), and the cysteine linkages are consistent with the *c*-type hemes reported to occupy six heme-binding motifs of OmcS (Qian et al., 2011).

Our OmcS model filament has a low percentage of α- and 3_{10}-helices (~ 13%) as well as β-strands (~ 6%), leaving ~ 81% of the model as turns and coil - consistent with previous secondary structure studies of OmcS monomers (Qian et al., 2011). We compared the OmcS protomer within the filament with a group of three crystallographic structures of other multi-heme *c*-type cytochromes (PDB IDs: 1ofw, 3ucp, and 3ov0). These structures showed 45, 49,

and 60% turns and coils, respectively, with uniformly hydrophobic cores surrounding the hemes and heme-binding residues. Cores in our model of OmcS also included buried charges (Arginine at locations 333, 344 and 375) that lack proximal compensating charges, as well as buried sidechain hydroxyls (Tyrosine at locations 186, 231, 385). In addition, our model of OmcS has a salt bridge between protein chains, Aspartate 407 to Arginine 151, which, along with cysteines in heme binding motifs, are highly conserved amino acids in OmcS (Ashkenazy et al., 2016). The lack of structural homology seen with these other *c*-type cytochromes is consistent with the observation that there is no conserved fold for this family of proteins (Bertini et al., 2006).

The model shows that each OmcS subunit contacts only one subunit on either side, so that all connectivity in the filament is along the left-handed 1-start helix (Fig. 1B). The interface between adjacent subunits is extensive, with ~ 2,600 Å^2 of surface area buried per subunit (Fig. 3A). In addition to the buried surface area, interactions between adjacent subunits incorporate additional stabilizing elements unique to the filament structure. Histidine 16 of one subunit coordinates the iron in heme 5 of an adjacent subunit (Fig. 3B). Furthermore, heme pairs at the interface are parallel rather than T-shaped with ~ 4 Å edge-to-edge distance (Figures 1D, 3B,C). This parallel stacking and inter-subunit coordination of heme may contribute substantially to the stability of the protein-protein interface. In addition, the presence of parallel-stacked hemes at the interface suggests facile transport of electrons between monomers.
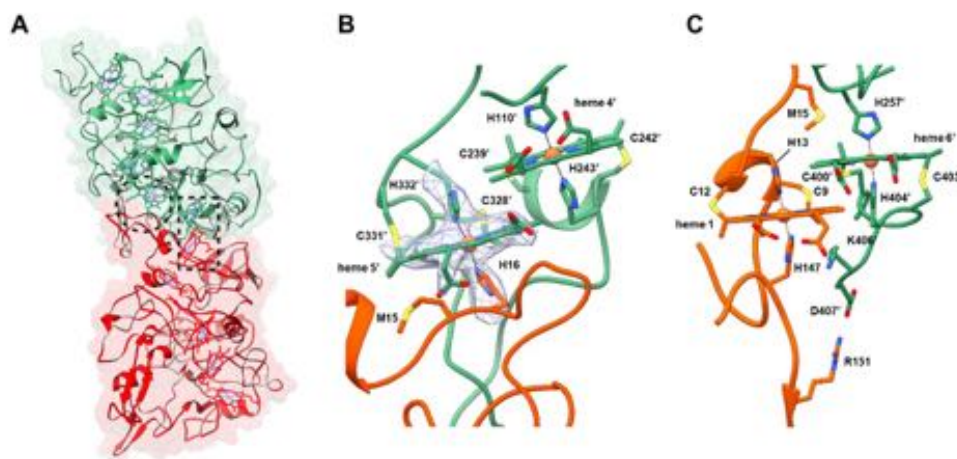
Figure 3. Subunit interface interactions within OmcS filament. (A) The large interface in the filament (~ 2,600 Å^2 per subunit) is due to the complementarity between the top of one subunit (green) and the bottom of an adjacent subunit (red). Residues in one subunit strongly interact via hemes shown in the dashed circle and rectangle (orange) and corresponding zoomed images in **B** and **C** respectively. **(B)** Histidine 16 of the bottom subunit is coordinating the iron atom in heme 5′ of the top subunit. The cryo-EM densities corresponding to Histidine 16, Histidine 332′, and heme 5' are shown in a mesh. **(C)** The stacking of heme 6′ from a top subunit

There is no precedent for such seamless micrometer-long polymerization of hundreds of cytochromes to our knowledge. Based on previous studies that have shown that cytochromes could form tetramers, the OmcS polymerization could be due to successive domain swapping, where the *c*-terminal helix can be displaced from its original position in the monomer and histidine-heme coordination can be perturbed significantly (Hirota et al., 2010). We have determined the structure for the OmcS protomer within the filament, but the structure of isolated OmcS monomer is needed to provide insight into this surprising polymerization process.

The atomic structure was solved with filaments from conductive biofilms of electrode-grown cells that require long-distance electron transport. However, fumarate-grown cells can also produce conductive filaments (Ing et al., 2017; Leang et al., 2013; Leang et al., 2010; Malvankar et al., 2011; Reguera et al., 2005). Filaments purified with fumarate-grown cells showed similar structure to filaments purified from electrode-grown cells. Moreover, previously published images of intact *G. sulfurreducens* filaments attached to cells (Leang et al., 2013) showed structural features similar to purified filaments such as an identical helical rise of 47 Å. These results showed that purified OmcS filaments are similar in dimensions and structure to cell-attached filaments that were previously thought to be type IV pili (Leang et al., 2013). Importantly, these studies also indicate that the formation of OmcS filaments is a natural process and not due to artificial preparation or pH conditions that can cause cytochrome *c* to form filamentous structures under extremely denaturing conditions (Haldar et al., 2014).

The cryo-EM images showed another filamentous structure that was thinner than the OmcS filament. The averaged power spectrum of these filaments showed similar layer lines to the OmcS filament, but with a slightly different axial rise of ~ 57 Å and rotation of ~ 160 degrees, suggesting that it is also not a type IV pilus and could potentially be another cytochrome filament. Due to much lower abundance of this filament, it was not possible to build an atomic model or to determine its composition. No filaments with power spectra consistent with type IV pili were observed in purified filaments preparations or in previously published images of intact, cell-attached filaments (Leang et al., 2013).

To evaluate the contribution of OmcS to the conductivity of these filaments, the DC conductivity of individual OmcS filaments of WT strain were compared with sparse filaments produced by a Δ*omcS* strain. *G. sulfurreducens* forms a variety of filaments in response to genetic mutations (Klimes et al., 2010). Therefore, it is not surprising that the Δ*omcS* strain also forms filaments that were previously thought to be conductive type IV pili (Leang et al., 2010). Atomic force microscopy (AFM; Fig. 4A-E) revealed distinct structural features for WT *G. sulfurreducens* filaments versus the type IV pili of other species (Wang et al., 2017) and filaments from the Δ*omcS* strain (Leang et al., 2010). In contrast to the linear and smooth-surfaced structure of Δ*omcS* filaments, WT filaments exhibited an axial height periodicity with a 20-nm pitch (Fig. 4E), consistent with the helical pitch determined by cryo-EM (Fig. 1B). Filaments of the Δ*omcS* strain showed no apparent axial periodicity under AFM. Moreover, Δ*omcS* filament thickness (~1.7 nm height measured by AFM) was half that of WT filaments (~ 4 nm) (Fig. 4D,E). This substantial thickness difference and distinct axial periodicity observed for OmcS filaments was used to confirm that filaments studied for electrical measurements are the same OmcS nanowires characterized by cryo-EM.

AFM was further used to locate an individual OmcS filament bridging two gold electrodes (Fig. 4F, inset). Our DC conductivity measurements of individual OmcS filaments fully hydrated in buffer yielded values comparable to previous measurements of WT filaments (Adhikari et al., 2016), further suggesting that OmcS filaments are identical to the WT nanowires analysed in previous studies as Type IV pili. DC conductivity measurements of individual Δ*omcS* filaments showed a very low conductivity that was more than 100-fold lower than OmcS filaments (Fig. 4F,G). Our conductivity measurements thus show that OmcS is required for high conductivity of these ~4 nm-thick filaments.

Our finding that *G. sulfurreducens* nanowires are OmcS filaments is consistent with previous physiological studies. These studies highlight the importance of OmcS in extracellular electron transfer (Holmes et al., 2006; Leang et al., 2013; Leang et al., 2010; Mehta et al., 2005;

Summers et al., 2010). OmcS is one of the most abundant cytochromes found in the proteome for electricity-producing *G. sulfurreducens* and is required only during extracellular electron transfer to insoluble electron acceptors such as Fe (III) oxide (Holmes et al., 2006; Mehta et al., 2005). It is also critical for direct interspecies electron transfer between syntrophic *Geobacter* co-cultures as evolved co-culture overexpressed OmcS, and deletion of the *omcS* gene inhibited bacterial ability to exchange electrons (Summers et al., 2010).
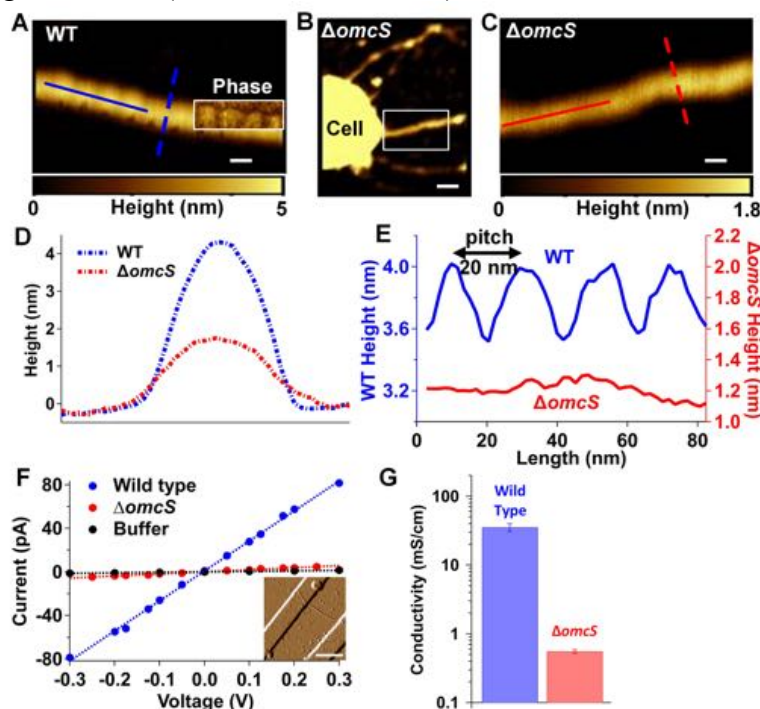
Figure. 4. Electrical measurements show that OmcS is required for filament conductivity. AFM height image of filaments from **(A)** WT strain **(B)** Δ*omcS* strain and **(C)** zoomed image of region shown in B. Inset in **A** is the phase image overlaid on height image that shows the repeating pattern. Scale bars: A, C, 20 nm; B, 100 nm. **(D)** The height profile for filaments of WT and Δ*omcS* strains using lateral cross section (dashed lines) in A and C. **(E)** Longitudinal height profile (solid lines in (A) and (C) for filaments of WT and Δ*omcS* strain. **(F)** Current-voltage profile for individual filaments of WT and Δ*omcS* strain compared to buffer alone. **Inset**: AFM images for filaments by Δ*omcS* strain across gold electrodes. Scale bar, 500 nm. **(G)** Comparison of DC conductivity (left) and carrier density (right) for filaments of WT and Δ*omcS* strains. Error bars represent S.E.M of three biological replicates.

OmcS also plays a critical role in long-range electron transport to electrodes in current-producing biofilms. Both microarray and quantitative reverse transcription polymerase chain reaction (qRT-PCR) analysis have demonstrated that cells show higher transcript levels for OmcS than for any other protein during the early stages of growth on electrodes (Holmes et al., 2006). Furthermore, immunogold localization has shown that OmcS is distributed throughout conductive *G. sulfurreducens* biofilms (Leang et al., 2013) and that deletion of the *omcS* gene inhibits electricity production (Holmes et al., 2006). However, the role of OmcS in conductivity was overlooked because Δ*omcS* biofilms were conductive and produced high current densities (Malvankar et al., 2011). These results might be due to a reciprocal relationship (Park and Kim, 2011) between the expression of OmcS and that of OmcZ, a cytochrome essential for current production (Nevin et al., 2009). The Δ*omcS* biofilms may compensate for the loss of OmcS by increasing the production of OmcZ.

Using immunogold localization, previous studies found that OmcS is associated with filaments (Leang et al., 2013; Leang et al., 2010; Summers et al., 2010). AFM images of filaments (Malvankar et al., 2012) as well as these antibody-labelling results (Leang et al., 2013; Leang et al., 2010; Summers et al., 2010) were interpreted as showing isolated OmcS monomers binding to the surfaces of the PilA filaments rather than showing antibodies directly binding to OmcS filaments. In light of the result presented here, a reinterpretation of these previous studies suggests that the antibodies may have been directly binding to the subunits of the OmcS filaments.

While no evidence of PilA was found in the structure of any of the purified filaments, non-filamentous PilA was present in our samples in lower abundance compared to OmcS, consistent with prior studies (Tan et al., 2016b). Multiple studies have shown that PilA is required for secretion of OmcS to the extracellular environment, as *pilA* deletion eliminated the presence of OmcS in outer-surface preparations (Liu et al., 2018; Richter et al., 2012). Overexpression of PilA is often accompanied by overproduction of OmcS and filaments (Leang et al., 2013; Summers et al., 2010), further suggesting that PilA is involved in secretion of OmcS filaments and explaining previous correlations found between PilA and biofilm conductivity (Malvankar et al., 2011). The requirement of PilA for the synthesis of OmcS filaments thus also explains the inability of Δ*pilA* cells to grow on insoluble electron acceptors such as Fe (III) oxides (Reguera et al., 2005) and electrodes (Reguera et al., 2006). A number of other bacteria have also been shown to require non-filamentous type IV pilins for the secretion of extracellular proteins (Hager et al., 2006). One possibility is that PilA is a pseudopilin as a part of a Type 2 Secretion System (T2SS) (Nivaskumar and Francetic, 2014), and OmcS is exported by this T2SS. Previous studies have shown that T2SS pseudopili could be secreted outside the cell (Nivaskumar and Francetic, 2014; Vignon et al., 2003). Similar mechanism could explain the presence of non-filamentous PilA in our filament preparations.

This potential ability of PilA to regulate the secretion and assembly of the OmcS nanowire as well as that of other multi-heme cytochromes (Liu et al., 2018; Richter et al., 2012) could explain how point mutations in *pilA* caused cells to produce filaments with different conductivities than wild-type (WT) filaments. Filaments produced by cells with point mutations in *pilA* showed very different morphology than WT filaments (Tan et al., 2016a). For example, substitution of two residues in PilA with tryptophan yielded mutant cells with filaments which surprisingly had half the diameter of WT filaments (Tan et al., 2016a). Based on our finding that conductive filaments are composed of cytochromes, this very large structural change in the filaments of mutant strains suggests that the observed change in conductivity may be due to filaments of different cytochromes or of different conformations of OmcS. Further structural studies on the filaments produced by these *pilA* mutants are needed to fully reconcile these studies with our finding of OmcS filaments functioning as nanowires.

2.4 CONCLUSIONS

Our findings show that conductive *G. sulfurreducens* filaments are polymerized chains of OmcS. The filament structure has hemes closely stacked along the micrometer-length of the filament, establishing the molecular basis for electronic conductivity in these nanowires. Functional characterization of conductivity in individual filaments shows that OmcS is required for the filament conductivity. This structure is surprising from a structural biology perspective and stands in contrast to the prevailing model in the field that conductive *G. sulfurreducens* appendages are type IV pili. The lack of type IV pili structures in these samples, from filament

preparations in two different labs and by two different cell growth and filament purification methods, call into question whether *G. sulfurreducens* makes type IV pili, let alone whether they are involved in conductivity. Nevertheless, the structure presented here provides a basis for re-evaluating previous work in the field and new insights into conductivity supramolecular protein nanowires. The advances in understanding of the structural basis for conductivity in microbial nanowires presented here can provide design principles for development of future bioelectronic interfaces between living cells and devices.

2.5 MATERIALS AND METHODS

Bacterial strains and growth conditions: The *Geobacter sulfurreducens* wild-type (WT) strain DL1 (ATCC 51573, DSMZ 12127) (Coppi et al., 2001) and the *omcS* deletion mutant strain (Mehta et al., 2005) (designated Δ*omcS*) were obtained from our laboratory culture collection. The cultures were maintained at 30 °C or at 25 °C under strictly anaerobic conditions in growth medium supplemented with acetate (10 mM) as the electron donor and fumarate (40 mM) as the electron acceptor in sterilized and degassed NBAF medium (O'Brien and Malvankar, 2017). 1L NBAF medium contained the following: 0.04 g/L calcium chloride dihydrate, 0.1 g /L, magnesium sulfate heptahydrate, 1.8 g/L sodium bicarbonate, 0.5 g/L sodium carbonate, 0.42 g/L potassium phosphate monobasic, 0.22 g/L potassium phosphate dibasic, 0.2 g/L ammonium chloride, 0.38 g/L potassium chloride, 0.36 g/L sodium chloride, vitamins and minerals as listed in (O'Brien and Malvankar, 2017). Resazurin was omitted and 1 mM cysteine was added as an electron scavenger. All chemicals obtained from Fisher Scientific unless otherwise noted. For filament samples used to build the atomic model, the wild-type strain was grown on electrodes under electron acceptor-limiting conditions that induce filament expression (O'Brien and Malvankar, 2017) (Fig. 1A).

G. sulfurreducens **filament preparation and biochemical characterization:** Filaments were separated from bacteria and extracted via centrifugation (Tan et al., 2016a) and maintained in 150 mM ethanolamine buffer at pH 10.5 in a manner similar to structural studies on bacterial filaments (Wang et al., 2017). Cells were gently scraped from the surface using a plastic spatula and isotonic wash buffer (20.02×10^{-3} M morpholinepropanesulfonic acid, 4.35×10^{-3} M $NaH_2PO_4 \cdot H_2O$, 1.34×10^{-3} M KCl, 85.56×10^{-3} M NaCl, 1.22×10^{-3} M $MgSO_4 \cdot 7H_2O$, and 0.07×10^{-3} M $CaCl_2 \cdot 2H_2O$), then collected by centrifugation and re-suspended in 150×10^{-3} M ethanolamine (pH 10.5). Filaments were mechanically sheared from the cell surface using a Waring Commercial Blender (Cat. No. 7011S) at low speed for 1 min, and then cells were removed by centrifugation at 13,000 g before collecting filaments with an overnight 10% ammonium sulfate precipitation and subsequent centrifugation at 13,000 g. Collected filaments were re-suspended in ethanolamine buffer then cleaned by centrifugation at 23,000 g to remove debris and a second 10% ammonium sulfate precipitation with centrifugation at 13,000 g (Tan et al., 2016a). The final filament preparation was re-suspended in 200 μl ethanolamine buffer. Filament preparations were further passed through 0.2 μm filters to remove any residual cells and stored at 4 °C. Cell-free filament preparations were imaged first with transmission electron microscopy to ensure sample quality (Fig. 1A). Dilute 5 μl solutions containing filaments were placed on gold electrodes to achieve individual filaments across two gold electrodes (Fig. 4F, Inset). Prior to all measurements, filaments were imaged with AFM and height measurements were performed to confirm the presence of individual filaments. For all conductivity measurements, samples were maintained under hydrated buffer environments (150

mM ethanolamine) and the pH of the buffer was equilibrated to pH 7 using HCl (Malvankar et al., 2011). Transmission electron microscopy imaging was used to confirm that filaments maintain their structure and remain morphologically similar at all pH conditions.

For polyacrylamide gel electrophoretic separation (SDS-PAGE), all filament samples were prepared in ethanolamine buffer and dried in a speedvac. Samples were then resuspended in 500 µl ultrapure deionized water and centrifuged at 18,000 x g at 4°C for 1 hour. The pellets were dried again in the speedvac, resuspended in water and dried repetitively 2 times. The final dried samples were resuspended in 5-8 µl 2.5% sodium-dodecyl sulphate (SDS) to disassemble filaments into their constituent monomers. The samples were incubated at room temperature for at least 4 hours, then diluted 3-fold with deionized water. The denatured samples were boiled in 1X SDS sample buffer that included b-mercaptoethanol for 12 min. The samples were run on a 16% Tricine protein gel (ThermoFisher Scientific, Carlsbad, CA) initially at constant voltage of 30 V for 18 minutes before changing to 190 V for 12 minutes. Precision Plus Protein Prestained molecular weight standards (BioRad, Hercules, CA) and Low Range Protein Ladder (Thermo Scientific) were used to compare the molecular weight of PilA and cytochromes in the filament preparations. Gels were immediately washed at least 3 times with ultra-pure deionized water over a 1-hour period, stained with Coomassie R-250 stain (Thermo Scientific, Rockford, IL), and destained overnight.

Custom monospecific anti-PilA antibody was synthesized by Pacific Immunology (Ramona, CA) by immunizing two rabbits with synthetic peptide sequence containing targeted epitope on the native protein, PilA, and then affinity purifying the serum against that peptide sequence. Specificity of antibody in the serum was confirmed by ELISA after 1st stage of immune response and then verified again with purified antibody (1:125,000 titer) at the final stage. Synthetic peptide sequence contained following 21 amino acids from C-terminus of PilA, Cys-RNLKTALESAFADDQTYPPES, to which a cysteine was added to N-terminus and then was conjugated with Keyhole Limpet Hemocyanin prior to immunization. The molecular weight of the synthetic peptide was verified by HPLC and ESI-MS.

For LC-MS/MS analysis of filaments, the PilA band (~ 6.5 kDa) and OmcS bands (~ 50 kDa and 30 kDa) were extracted from the protein gel and treated with trypsin to digest the protein. Proteomic analysis of the cleaved peptides from filaments of electrode-grown cells) was performed by the Proteomics Mass Spectrometry Facilities at Yale University Results gave unique amino acid sequence matches with the OmcS and *c*-terminal domain of PilA whereas the hydrophobicity of the N-terminal domain may have interfered with the sequence detection procedure (Ing et al., 2017).

Filament preparation from fumarate-grown cells: *G. sulfurreducens* was grown and used for filament purification (Ing et al., 2017). Briefly, *G. sulfurreducens* (DSMZ strain 12127) was grown anaerobically in 1 L cultures of sterilized and degassed NBAF medium (0.04 g/L calcium chloride dihydrate, 0.1 g/L magnesium sulphate heptahydrate, 1.8 g/L sodium bicarbonate, 0.5 g/L sodium carbonate, 0.42 g/L potassium phosphate monobasic, 0.22 g/L potassium phosphate dibasic, 0.2 g/L ammonium chloride, 0.38 g/L potassium chloride, 0.36 g/L sodium chloride, vitamins and minerals, using 20 mM acetate as the electron donor and 40 mM fumarate as the electron acceptor). Resazurin was omitted and 1mM cysteine was added as an electron scavenger. All chemicals were obtained from Fisher Scientific unless otherwise noted.

Upon reaching stationary phase, cells were pelleted by centrifugation at 5000 x *g* for 20 min at 4° C. Cell pellets were removed and extracellular filaments were purified from the

supernatant through dropwise additions of 1.1 M aqueous MgCl$_2$, which was added to a final ratio of 1:10 for aqueous MgCl$_2$:supernatant. Supernatants were stored at 4° C overnight and centrifuged at 50,000 x g for 1 h at 4° C to precipitate extracellular filaments. Pellets of extracellular filaments were resuspended with ultrapure water adjusted to pH 4.3 with HCl and passed through 0.2 μm filters. Additional contaminants were removed from the resuspended pellets using 50 kDa dialysis tubing. After two 1 L exchanges of pH 4.3 water, the dialyzed sample was removed from dialysis tubing and stored at 4° C.

For analysis of filaments from fumarate-grown cells, the purified filament samples were analysed for protein content by 12.5% PhastGel (GE Healthcare) and stained with Coomassie. There were two prominent protein bands around 47 kDa, and these were cut from the gel, digested by trypsin overnight, and then analysed by mass spec at the University of Virginia core facility. The LC-MS system consisted of a Thermo Electron Q Exactive HFX mass spectrometer system with an Easy Spray ion source connected to a Thermo 75 μm x 15 cm C18 Easy Spray column. 5 μL of the extract was injected and the peptides eluted from the column by an acetonitrile/0.1 M formic acid gradient at a flow rate of 0.3 μL/min over 2.0 hours. The nanospray ion source was operated at 1.9 kV. The digest was analysed using the rapid switching capability of the instrument acquiring a full scan mass spectrum to determine peptide molecular weights followed by product ion spectra (10 HCD) to determine amino acid sequence in sequential scans. This mode of analysis produces approximately 60,000 MS/MS spectra of ions ranging in abundance over several orders of magnitude.

Prior to use, purified filaments were characterized by MALDI-TOF. For MALDI-TOF analysis, filaments were denatured with 10% OG overnight and then diluted with ultrapure water to a final OG concentration of 2% prior to the addition of matrix solution (α-Cyano-4-hydroxycinnamic acid dissolved in a 2:1 solution of ultrapure water: acetonitrile and 0.2% trifluoroacetic acid). The final sample for MALDI was a 12:7:5 ratio of matrix solution to ultrapure water to diluted and denatured protein. Mass spectra were collected in positive ion mode.

Cryo-EM sample preparation conditions: For samples used to build the atomic model, holey carbon coated Quantifoil grids (R 2μm/2μm) were used. Prior to use, the grids were floated in 0.05% Triton 100X solution (Cheung et al., 2013). Cryo-EM specimens were prepared with a FEI Vitrobot Mark IV at 22 °C with 100% humidity. 3 μL of sample solution containing WT filaments were dropped on the grids and spread gently by pipette tip before loading to the Vitrobot, blotted for 5.5 s and plunged freezing in liquid ethane.

Cryo-EM data collection conditions: Micrographs were acquired by FEI Titan Krios electron microscopy performed at 300kV equipped with a Gatan K2 summit camera. Quantum energy filter with a slit width at 20 eV was applied to remove inelastically scattered electrons. Movies were collected using super-resolution imaging mode with a physical pixel size of 1.05 Å and an exposure rate of 6.8 electrons per pixel per second. A total exposure time of 9.75 seconds was fractioned into 30 frames and 1447 movies were generated using serial EM auto-collection. The data collection and processing parameters are summarized below:

Magnification	130,000 X
Voltage (kV)	300
Electron exposure (e$^-$/Å^2)	63

Energy filter slit width	20 eV
Physical Pixel Size (Å)	1.05
Defocus range (μm)	0.5 – 3.0

For analysis of filaments from fumarate-grown cells, sample (4 μL, ~1 μg/μl) was applied to discharged lacey carbon grids and plunged frozen using a Vitrobot Mark IV (FEI, Inc.). Grids were imaged in a Titan Krios at 300 keV and recorded with a Falcon III direct electron detector at 1.4 Å per pixel. Micrographs were collected using a defocus range of 1.25–2.25 μm, with a total exposure of 2 s (amounting to ~ 60 electrons/$Å^2$) distributed into 24 fractions. All the micrographs were first motion corrected (ignoring the first fraction) using MotionCorr (Li et al., 2013) version 2 and then used for CTF estimation by the CTFFIND3 program (Mindell and Grigorieff, 2003).

Cryo-EM image analysis: For filaments of fumarate-grown cells, images were extracted using the e2helixboxer program within EMAN2 (Tang et al., 2007) from the dose-weighted fractions 2-10 (amounting to ~ 20 electrons/$Å^2$), after the images were corrected for the CTF through multiplication by the theoretical CTF (a Wiener filter in the limit of a very poor SNR). A total of 17,800 overlapping 384-px long segments (with a shift of 55 pixels, ~ 1.5 times the axial rise per subunit) were generated. The determination of the helical symmetry was unambiguous given the 1/(47 Å) meridional layer-line and the 1-start helix of ~ 200 Å pitch. A reconstruction was generated using the IHRSR method implemented in Spider (Egelman, 2000), and this reconstruction was subsequently filtered to 20 Å for the starting reference in the reconstruction of the second dataset. To build the atomic model of filaments from electrode-grown cells, a total of 573 images were selected, motion-corrected, dose weighted (amounting to ~ 20 electrons/$Å^2$) and CTF-corrected in the same manner as for filaments of electrode-grown cells. About 2,000 long filaments were extracted using e2helixboxer and then 384-pixel long 28,293 overlapping segments with a shift of 60 pixels were generated. The final volume from the IHRSR reconstruction was estimated to have a resolution of ~ 3.7 Å based on the model:map FSC. It was filtered to 3.6 Å and sharpened with a negative B-factor of 100. Micrographs with all fractions and boxing coordinates were also imported into Relion for 3D reconstruction. A similar final reconstruction to the one from SPIDER was generated in Relion using the same helical symmetry, starting with the SPIDER volume filtered to 10 Å. Interestingly this reconstruction was estimated to have a resolution of 3.2 Å resolution based on a "gold standard" map:map FSC.

Model building of OmcS filaments: First, about 400 protein C_α atoms and six heme cofactors corresponding to a single subunit within the filaments were built manually in Coot (Emsley and Cowtan, 2004). Then the density corresponding to a single subunit was segmented from the experimental filament density using Chimera (Pettersen et al., 2004). Using the proteins identified in the MS/MS results and real space fitting to the cryo-EM density, the sequence of the filament was unambiguously determined to be cytochrome OmcS. The full length OmcS protein as well as six heme molecules were then built manually in Coot. Then the OmcS/heme was rebuilt with the RosettaCM protocol (Wang et al., 2015) to remove bad geometries. A total of 3,000 full-length models were generated and the top 20 models were selected based on Rosetta's energy function, Ramachandran plots and overall fit to the map. These 20 models were then combined into one model by manual editing in Coot using the criteria of the local fit to the density map and the geometry statistics of the model. To better refine heme interacting areas at this resolution, bond/angle restraints for the heme molecule itself, His-Fe, and Cys-heme

thioester bonds were created based on high resolution cytochrome c3 crystal structures NrfB (PDB 2P0B) and NrfHA (PDB 2J7A). Then a filament model was generated and further refined using Phenix with additional heme area restraints, and MolProbity (Williams et al., 2018) was used to evaluate the quality of the filament model. The refinement statistics are given in Table 1.

Atomic force microscopy (AFM): To visualize individual filaments, 5 µl of buffer solution containing filaments were deposited on mica or on a silicon wafer insulated by a 100 nm silicon dioxide dielectric layer with gold electrodes patterned by nanoimprint lithography (Tan et al., 2016a). For nanoimprinting, the substrate was cleaned with a Piranha solution (H_2SO_4:H_2O_2 = 3:1) and a diluted Hydrofluoric acid solution before patterning. Two layers of resists (50-nm-thick poly methyl methacrylate and 60-nm-thick UV-curable resist) were then sequentially spin-coated onto the cleaned substrate. Circuit patterns including nanoelectrodes separated by nano-sized gaps, microscale fan outs, and contact pads were transferred from a quartz mold to the UV resist with nanoimprint lithography in a homemade imprint chamber. The residual UV-resist layer and the poly methyl methacrylate underlayer were removed by reactive ion etching with fluorine based (CHF_3/O_2) and oxygen-based gases respectively. The excess buffer was absorbed with filter paper. The sample was air-dried and was mounted on a metal puck (Oxford Instrument, Cypher ES). AFM experiments were performed using soft cantilevers (ASYELEC-01, Oxford Instrument Co.) with a nominal force constant of 2 N/m and resonance frequencies of 70 KHz. The free-air amplitude of the tip was calibrated with the Asylum Research software and the spring constant was captured by the thermal vibration method. The sample was imaged with a Cypher ES scanner using intermittent tapping (AC-air topography) mode. AFM showed that gold electrodes were bridged with individual filaments to facilitate conductivity measurements (Fig. 4F, inset). To visualize helical features of filaments, higher-resolution AFM was performed in attractive force imaging mode.

Direct current (DC) conductivity measurements: All DC conductivity measurements of filaments were performed under fully hydrated buffer conditions in a 2-electrode configuration inside a triaxially shielded dark box using a probe station (MPI Corp.) connected to a semiconductor parameter analyser (Keithley 4200A-SCS) equipped with preamplifiers, allowing 0.1 fA current resolution and 0.5 µV voltage resolution. A DC voltage, typically in the range of -0.5V to +0.5V, was applied between the two electrodes and the current was measured over a minimum period of 120 seconds until the steady state was reached. The linearity of the *I-V* characteristics was maintained by applying an appropriate low voltage and the slope of the *I-V* curve was used to determine the conductance (*G*). Measurements were performed at low voltages (< 0.5 V) and over longer times (> 100 seconds) to ensure a lack of electrochemical leakage currents or faradic currents as evidenced by the absence of significant DC conductivity in buffer or filaments of Δ*omcS* strain that were maintained under identical buffer conditions as filaments of the WT strain (Fig. 4F,G). All analysis was performed using IGOR Pro (WaveMetrics Inc.).

Conductivity calculations: The conductivity (*σ*) of filaments was calculated using the relation (Malvankar et al., 2011) $\sigma = G \cdot (L/A)$ where *G* is the conductance, *L* is the length of the filament, and $A = \pi r^2$ is the area of cross section of filament with 2*r* as the height of the filament measured by AFM (Fig. 4F,G).

2.6 REFERENCES

Adhikari, R., Malvankar, N., Tuominen, M., and Lovley, D. (2016). Conductivity of individual *Geobacter* pili. RSC Advances *6*, 8354 - 8357.

Afkar, E., Reguera, G., Schiffer, M., and Lovley, D.R. (2005). A novel *Geobacteraceae*-specific outer membrane protein J (OmpJ) is essential for electron transport to Fe (III) and Mn (IV) oxides in *Geobacter sulfurreducens*. BMC microbiology *5*, 41-41.

Ashkenazy, H., Abadi, S., Martz, E., Chay, O., Mayrose, I., Pupko, T., and Ben-Tal, N. (2016). ConSurf 2016: an improved methodology to estimate and visualize evolutionary conservation in macromolecules. Nucleic Acids Research *44*, W344-W350.

Bertini, I., Cavallaro, G., and Rosato, A. (2006). Cytochrome *c*: occurrence and functions. Chemical Reviews *106*, 90-115.

Cheung, M., Kajimura, N., Makino, F., Ashihara, M., Miyata, T., Kato, T., Namba, K., and Blocker, A.J. (2013). A method to achieve homogeneous dispersion of large transmembrane complexes within the holes of carbon films for electron cryomicroscopy. Journal of Structural Biology *182*, 51-56.

Childers, S.E., Ciufo, S., and Lovley, D.R. (2002). Geobacter metallireducens accesses insoluble Fe(iii) oxide by chemotaxis. Nature *416*, 767-769.

Clarke, T.A., Edwards, M.J., Gates, A.J., Hall, A., White, G.F., Bradley, J., Reardon, C.L., Shi, L., Beliaev, A.S., Marshall, M.J.*, et al.* (2011). Structure of a bacterial cell surface decaheme electron conduit. Proceedings of the National Academy of Sciences *108*, 9384-9389.

Egelman, E.H. (2000a). A robust algorithm for the reconstruction of helical filaments using single-particle methods. Ultramicroscopy *85*, 225-234.

Egelman, E.H. (2000b). A robust algorithm for the reconstruction of helical filaments using single-particle methods. Ultramicroscopy *85*, 225-234.

Emsley, P., and Cowtan, K. (2004). Coot: model-building tools for molecular graphics. Acta Crystallographica Section D *60*, 2126-2132.

Hager, A.J., Bolton, D.L., Pelletier, M.R., Brittnacher, M.J., Gallagher, L.A., Kaul, R., Skerrett, S.J., Miller, S.I., and Guina, T. (2006). Type IV pili-mediated secretion modulates *Francisella virulence*. Molecular Microbiology *62*, 227-237.

Haldar, S., Sil, P., Thangamuniyandi, M., and Chattopadhyay, K. (2014). Conversion of amyloid fibrils of cytochrome c to mature nanorods through a honeycomb morphology. Langmuir *31*, 4213-4223.

Hirota, S., Hattori, Y., Nagao, S., Taketa, M., Komori, H., Kamikubo, H., Wang, Z., Takahashi, I., Negi, S., and Sugiura, Y. (2010). Cytochrome c polymerization by successive domain

swapping at the C-terminal helix. Proceedings of the National Academy of Sciences *107*, 12854-12859.

Holmes, D.E., Chaudhuri, S.K., Nevin, K.P., Mehta, T., Methe, B.A., Liu, A., Ward, J.E., Woodard, T.L., Webster, J., and Lovley, D.R. (2006). Microarray and genetic analysis of electron transfer to electrodes in *Geobacter sulfurreducens*. Environmental Microbiology *8*, 1805-1815.

Ing, N.L., Nusca, T.D., and Hochbaum, A.I. (2017). *Geobacter sulfurreducens* pili support ohmic electronic conduction in aqueous solution. Physical Chemistry Chemical Physics *19*, 21791-21799.

Inoue, K., Qian, X., Morgado, L., Kim, B., Mester, T., Izallalen, M., Salgueiro, C., and Lovley, D. (2010). Purification and characterization of omcZ, an outer-surface, octaheme *c*-type cytochrome essential for optimal current production by *Geobacter sulfurreducens*. Applied and Environmental Microbiology *76*, 3999-4007.

Janiak, C. (2000). A critical account on π-π stacking in metal complexes with aromatic nitrogen-containing ligands. Journal of the Chemical Society, Dalton Transactions, 3885-3896.

Jiang, X., Futera, Z., Ali, M.E., Gajdos, F., von Rudorff, G.F., Carof, A., Breuer, M., and Blumberger, J. (2017). Cysteine linkages accelerate electron flow through tetra-heme protein STC. Journal of the American Chemical Society *139*, 17237-17240.

Klimes, A., Franks, A.E., Glaven, R.H., Tran, H., Barrett, C.L., Qiu, Y., Zengler, K., and Lovley, D.R. (2010). Production of pilus-like filaments in Geobacter sulfurreducens in the absence of the type IV pilin protein PilA. FEMS Microbiology Letters *310*, 62-68.

Leang, C., Malvankar, N.S., Franks, A.E., Nevin, K.P., and Lovley, D.R. (2013). Engineering *Geobacter sulfurreducens* to produce a highly cohesive conductive matrix with enhanced capacity for current production. Energy & Environmental Science *6*, 1901-1908.

Leang, C., Qian, X.L., Mester, T., and Lovley, D.R. (2010). Alignment of the *c*-type cytochrome OmcS along pili of *Geobacter sulfurreducens*. Applied and Environmental Microbiology *76*, 4080-4084.

Li, X., Mooney, P., Zheng, S., Booth, C.R., Braunfeld, M.B., Gubbens, S., Agard, D.A., and Cheng, Y. (2013). Electron counting and beam-induced motion correction enable near-atomic-resolution single-particle cryo-EM. Nature Methods *10*, 584.

Liu, X., Zhuo, S., Rensing, C., and Zhou, S. (2018). Syntrophic growth with direct interspecies electron transfer between pili-free Geobacter species. The ISME Journal.

Malvankar, N.S., and Lovley, D.R. (2014). Microbial nanowires for bioenergy applications. Current Opinion in Biotechnology *27*, 88-95.

Malvankar, N.S., Tuominen, M.T., and Lovley, D.R. (2012). Lack of cytochrome involvement in long-range electron transport through conductive biofilms and nanowires of *Geobacter sulfurreducens*. Energy & Environmental Science *5*, 8651-8659.

Malvankar, N.S., Vargas, M., Nevin, K.P., Franks, A.E., Leang, C., Kim, B.C., Inoue, K., Mester, T., Covalla, S.F., Johnson, J.P.*, et al.* (2011). Tunable metallic-like conductivity in microbial nanowire networks. Nature Nanotechnology *6*, 573-579.

Margoliash, E., and Lustgarten, J. (1962). Interconversion of horse heart cytochrome *c* monomer and polymers. Journal of Biological Chemistry *237*, 3397-3405.

Marsili, E., Baron, D.B., Shikhare, I.D., Coursolle, D., Gralnick, J.A., and Bond, D.R. (2008). *Shewanella* secretes flavins that mediate extracellular electron transfer. Proceedings of the National Academy of Sciences *105*, 3968-3973.

Mehta, T., Coppi, M.V., Childers, S.E., and Lovley, D.R. (2005). Outer membrane *c*-type cytochromes required for Fe (III) and Mn (IV) oxide reduction in *Geobacter sulfurreducens*. Applied and Environmental Microbiology *71*, 8634-8641.

Mindell, J.A., and Grigorieff, N. (2003). Accurate determination of local defocus and specimen tilt in electron microscopy. Journal of Structural Biology *142*, 334-347.

Neumann, P., Dickmanns, A., and Ficner, R. (2018). Validating resolution revolution. Structure *26*, 785-795. e784.

Nevin, K.P., Kim, B.C., Glaven, R.H., Johnson, J.P., Woodard, T.L., Methé, B.A., DiDonato Jr, R.J., Covalla, S.F., Franks, A.E., Liu, A.*, et al.* (2009). Anode biofilm transcriptomics reveals outer surface components essential for high density current production in *Geobacter sulfurreducens* fuel cells. PLoS ONE *4*, e5628.

Nivaskumar, M., and Francetic, O. (2014). Type II secretion system: A magic beanstalk or a protein escalator. Biochimica et Biophysica Acta (BBA) - Molecular Cell Research *1843*, 1568-1577.

O'Brien, J.P., and Malvankar, N.S. (2017). A simple and low-cost procedure for growing *Geobacter sulfurreducens* cell cultures and biofilms in bioelectrochemical systems. Current Protocols in Microbiology *43*, A.4K.1-A.4K.27.

Park, I., and Kim, B.-C. (2011). Homologous overexpression of omcZ, a gene for an outer surface c-type cytochrome of Geobacter sulfurreducens by single-step gene replacement. Biotechnology Letters *33*, 2043.

Pettersen, E.F., Goddard, T.D., Huang, C.C., Couch, G.S., Greenblatt, D.M., Meng, E.C., and Ferrin, T.E. (2004). UCSF Chimera—a visualization system for exploratory research and analysis. Journal of Computational Chemistry *25*, 1605-1612.

Qian, X., Mester, T., Morgado, L., Arakawa, T., Sharma, M.L., Inoue, K., Joseph, C., Salgueiro, C.A., Maroney, M.J., and Lovley, D.R. (2011). Biochemical characterization of purified OmcS, a c-type cytochrome required for insoluble Fe(III) reduction in Geobacter sulfurreducens. Biochimica et Biophysica Acta (BBA) - Bioenergetics *1807*, 404-412.

Reardon, P.N., and Mueller, K.T. (2013). Structure of the type IVa major pilin from the electrically conductive bacterial nanowires of *Geobacter sulfurreducens*. Journal of Biological Chemistry *288*, 29260-29266.

Reguera, G., McCarthy, K.D., Mehta, T., Nicoll, J.S., Tuominen, M.T., and Lovley, D.R. (2005). Extracellular electron transfer via microbial nanowires. Nature *435*, 1098-1101.

Reguera, G., Nevin, K.P., Nicoll, J.S., Covalla, S.F., Woodard, T.L., and Lovley, D.R. (2006). Biofilm and nanowire production leads to increased current in Geobacter sulfurreducens fuel cells. Applied and environmental microbiology *72*, 7345-7348.

Reguera, G., Pollina, R.B., Nicoll, J.S., and Lovley, D.R. (2007). Possible nonconductive role of *Geobacter sulfurreducens* pilus nanowires in biofilm formation. Journal of Bacteriology *189*, 2125-2127.

Richter, L.V., Sandler, S.J., and Weis, R.M. (2012). Two isoforms of *Geobacter sulfurreducens* PilA have distinct roles in pilus biogenesis, cytochrome localization, extracellular electron transfer, and biofilm formation. Journal of Bacteriology *194*, 2551-2563.

Scheres, S.H. (2012). RELION: implementation of a Bayesian approach to cryo-EM structure determination. Journal of Structural Biology *180*, 519-530.

Subramaniam, S., Earl, L.A., Falconieri, V., Milne, J.L., and Egelman, E.H. (2016). Resolution advances in cryo-EM enable application to drug discovery. Current Opinion in Structural Biology *41*, 194-202.

Summers, Z.M., Fogarty, H.E., Leang, C., Franks, A.E., Malvankar, N.S., and Lovley, D.R. (2010). Direct exchange of electrons within aggregates of an evolved syntrophic coculture of anaerobic bacteria. Science *330*, 1413-1415.

Tan, Y., Adhikari, R.Y., Malvankar, N.S., Pi, S., Ward, J.E., Woodard, T.L., Nevin, K.P., Xia, Q., Tuominen, M.T., and Lovley, D.R. (2016a). Synthetic biological protein nanowires with high conductivity. Small *12*, 4481–4485.

Tan, Y., Adhikari, R.Y., Malvankar, N.S., Ward, J.E., Nevin, K.P., Woodard, T.L., Smith, J.A., Snoeyenbos-West, O.L., Franks, A.E., Tuominen, M.T.*, et al.* (2016b). The low conductivity of *Geobacter uraniireducens* pili suggests a diversity of extracellular electron transfer mechanisms in the genus *Geobacter*. Frontiers in Microbiology *7*, 980.

Tan, Y., Adhikari, R.Y., Malvankar, N.S., Ward, J.E., Woodard, T.L., Nevin, K.P., and Lovley, D.R. (2017). Expressing the *Geobacter metallireducens* PilA in *Geobacter sulfurreducens* yields pili with exceptional conductivity. mBio *8*.

Tang, G., Peng, L., Baldwin, P.R., Mann, D.S., Jiang, W., Rees, I., and Ludtke, S.J. (2007). EMAN2: An extensible image processing suite for electron microscopy. Journal of Structural Biology *157*, 38-46.

Ueki, T., Leang, C., Inoue, K., and Lovley, D.R. (2012). Identification of multicomponent histidine-aspartate phosphorelay system controlling flagellar and motility gene expression in *Geobacter* species. Journal of Biological Chemistry *287*, 10958-10966.

Vargas, M., Malvankar, N.S., Tremblay, P.L., Leang, C., Smith, J., Patel, P., Synoeyenbos-West, O., Nevin, K.P., and Lovley, D.R. (2013). Aromatic amino acids required for pili conductivity and long-range extracellular electron transport in *Geobacter sulfurreducens*. mBio *4*, e00105-00113.

Vignon, G., Köhler, R., Larquet, E., Giroux, S., Prévost, M.-C., Roux, P., and Pugsley, A.P. (2003). Type IV-Like Pili Formed by the Type II Secreton: Specificity, Composition, Bundling, Polar Localization, and Surface Presentation of Peptides. Journal of Bacteriology *185*, 3416-3428.

Wang, F., Coureuil, M., Osinski, T., Orlova, A., Altindal, T., Gesbert, G., Nassif, X., Egelman, E.H., and Craig, L. (2017). Cryoelectron microscopy reconstructions of the *Pseudomonas aeruginosa* and *Neisseria gonorrhoeae* type IV pili at sub-nanometer resolution. Structure *25*, 1423-1435.

Wang, R.Y.-R., Kudryashev, M., Li, X., Egelman, E.H., Basler, M., Cheng, Y., Baker, D., and DiMaio, F. (2015). De novo protein structure determination from near-atomic-resolution cryo-EM maps. Nature Methods *12*, 335.

Williams, C.J., Headd, J.J., Moriarty, N.W., Prisant, M.G., Videau, L.L., Deis, L.N., Verma, V., Keedy, D.A., Hintze, B.J., Chen, V.B.*, et al.* (2018). MolProbity: More and better reference data for improved all-atom structure validation. Protein Science *27*, 293-315.

Design and Structure of a Coiled-Coil Hexamer Scaffold for Redox Amino Acids.

3.1 SUMMARY

The self-assembly of peptides and proteins into higher-ordered structures is encoded in the amino acid sequence of each peptide or protein. Understanding the relationship between amino acid sequence, the assembly dynamics, and structure of well-defined peptide oligomers expands the synthetic toolbox for these structures. Here, we present the X-ray crystallographic structure and solution behavior of de novo peptides that form antiparallel coiled-coil hexamers (ACC-Hex) by an interaction motif neither found in nature nor predicted by existing peptide design software. We designed these peptides to arrange redox species, in this case phenyl groups, in an ordered chain along the axis of the hexamer with a view towards using these hexamers as building blocks for conductive fiber assembly, inspired by conductive bacterial appendages. The 1.70 Å X-ray crystallographic structure of peptide 1a shows six α-helices associating in an antiparallel arrangement around a central axis comprising hydrophobic and aromatic residues. SEC studies suggest that peptide 1 form stable oligomers in solution, and CD experiments show that peptides 1 are stable to relatively high temperatures. SAXS studies on the solution behavior of peptide 1a indicate an equilibrium of dimers, hexamers, and larger aggregates in solution. The structures presented here represents a new motif of biomolecular self-assembly not previously observed for de novo peptides and suggests supramolecular design principles for material scaffolds based on coiled-coil motifs containing aromatic residues.

3.2 INTRODUCTION

The self-assembly of peptides and proteins to form higher-ordered structures is determined by the amino acid sequence within the polypeptide. The ability of a polypeptide sequences to fold into secondary, tertiary, and quaternary structures is dictated by the interactions among the side chains of the amino acids within the polypeptide. Nature has created a diverse library of functional peptides and proteins ranging from simple neurotransmitters to complex multidomain enzymes. Designing de novo polypeptides that recapitulate or expand the properties of peptides and proteins found in nature without relying on the sequences derived directly from nature has been difficult.

Substantial progress for de novo peptides has been made in the design of polypeptide sequences that adopt α-helices and associate further to form coiled coils.[1–3] The formation of coiled coils from the assembly of α-helices was first predicted over 60 years ago for naturally occurring proteins and peptides.[4] De novo peptides that fold into coiled coils have proven to be a robust scaffold with interesting properties.[5–10] *De novo* coiled coils can be de- signed to associate into diverse supramolecular assemblies including dimers,[11–14] trimers,[15,16] tetramers,[17–19] pentamers,[20–22] hexamers,[23] and larger assemblies.[3,24] De novo coiled coils have also been designed to form fibers,[12,13,25,26] act as enzymes,[27] and mimic membrane transport proteins.[28]

Coiled-coil sequences often contain heptad amino acid repeats where residue positions within the heptad are described by an *a-b-c-d-e-f-g* pattern. Variation of the size, hydrophobicity, and placement of the amino acids within the repeating heptad pattern can impact supramolecular assembly. Patterned interactions between the side chains of the amino acids, often called knobs-

into-holes (KIH), along the interior surface of the α-helices dictate the oligomerization of the coiled coils.[4] While advances in computer software have helped guide researchers in the development of de novo peptide assemblies,[29–37] predicting the supramolecular assembly based on a peptide sequence remains challenging. More experimental exploration is needed to better understand how de novo peptides assemble into homogeneous oligomers, which will allow better control of their molecular properties. The discovery of new interaction motifs, therefore, opens new areas for study in peptide self-assembly.

The development of larger assemblies from de novo coiled-coil motifs showed a progression of expanding the KIH interactions by incorporating additional hydrophobic residues along the inner surfaces of the interacting α-helices while also incorporating hydrophilic residues along the outer surfaces. Hydrophobic residues such as Val, Leu, or Ile are used in conjunction with Ala residues at adjacent positions along the interacting surfaces of the α-helices to expand the KIH interactions. The design of de novo coiled coils that contain interdigitating hydrophobic residues has been used to create tetramers, pentamers, and most recently hexamers.[17–23] With a few exceptions,[20,22,38] most coiled-coil designs lack repeating patterns of amino acids with aromatic side chains. Moreover, α-helices containing bundles of aromatic residues have been implicated as an important feature in certain classes of bacterial pili, some of which being capable of transporting electrical current.[39–43] To further explore this structural space we designed a coiled-coil motif that contains repeating aromatic residues along the hydrophobic coiled-coil interface.

Ac-ELKAIAQE**F**KAIAKE**F**KAIAWE**F**KAIAQK-NH$_2$
abcdefgabcdefgabcdefgabcdefg
peptide **1a**
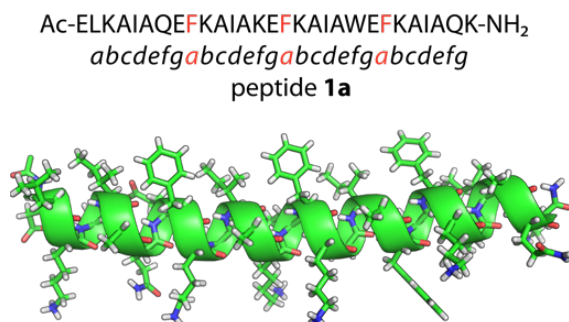
Figure 1: Sequence of peptide 1a and X-ray crystallographic structure of an α-helix monomer formed by peptide 1a.

We designed a new coiled-coil motif to incorporate Phe residues, fold to adopt α-helix, and assemble into a supramolecular structure. The sequence was adapted from a parallel coiled-coil hexamer developed by the Woolfson lab, termed CC-Hex, to explore the oligomers formed by coiled coils containing aromatic residues.[23] Peptide 1a contains four heptad repeats with a sequence of L/F-K-A-I-A-X-E (Figure 1). In CC-Hex, six α-helices associate symmetrically along a hydrophobic surface containing Leu and Ile residues. The parallel arrangement of each α-helix in CC-Hex creates alternating layers of Leu or Ile along the axis of the hydrophobic core. To not perturb the hydrophobic core substantially, we kept the Ile residue at the d positions and replaced three of the four Leu residues at the a positions with the hydrophobic Phe residue. Hydrophilic Glu and Lys residues were placed at the solvent-exposed b and g positions to promote solubility. We added a Glu residue at the N-terminus and Lys residue at the C-terminus to help promote higher-ordered assemblies between hexamer units. Peptide 1b was designed as

an analogue to peptide 1a and contained a p-iodophenylalanine in place of the Trp residue to facilitate crystal structure determination.

3.3 RESULTS
3.3.1 Synthesis and X-ray crystallographic structure of designed peptides:

We synthesized peptides 1 using standard Fmoc-based solid-phase peptide synthesis. Pep- tides 1 were acetylated, deprotected, and then purified by RP-HPLC. The optimal concentration for the crystallization of peptide 1b was determined using the Hampton Precrystallization Test. Conditions appropriate for crystal growing were determined using the Hampton Research crystallization kits: Crystal Screen, Index, and PEG/Ion (864 experiments). Pep- tide 1b crystallizes from wells containing 0.1 M sodium formate buffer (pH 6.75 – 7.3) and PEG 3350 (25 – 28%). Peptide 1a crystallizes in similar conditions to that of peptide 1b, with diffraction quality crystals forming from 0.1 M sodium formate, pH 7.3 and 29% PEG 3350. Crystal diffraction data were collected at the Advanced Light Source at the Lawrence Berkeley National Laboratory with a synchrotron source at 0.977 Å and to a resolution of 1.70 Å for peptide 1a and 2.10 Å for peptide 1b.

We determined the crystallographic phases of the electron density map for peptide 1a using a single α-helix derived from the crystal structure of peptide 1b. A single α-helix derived from the crystal structure of peptide 1b was used as a search model in the program Phaser to determine the initial phases of the electron density map.[55] Two additional α-helices were placed automatically by Phaser after the placement of the initial α-helix. We used the pro- gram Autosol in the Phenix software suite to perform rounds of automated model building and electron density modification.[60] The crystallographic model was subjected to subsequent rounds of manipulation using the program Coot and refinement using the phenix.refine program.[53,54] Coordinates for hydrogen atoms were refined as "riding" and were generated by phenix.refine during refinement.

Peptide 1a crystallizes in the $P4_22_12$ space group, with three nearly identical α-helix monomers in the asymmetric unit (ASU) (Table 1). Expanding the ASU reveals hexamers comprising six α-helices. The α-helices are arranged in an antiparallel fashion around a central axis that runs through the center of the hexamer (Figure 2). Peptide 1a folds to adopt an α-helix with each heptad repeat forming two full-turns within the helix. Four heptad repeats create an extended α-helix with all 29 residues adopting an α-helix conformation (Figure 2). Analysis of peptide 1a with the program Coiled-Coil Crick Parameterization (CCCP) reveals that the antiparallel coiled-coil hexamer is left-handed, with a superhelical frequency of -3.08° per residue, and completing a full turn of the superhelix in 117 residues.[32] Each α-helix associates with two other α-helices in an antiparallel conformation. The C-terminus of each α-helix is offset by an avg. of 6.5 Å along the central axis of the hexamer from the neighboring N-termini of the α-helices (Figure 2A). This leads to a staggering of the α-helices at the ends of the hexamer, with three α-helices aligned at the same height and three α-helices shifted 6.5 Å lower.

The Phe and Ile residues at the a and d positions within the heptad repeat form the hydrophobic core of the hexamer. Three Phe and three Ile residues form a hydrophobic layer in which the Phe and Ile residues alternate in an a-d-a-d-a-d pattern around the hexamer core (Figures 2C and 2D and 3). Analysis of the KIH interactions using the program SOCKET reveals that the antiparallel hexamers contain type III and IV KIH interactions.[61] The Ile and Ala residues at the d and e positions within the heptad are involved in type IV interactions with the adjacent Glu, Phe, and Lys residues. The Phe residues are involved in type III KIH interactions and act as knobs in the hole generated by Ile and Ala residues in the d and e positions.

Table 1: Crystallographic Properties, Crystallization Conditions, and Data Collection and Model Refinement Statistics for Peptides 1.
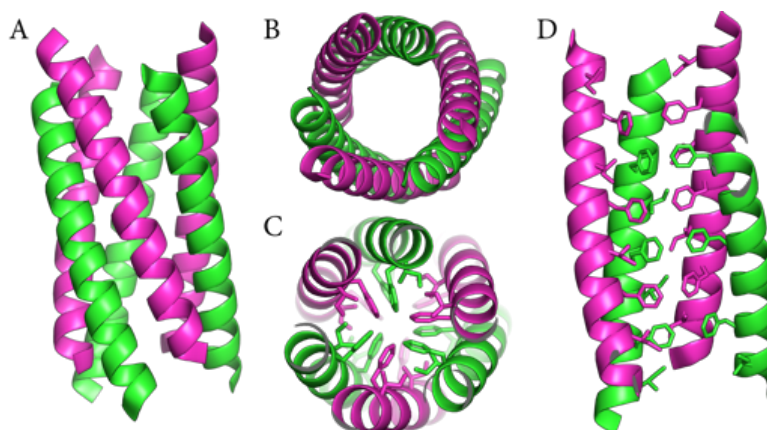
	peptide **1a**	peptide **1b**
PDB ID	5EON	5EOJ
space group	$P4_22_12$	$P4_322$
a, b, c (Å)	59.26 59.26 52.52	40.85 40.85 118.15
α, β, γ (°)	90 90 90	90 90 90
peptide per asymmetric unit	3	3
crystallization conditions	0.1 M sodium formate, pH 7.3, 28% PEG 3350	0.1 M sodium formate, pH 6.75-7.3 25-28% PEG 3350
Data Collection[1]		
wavelength (Å)	0.977	0.977
resolution (Å)	32.75–1.70 (1.76–1.70)	38.61–2.12 (2.19–2.12)
total reflections	21525 (1925)	12488 (1214)
unique reflections	10805 (1005)	6246 (608)
multiplicity	2.0	2.0
completeness (%)	100 (96)	98 (99)
mean I/σ	31.70 (3.42)	13.42 (1.12)
Wilson B-factor	28.57	46.68
R_{merge}	0.008 (0.19)	0.026 (0.45)
$R_{measure}$	0.012	0.037
$CC_{1/2}$	1.00 (0.90)	0.98 (0.73)
CC^*	1.00 (0.97)	0.99 (0.92)
Refinement		
R_{work}	19.80	24.63
R_{free}	22.17	27.68
number of non-hydrogen atoms	868	752
RMS_{bonds}	0.002	0.014
RMS_{angles}	0.39	1.00
Ramachandran favored (%)	100	99
outliers (%)	0	0
clashscore	1.30	1.35
average B-factor	35.60	77.40

1. Values for the highest resolution shell are show in parentheses.

Six hydrophobic layers stack, exclude water, and form the core of the hexamer. The Phe residues within each layer are separated by ca. 3.8 Å and the Phe residues between layers are separated by ca. 4.1 ˚A. The faces of the Phe residues are oriented parallel to the central axis of the hexamer and do not appear to stack between the layers (Figure 2D). The faces of the Phe residues adopt a parallel orientation to avoid steric clashes with the side chains of the Ile residues at the d positions within each layer. The side chains of Ile residues fill the space between the side chains of the Phe residues within each layer. Six Leu residues near the N-terminus of peptide 1a cap the hydrophobic core, with three Leu residues packing above and below the hydrophobic core.

We designed the heptad repeat to take advantage of electrostatic interactions between the Lys and Glu residues at positions b and g within the heptad. In a parallel conformation these residues would form salt bridges, however in the antiparallel conformation the formation of salt bridges from positions b and g in peptides 1 would be impossible (Figure 3). The Lys residues at the b positions are displayed proximal to one another while Glu residues at the g positions are also displayed proximal to one another. The 6.5 Å offset that occurs between antiparallel α-helices allows for the separation of the Lys residues from each other, the separation of Glu residues from each other, and decreases the electrostatic repulsion between these similarly

charged residues. The lack of salt bridging between oppositely charged residues within the hexamer further emphasizes the importance of the hydrophobic core as a driving force for the formation and stabilization of the hexamer.

Figure 2: X-ray crystallographic structure of peptide 1a. (A) Hexamer, side view. (B) Hexamer, top view. (C) Hexamer, top view showing Phe and Ile residues inside the hy- drophobic core. (D) Hexamer, side view showing Phe and Ile residues lining the inside of the hydrophobic core.
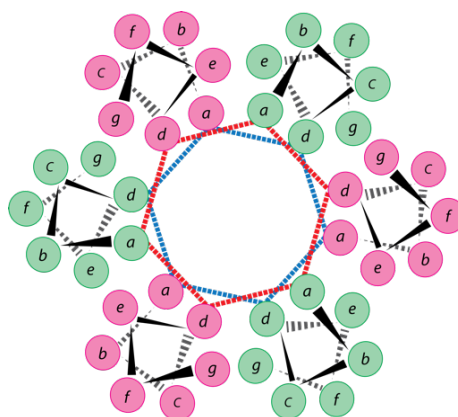
Figure 3: Diagram of the heptad repeat *a-b-c-d-e-f-g* arranged in an antiparallel α-helix conformation. Two axial layers in the *a-d-a-d-a-d* patterning of Phe and Ile residues at *a* and *d* positions are shown by the red and blue dashed lines.
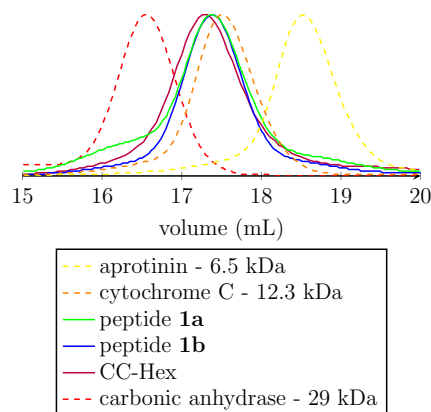
3.3.2 Size-Exclusion Chromatography of Peptides 1:
We studied the behavior of peptides 1 in solution by size-exclusion chromatography (SEC), small-angle X-ray scattering (SAXS), and circular dichroism (CD). The elution profile of peptides 1 were compared to the elution profiles of carbonic anhydrase, cytochrome C, and aprotinin. These 29, 12.3, and 6.5 kDa standards eluted at 16.6, 17.5, and 18.6 mL, respectively. At 1 mM, peptide 1a eluted at 17.4 mL, consistent with an oligomer in the tetramer to pentamer size range, slightly later than would be expected for the hexamer but much sooner than would be expected for the 3.4 kDa monomer (Figure 4). The elution profile shows a small secondary hump at 16.2 mL, consistent with an oligomer that has dimerized. Peptide 1b showed a similar elution

profile to that of peptide 1a but lacked the dimer peak at 16.2 mL. To address the difference between the expected and observed elutions values, we evaluated the behavior of CC-Hex under identical conditions. The CC-Hex oligomer eluted at 17.3 mL, also consistent with an oligomer in the tetramer to pentamer size range and also slightly later than would be expected for a hexamer. These results suggest that peptides 1 and CC-Hex behave similarly in solution and that the later- than-expected elution from the SEC column may be due to non-specific interactions of the peptides with the column or hexamers that are in a fast equilibrium with monomer or dimer subcomponents.

3.3.3 Small-Angle X-ray Scattering of Peptides 1:

The solution oligomerization state of peptides 1a was further resolved by solution small- angle X-ray scattering (SAXS).[56,57] SAXS profile data were collected for peptides 1 in three buffers: 0.1 M potassium formate, 0.1 M sodium formate, and 0.1 M HEPES and at peptide concentrations of 1 mM, 500 μM, and 250 μM. The scattering profiles of peptide 1a does not appear to vary noticeably between concentrations but did vary slightly between buffer conditions (Figure 5). The SAXS profiles of peptide 1a also exhibit large inflections at low q ranges regardless of concentration or conditions. This inflection is characteristic of the presence of large aggregates in solution.[58] Figure 5A shows the SAXS profiles of peptide 1a in potassium phosphate, sodium formate, and HEPES buffers and at a peptide concentration of 500 μM. The sharp increase in intensity in the Guinier region, low q values, indicates that peptide 1a forms large aggregates in solution (Figure 5B).

volume (mL)

- - - aprotinin - 6.5 kDa
- - - cytochrome C - 12.3 kDa
—— peptide **1a**
—— peptide **1b**
—— CC-Hex
- - - carbonic anhydrase - 29 kDa

Figure 4: SEC chromatograms showing the elution profiles of peptides 1, CC-Hex, and size standards carbonic anhydrase, cytochrome C, and aprotinin.

We analyzed the SAXS profiles using the program ScÅtter to determine the radius of gyration (R_g), the length of the maximum dimension (D_{max}), and the volume of the oligomers formed by peptide 1a. The SAXS profiles of peptide 1a showed the least amount of aggregation in sodium formate. Analysis of the Guinier region, just past the inflection caused by aggregates, shows that peptide 1a forms oligomers with a "reciprocal space" R_g of 20.95 Å. Analysis of the distribution plot, P(r), shows that peptide 1a has a "real space" R_g of 20.65 Å and a D_{max} of 74 Å. The P(r) distribution shows peaks at higher R_g values, indicating the presence of hexamers that have dimerized or formed larger oligomers. A comparison to the theoretical P(r) of the crystallographic hexamer of peptide 1a shows a good correlation to the SAXS profile of peptide

1a before the peaks caused by the larger aggregates (Figure 5C). A comparison of the calculated volumes derived from the SAXS profile and that of the crystallographic hexamer also show a good correlation (33,000 Å^3 vs 32,500 Å^3, respectively).
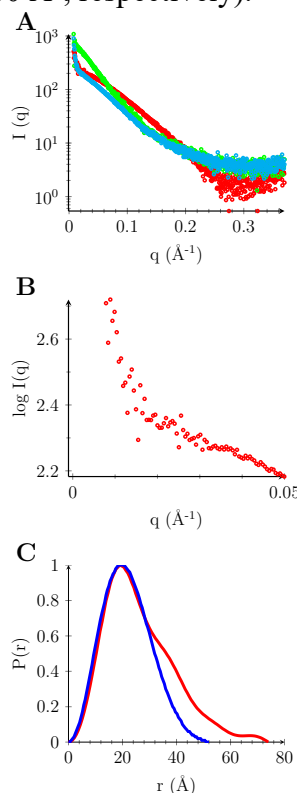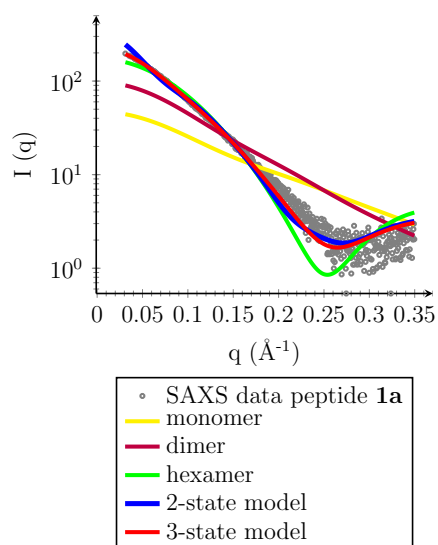

Figure 5: A) SAXS profiles for peptide 1a in 0.1 M potassium phosphate (green), 0.1 M sodium formate (red), and 0.1 M HEPES (cyan). B) Expansion of the lower q region of peptide 1a in 0.1 M sodium formate. C) Size distribution, P(r), plots of peptide 1a in sodium formate and the theoretical P(r) of the hexamer of peptide 1a.

We compared the theoretical scattering profiles derived from structures generated from the crystal lattice to the SAXS profile of peptide 1a using the program MultiFoXS.[59] As indicated by the P(r) analysis, peptide 1a is heterogenous in solution and a single structure does not completely explain the observed SAXS profile data. The theoretical scattering pro- files of the monomer, dimer, trimer, hexamer, dimers of hexamers, and trimers of hexamers were compared to the observed SAXS profile of peptide 1a (Figure 6). The scattering profile of the hexamer alone matched poorly to the profile of peptide 1a, with a χ^2 value of 4.04. A 2-component mixture of dimers and dimers of hexamers showed a better correlation with a χ^2 value of 3.12 and a 3-component mixture of dimers, hexamers, and dimers of hexamers showed the best correlation with a χ^2 value of 1.66. These data suggest that peptide 1a forms dimers, hexamers, and larger aggregates comprising hexamer units in solution.

3.3.4 Circular Dichroism of Peptides 1:
We studied the thermal stability of peptides 1 by monitoring temperature-dependent changes in the CD spectrum. At 20 °C, a 50 μM solution of peptide 1a displays a CD spectrum characteristic of an α-helix conformation, with maximums in mean residue ellipticity ($[\theta]_{MR}$) at

220 and 208 nm wavelength (Figure 7). Gradually warming the solution from 10-95 °C over two hours and monitoring the $[\theta]_{MR}$ at 222 nm showed a loss of ellipticity starting around 75 °C (Figure 7). A loss of ellipticity is commonly associated with a loss of tertiary or secondary structure as a peptide or protein denatures.[62] Peptide 1b shows a similar CD spectrum but with a loss of ellipticity beginning around 60 °C. The loss of $[\theta]_{MR}$ may be due to the aggregation of peptide 1. Peptide 1b aggregates to make visible insoluble precipitates at higher temperatures, resulting in a lower concentration of hexamer in solution. Peptide 1a did not form visible aggregates but may still form large soluble aggregates rather than denaturing at higher temperatures. Normalizing the CD spectra of peptide 1a to the $[\theta]_{MR}$ observed peak at 209 nm for each temperature measurements shows little difference in the secondary structure of peptide 1a at higher temperatures (Figure 8). Even at 90 °C, the CD spectrum suggests that peptide 1a adopts an α-helix but is present at a much lower concentration.

Figure 6: SAXS profile for peptide 1a in 0.1 M sodium formate and theoretical scattering profiles for the monomer, dimer, hexamer, 2-state model, and 3-state model of peptide 1a.
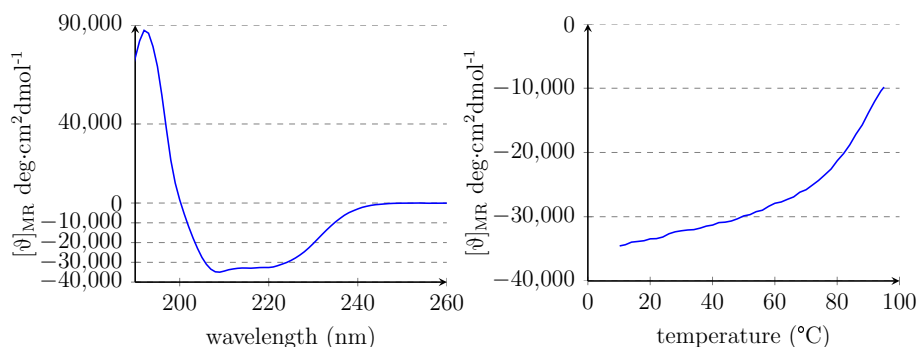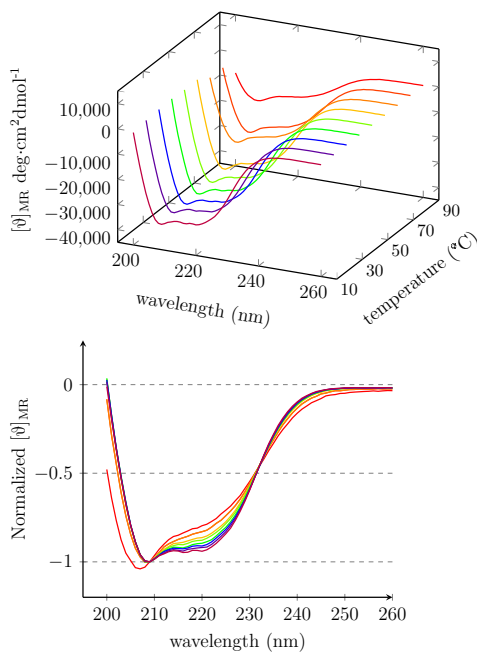

Figure 7: CD spectrum of a 50 μM solution of peptide 1a in 100 mM potassium phosphate buffer at pH 7.4 and at 20 °C (left). CD melting point curve of a 50 μM solution of peptide 1a in 100 mM potassium phosphate buffer at pH 7.4 recorded between 10-95 °C and at 222 nm wavelength (right).

3.4 DISCUSSION

The X-ray crystallographic structure of the antiparallel hexamers formed by peptides 1 represents a new protein fold not previously observed at atomic resolution for de novo peptides. Key to the assembly of the hexamer is the formation of a large hydrophobic core populated with Phe and Ile residues that pack tightly in the center of the hexamer while hydrophilic residues line the outer surface. The formation of this compact hydrophobic core creates a hexamer with a diameter of ca. 22 Å, slightly smaller than that of CC-Hex, and prevents the formation of a water accessible channel. Many de novo coiled-coils designs utilize Glu and Lys residues at opposing positions to promote salt bridging between helices, however, in peptides 1 the Glu and Lys residues are unable to form salt bridges because of the antiparallel conformation in ACC-Hex. This lack of additional stabilization from the exterior residues on ACC-Hex further emphasizes the substantial contribution of the hydrophobic residues within the core in its stabilization.

The hexamer core appears to form from the assembly of three dimer units. In each dimer, two α-helices assemble in an antiparallel arrangement with a ca. 6 Å offset. This offset permits the Phe residues at the a positions within each α-helix to interact among the edges of the aromatic groups, creating a zipperlike pattern (Figure 9A). The Ile residues at the d positions pack behind the Phe residues, locking the aromatic rings in a conformation parallel to the axis of the α-helix. This arrangement creates a large wedge in which two hydrophobic surfaces of the dimers are separated by ca. 120 degrees (Figure 9). Two additional dimers associate along the hydrophobic surfaces to form the complete hexamer.


Figure 8: CD spectra of a 5 μM solution of peptide 1a in 100 mM potassium phosphate buffer at pH 7.4 between 10-90 °C (top). Normalized CD spectra of a 50 μM solution of peptide 1a in 100 mM potassium phosphate buffer at pH 7.4 between 10-90 °C (bottom).

Peptides 1 were designed based on the heptad sequence that formed parallel hexamers and thus the formation of the antiparallel hexamer was unexpected. There is little difference in hydrophobicity between Leu and Phe residues but a substantial difference in the volumes of the two residues.[63] The smaller size of the Leu residues in the CC-Hex heptad sequence permits the

parallel arrangement of the α-helices and also allows for a small water-accessible channel in CC-Hex. The larger Phe residue however does not permit the parallel arrangement of α-helices and would likely cause significant steric clashing between symmetric residues in the a positions between parallel α-helices. The Phe-Ile residue combination at the a and d positions in peptides 1 permits the formation of the antiparallel dimer that further assembles to form ACC-Hex. Other de novo peptides containing either Phe or Trp residues at both the a and d positions within the heptad sequence form parallel pentamers or tetramers.[18,20] While the incorporation of aromatic residues has been shown to stabilize hexameric helical bundles in solution, the structure of these bundles and the contributions of the aromatic residues to their formation have not been characterized at atomic resolution.[38]

The formation of an antiparallel coiled-coil hexamer by peptides or proteins is rare. A search of the CC+ coiled-coil database reveals only three antiparallel coiled-coil hexamer motifs with minimal resemblance to the hexamer formed by peptides 1.[64,65] A 146 amino acid protein derived from *Thermoplasma acidophilum* forms an antiparallel hexamer through the association of three proteins along a three-fold rotational axis. Each protein monomer contributes two α-helices to form the antiparallel hexamer (PDB 1NIG).[66] Hydrophilic Lys, Arg, and Glu amino acids and hydrophobic Tyr and Lue residues occupy the center of the hexamer. A similar *a-d-a-d-a-d* pattern is observed between the Tyr and Leu residues that occupy a portion of the core. A 181 amino acid protein derived from *Lactobacillus reuteri* shows a similar topology to the protein derived from *T. acidophilum*, but contains additional hydrophilic residues that form a hydrophilic hexamer core (PDB 2NT8).[67] Finally, a 169 amino acid protein derived from *Sulfolobus tokodaii* displays similar characteristics to the two previous proteins with three monomer protein units forming an antiparallel hexamer (PDB 1WVT).[68] A single layer of Phe and Val residues in an a-d-a-d-a-d pattern is notice- able within the hexamer core but much like the two previous proteins, the hexamer core is dominated by hydrophilic residues.
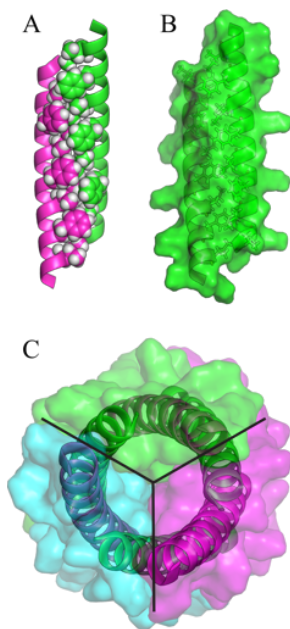
Figure 9: (A) Cartoon structure of the antiparallel dimer with Phe and Ile residues shown as spheres. (B) Surface diagram of the antiparallel dimer. (C) Surface diagram of the hexamer comprising three dimer surfaces.

While the antiparallel hexamer motif by these three proteins share similar topologies to the hexamer formed by peptide 1, the fundamental interactions between the α-helices in the protein-derived hexamers and that of peptides 1 are different. The α-helices that form the protein-derived hexamers are short in length (10-12 residues) and are constructed primarily from the interactions of hydrophilic residues. Peptides 1 contain only hydrophobic residues within the hexamer core and create a dry surface, devoid of water. The hexamers formed by the three proteins contain additional contacts between the side chains of distal residues not involved in the hexamer core structure, which may help stabilize the hexamers in the crystal lattice. Without the additional contacts, these natural protein domains may not form coiled- coil hexamers in the crystal lattice and are unlikely to form hexamers in solution. Peptides 1, on the other hand, form hexamers and higher-order assemblies of hexamers in both the crystal lattice and in solution.

3.5 CONCLUSIONS

Here, we report the X-ray crystallographic structure and solution behavior of an antiparallel coiled-coil hexamer formed by de novo peptides. The peptides fold to adopt an α-helix that further associate along hydrophobic residues to form the dry hydrophobic core of ACC- Hex. The staggered alignment of the α-helices allows for the interdigitation of the Ile and Phe residues within the core, leading to a compact antiparallel hexamer that is resistant to denaturation, even at high temperatures. Collectively, the SEC, SAXS, and CD data show that peptides 1 form hexamers in solution, which exist in equilibrium with dimers, hexamers, and larger aggregates of hexamers. The structure of ACC-Hex provides a new interaction motif for, and expands the range of molecular assembly accessible by de novo peptides. Further experiments will explore the chemical determinants of ACC-Hex stability based on this interaction motif, the supramolecular registration, and the kinetics of larger assemblies formed by peptides 1. The controlled and systematic incorporation of aromatic amino acids into coiled coils with solution behavior strongly correlated to their structure in the solid state provides a promising experimental platform in which to study electronic delocalization and long-range charge transport in peptides and proteins.

3.6 MATERIALS AND METHODS

Solvents used for peptides synthesis and RP-HPLC purification were purchased from VWR or Fisher Scientific and were used directly without further purification. Fmoc-amino acids, amino acid coupling reagent (HCTU), and Rink-amide AM resin were purchased from Chem- Impex International. Peptide synthesis was performed on a CEM Liberty Blue automated peptide synthesizer equipped with a microwave reactor.

Synthesis of peptides 1: Representative synthesis of peptide 1a. Loading of the resin. Rink-amide resin AM (400 mg, 0.52 mmol/g) was added to a Bio-Rad Poly-Prep chromatography column (10 mL). The resin was suspended in dry DMF (10 mL) and allowed to swell for 1 hr. The solution was drained from the resin and a solution of 20% piperidine in dry DMF was added to cleave the Fmoc- protecting group on the resin. After 30 minutes, the solution was drained from the resin and washed with dry DMF (5 × 5 mL). A solution of Fmoc-Lys(Boc)-OH (2.5 equiv., 252 mg, 0.52 mmol), HCTU (2.3 equiv, 0.48 mmol) in 20% NMM in dry DMF (5 mL) was added immediately and the mixture was gently agitated for 6 h. The solution was then drained and washed with DMF (3 × 5 mL) and then a mixture of acetic anhydride:pyridine (3:2, 5 mL) was added immediately. The mixture was gently agitated for 1 h to cap the unreacted

Rink-amide sites. The capping solution was drained and the resin was then washed with dry DMF (2 × 10 mL) and dried by passing nitrogen through the vessel.

Peptide coupling. The Rink-Lys(Boc)-Fmoc generated from the previous step was trans- ferred to a solid-phase peptide synthesizer reaction vessel and submitted to cycles of auto- mated peptide coupling with Fmoc-protected amino acid building blocks. The linear peptide was synthesized from the C-terminus to the N-terminus starting at Gln. Each coupling consisted of: i. Fmoc-deprotection with 20% piperidine in DMF for 3 min at 50 °C, ii. washing with DMF (3 × 7 mL), iii. coupling of the amino acid (0.83 mmol, 4 equiv.) in the presence of HCTU (0.83 mmol, 4 equiv.) and 20% NMM in DMF, and iv. washing with DMF (2 × 7 mL). Each amino acid coupling step took 10 min at 50 °C. After the last amino acid was coupled (Glu), the terminal Fmoc group was removed with 20% piperidine in DMF. The resin was transferred from the reaction vessel of the peptide synthesizer to a Bio-Rad Poly-Prep chromatography column.

Capping of the peptide. A 5 mL solution of acetic anhydride:pyridine (3:2) was added to the crude peptide and agitated for 1 hr. The solution was drained and washed with DMF (2 × 5 mL) and then CH_2Cl_2 (5 × 5 mL). The resin was dried by passing nitrogen through the vessel for 10 min.

Cleavage of the peptide from the resin and global deprotection. The linear peptide was cleaved from the resin by agitating the resin for 2 hr in a solution of TFA/triisopropylsilane (TIPS)/H_2O (18:1:1, 10 mL). The suspension was filtered and the filtrate was collected in a 250 mL round-bottomed flask. The resin was washed with an additional TFA/TIPS/H_2O mixture (5 mL). The combined filtrates were concentrated by rotary evaporation to about 5 mL and transferred to a 50 mL conical vial. The conical vial was placed on dry ice and cold Et_2O (45 mL) was added all at once. The peptide precipitated, was centrifuged, and the supernatant was removed. The crude peptide was washed with additional cold Et_2O (45 mL × 2). Residual Et_2O was removed by passing nitrogen over the conical vial yielding crude peptide 1a as an off-white solid (245 mg, 28% yield based on 100% loading of the resin). Peptide 1b was isolated in similar quantities.

Isolation of peptide 1a by RP-HPLC. Peptide 1a was purified in multiple 50 mg batches because peptide 1a forms a hydrogel at concentrations >10 mM. A single batch of crude peptide 1a was dissolved in a 1:1 mixture of H_2O and acetonitrile (5 mL) and the solution was filtered through a 0.20 μm syringe filter and purified by reversed-phase HPLC (gradient elution with 40–95% CH_3CN over 30 min). Pure fractions were combined and lyophilized. Peptide 1a was isolated as 35 mg of a white powder. Additional batches resulted in similar isolated quantities of peptide 1a. Peptide 1b was isolated in similar quantities.

Crystallization of peptide 1b: Crystallization procedures were performed similarly to those described previously.[44–46] Crystallization conditions were determined using the hanging-drop vapor-diffusion method. Crystallization was performed in a 96-well format, with each well containing 100 μL of a solution from a 96-well screening kit. Three kits were used (Hampton Index, PEG/Ion, and Crystal Screen) for a total of 864 experiments (three 96-well plates with three drops per well). Hanging drops were made by combining 75 nL aliquots of peptide 1b solution (10 mg/mL in 18 MW deionized water) and 75 nL aliquots of the well solution in 1:1, 2:1, and 1:2 ratios using a TTP LabTech Mosquito crystal screening robot. Crystals grew rapidly

(< 48 h) in multiple wells. A solution of 0.1 M sodium formate and 12% PEG 3350 was selected from the Index crystal screen kit for further optimization.

Crystallization conditions were optimized using a 4×6 matrix Hampton VDX 24-well plate. The PEG concentration was varied in increments of 2% across the rows and the pH of the sodium formate buffer was varied in increments of 0.5 pH units down the columns. Three hanging-drops were suspended on each borosilicate glass slide. The drops were prepared by combining 1- or 2-μL aliquots of a solution of peptide 1b (10 mg/mL) and the well solution in 1:1, 2:1, and 1:2 ratios. Slides were inverted and pressed firmly against the silicone grease surrounding each well. Crystals of peptide 1b suitable for X-ray crystallography were selected from 3 separate wells containing 0.1 M sodium formate with pH ranges 6.75-7.3 and 25-28% PEG 3350. Crystals of peptide 1a suitable for X-ray crystallography were selected from 0.1 M sodium formate with pH 7.3 and 28% PEG 3350.

Crystallization conditions for peptides 1 are shown in Table 1.

X-ray diffraction data collection, data processing, and structure determination for peptides 1: X-ray diffraction data sets for peptides 1 were collected at the Advanced Light Source (ALS) at the Lawrence Berkeley National Laboratory (Berkeley, California) on synchrotron beam- line 5.0.1 at 0.98 Å wavelength with 0.5° rotation per image (Table 1). Diffraction data were scaled using XDS,[47] analyzed using Pointless,[48] and merged using Aimless.[49]

Structure determination of peptide 1b: The electron density map of peptide 1b was determined by single-anomalous diffraction (SAD) phasing techniques. The locations of the anomalous signals from the iodines in the p- iodophenylalanines were determined using the program Hybrid Structure Search (HySS).[50,51] A weak anomalous signal was present to a resolution of 6.5 Å. The coordinates for the iodine sites were used directly in the program AutoSol,[52] in the Phenix software suite,[53] to generate an initial electron density map and model. Molecular manipulations of the model were performed with Coot.[54] Coordinates were refined with phenix.refine. Models were refined with riding hydrogen atoms. Table 1 shows the statistics of data collection and model refinement for peptide 1b.

Structure determination of peptide 1a: The electron density map of peptide 1a was determined by molecular replacements tech- niques. A single α-helix derived from peptide 1b was used as a search model in the program Phaser.[55] After determining the location of the inital alpha-helix, two additional helices were placed within the asymmetric unit. Models were manipulated and refined similarly to that of peptide 1b. Table 1 shows the statistics of data collection and model refinement for peptide 1a.

Size-exclusion chromatography of peptides 1: The oligomerization of peptides 1 was studied by size-exclusion chromatography (SEC) at 5 °C in 100 mM potassium phosphate buffer at pH 7.4. Peptides 1 were dissolved in potassium phosphate buffer to a concentration of 1 mM and loaded onto a GE Superdex 200 10/300 GL column at a flow rate 0.5 mL/min. Samples were eluted with potassium phosphate buffer at a flow rate of 0.5 mL/min. Chromatograms were recorded at 280 nm and normalized to the highest absorbance value. Peptides 1 eluted at 17.4 mL with peptide 1a showing an additional peak at 16.2 mL. Standards (carbonic anhydrase, cytochrome C, and aprotinin) were eluted similarly and are plotted along with peptides 1.

Small-angle X-ray scattering of peptides 1: Small-angle X-ray scattering (SAXS) profiles of peptides 1 were collected on SIBYLS beam- line (12.3.1) at the Advanced Light Source (ALS) at the Lawrence Berkeley National Lab- oratory (Berkeley, California). SAXS samples were prepares in a high-throughput 96-well format.[56,57] Peptides 1 were dissolved in 100 mM potassium phosphate, sodium formate, or HEPES buffer to a peptide concentrations of 1 mM, 500 μM, and 250 μM. Peptide solutions were centrifuged at 14,000 g for 10 min. Aliquots (100 μL) from the supernatant were transferred to a 96-well plate. Raw scattering profiles for peptides 1 and buffers were recorded at 0.5, 1, 2, and 4 second X-ray exposures. Scattering profiles of the buffer solutions were subtracted from the raw scattering profiles of peptides 1. SAXS profiles were analyzed using the programs ScÅtter and MultiFOXS.[58,59]

Circular dichroism of peptides 1: The conformation of peptides 1 were studied by circular dichroism (CD). Peptides 1 were dissolved in 100 mM postassium phophate buffer at pH 7.4 to a concentration of 50 μM or 5 μM. CD spectra were recorded on a Jasco J-810 Spectropolarimeter equipped with a Peltier thermoelectric temperature control device. The 50 μM samples of peptides 1 were prepared in a quartz cuvette with a 1 mm path length and the 5 μM sample of peptide 1b was prepared in a quartz cuvette with a 1 cm path length. The CD spectrum for the 50 μM solutions of peptides 1 were recorded between 190–260 nm wavelength and at 20 °C. CD melting point data for the 50 μM solution of peptide 1a was recorded by gradually warming from 10–95 °C at a rate of 40 degrees per hour and recording at 222 nm wavelength. The CD spectra for the 5 μM solution of peptide 1b was recorded between 10–90 °C by gradually warming the sample at a rate of 40 °C per hour and recording a CD spectra at every 10 degree increment.

3.7 REFERENCES

1. Brunette, T. J.; Parmeggiani, F.; Huang, P. S.; Bhabha, G.; Ekiert, D. C.; Tsutakawa, S. E.; Hura, G. L.; Tainer, J. A.; Baker, D. Exploring the repeat protein universe through computational protein design. Nature 2015, 528, 580–584.
2. Doyle, L.; Hallinan, J.; Bolduc, J.; Parmeggiani, F.; Baker, D.; Stoddard, B. L.; Bradley, P. Rational design of alpha-helical tandem repeat proteins with closed ar- chitectures. Nature 2015, 528, 585–588.
3. Huang, P. S.; Feldmeier, K.; Parmeggiani, F.; Fernandez Velasco, D. A.; Hocker, B.; Baker, D. De novo design of a four-fold symmetric TIM-barrel protein with atomic-level accuracy. Nat. Chem. Biol. 2016, 12, 29–34.
4. Crick, F. H. C. The packing of alpha-helices - simple coiled-coils. Acta Crystallographica 1953, 6, 689–697.
5. Lupas, A. N.; Gruber, M. The structure of alpha-helical coiled coils. Fibrous proteins: coiled-coils, collagen and elastomers 2005, 70, 37–78.
6. Parry, D. A.; Fraser, R. D.; Squire, J. M. Fifty years of coiled-coils and alpha-helical bundles: a close relationship between sequence and structure. J. Struct. Biol. 2008, 163, 258–269.
7. Apostolovic, B.; Danial, M.; Klok, H. A. Coiled coils: attractive protein folding motifs for the fabrication of self-assembled, responsive and bioactive materials. Chem. Soc. Rev. 2010, 39, 3541–3575.
8. Woolfson, D. N. Building fibrous biomaterials from alpha-helical and collagen-like coiled-coil peptides. Biopolymers 2010, 94, 118–127.
9. Woolfson, D. N.; Bartlett, G. J.; Bruning, M.; Thomson, A. R. New currency for old rope: from coiled-coil assemblies to alpha-helical barrels. Curr. Opin. Struct. Biol. 2012, 22, 432–441.
10. Egelman, E. H.; Xu, C.; DiMaio, F.; Magnotti, E.; Modlin, C.; Yu, X.; Wright, E.; Baker, D.; Conticello, V. P. Structural plasticity of helical nanotubes based on coiled- coil assemblies. Structure 2015, 23, 280–289.
11. Adamson, J. G.; Zhou, N. E.; Hodges, R. S. Structure, function and application of the coiled-coil protein folding motif. Curr. Opin. Biotechnol. 1993, 4, 428–437.
12. Ogihara, N. L.; Ghirlanda, G.; Bryson, J. W.; Gingery, M.; DeGrado, W. F.; Eisen- berg, D. Design of three-dimensional domain-swapped dimers and fibrous oligomers. Proc. Natl. Acad. Sci. U. S. A. 2001, 98, 1404–1409.
13. Straussman, R.; Ben-Ya'acov, A.; Woolfson, D. N.; Ravid, S. Kinking the coiled coil–negatively charged residues at the coiled-coil interface. J. Mol. Biol. 2007, 366, 1232– 1242.
14. Steinkruger, J. D.; Woolfson, D. N.; Gellman, S. H. Side-chain pairing preferences in the parallel coiled-coil dimer motif: insight on ion pairing between core and flanking sites. J. Am. Chem. Soc. 2010, 132, 7586–7588.
15. Schnarr, N. A.; Kennan, A. J. Strand orientation by steric matching: a designed antiparallel coiled-coil trimer. J. Am. Chem. Soc. 2004, 126, 14447–14451.
16. Fletcher, J. M.; Boyle, A. L.; Bruning, M.; Bartlett, G. J.; Vincent, T. L.; Zaccai, N. R.; Armstrong, C. T.; Bromley, E. H.; Booth, P. J.; Brady, R. L.; Thomson, A. R.; Woolf- son, D. N. A basis set of de novo coiled-coil peptide oligomers for rational protein design and synthetic biology. ACS Synth. Biol. 2012, 1, 240–250.

17. Stetefeld, J.; Jenny, M.; Schulthess, T.; Landwehr, R.; Engel, J.; Kammerer, R. A. Crystal structure of a naturally occurring parallel right-handed coiled coil tetramer. Nat. Struct. Biol. 2000, 7, 772–776.

18. Liu, J.; Deng, Y.; Zheng, Q.; Cheng, C. S.; Kallenbach, N. R.; Lu, M. A parallel coiled-coil tetramer with offset helices. Biochemistry 2006, 45, 15224–15231.

19. Sales, M.; Plecs, J. J.; Holton, J. M.; Alber, T. Structure of a designed, right-handed coiled-coil tetramer containing all biological amino acids. Protein Sci. 2007, 16, 2224– 2232.

20. Liu, J.; Yong, W.; Deng, Y.; Kallenbach, N. R.; Lu, M. Atomic structure of a tryptophan-zipper pentamer. Proc. Natl. Acad. Sci. U. S. A. 2004, 101, 16156–16161.

21. Slovic, A. M.; Lear, J. D.; DeGrado, W. F. De novo design of a pentameric coiled-coil: decoding the motif for tetramer versus pentamer formation in water-soluble phospho-lamban. J. Pept. Res. 2005, 65, 312–321.

22. Liu, J.; Zheng, Q.; Deng, Y.; Kallenbach, N. R.; Lu, M. Conformational transition between four and five-stranded phenylalanine zippers determined by a local packing interaction. J. Mol. Biol. 2006, 361, 168–179.

23. Zaccai, N. R.; Chi, B.; Thomson, A. R.; Boyle, A. L.; Bartlett, G. J.; Bruning, M.; Linden, N.; Sessions, R. B.; Booth, P. J.; Brady, R. L.; Woolfson, D. N. A de novo peptide hexamer with a mutable channel. Nat. Chem. Biol. 2011, 7, 935–941.

24. Liu, J.; Zheng, Q.; Deng, Y.; Cheng, C. S.; Kallenbach, N. R.; Lu, M. A seven-helix coiled coil. Proc. Natl. Acad. Sci. U. S. A. 2006, 103, 15457–15462.

25. Dong, H.; Paramonov, S. E.; Hartgerink, J. D. Self-assembly of alpha-helical coiled coil nanofibers. J. Am. Chem. Soc. 2008, 130, 13691–13695.

26. Burgess, N. C.; Sharp, T. H.; Thomas, F.; Wood, C. W.; Thomson, A. R.; Zaccai, N. R.; Brady, R. L.; Serpell, L. C.; Woolfson, D. N. Modular design of self-assembling peptide-based nanotubes. J. Am. Chem. Soc. 2015, 137, 10554–10562.

27. Burton, A. J.; Thomas, F.; Agnew, C.; Hudson, K. L.; Halford, S. E.; Brady, R. L.; Woolfson, D. N. Accessibility, reactivity, and selectivity of side chains within a channel of de novo peptide assembly. J. Am. Chem. Soc. 2013, 135, 12524–12527.

28. Joh, N. H.; Wang, T.; Bhate, M. P.; Acharya, R.; Wu, Y.; Grabe, M.; Hong, M.; Grig- oryan, G.; DeGrado, W. F. De novo design of a transmembrane Zn(2)(+)-transporting four-helix bundle. Science 2014, 346, 1520–1524.

29. Hadley, E. B.; Gellman, S. H. An antiparallel alpha-helical coiled-coil model system for rapid assessment of side-chain recognition at the hydrophobic interlace. Biopolymers 2007, 88, 586–586.

30. Hadley, E. B.; Testa, O. D.; Woolfson, D. N.; Gellman, S. H. Preferred side-chain constellations at antiparallel coiled-coil interfaces. P. Natl. Acad. Sci. U. S. A. 2008, 105, 530–535.

31. Grigoryan, G.; Keating, A. E. Structural specificity in coiled-coil interactions. Curr. Opin. Struct. Biol. 2008, 18, 477–483.

32. Grigoryan, G.; Degrado, W. F. Probing designability via a generalized model of helical bundle geometry. J. Mol. Biol. 2011, 405, 1079–1100.

33. Grigoryan, G.; Kim, Y. H.; Acharya, R.; Axelrod, K.; Jain, R. M.; Willis, L.; Drndic, M.; Kikkawa, J. M.; DeGrado, W. F. Computational design of virus-like protein assemblies on carbon nanotube surfaces. Science 2011, 332, 1071–1076.

34. Thomson, A. R.; Wood, C. W.; Burton, A. J.; Bartlett, G. J.; Sessions, R. B.; Brady, R. L.; Woolfson, D. N. Computational design of water-soluble alpha-helical barrels. Science 2014, 346, 485–488.

35. Wood, C. W.; Bruning, M.; Ibarra, A. A.; Bartlett, G. J.; Thomson, A. R.; Ses- sions, R. B.; Brady, R. L.; Woolfson, D. N. CCBuilder: an interactive web-based tool for building, designing and assessing coiled-coil protein assemblies. Bioinformatics 2014, 30, 3029–3035.

36. Nivon, L. G.; Bjelic, S.; King, C.; Baker, D. Automating human intuition for protein design. Proteins 2014, 82, 858–866.

37. Parmeggiani, F.; Huang, P. S.; Vorobiev, S.; Xiao, R.; Park, K.; Caprari, S.; Su, M.; Seetharaman, J.; Mao, L.; Janjua, H.; Montelione, G. T.; Hunt, J.; Baker, D. A general computational approach for repeat protein design. J. Mol. Biol. 2015, 427, 563–575.

38. Ghirlanda, G.; Lear, J. D.; Ogihara, N. L.; Eisenberg, D.; DeGrado, W. F. A hierarchic approach to the design of hexameric helical barrels. J. Mol. Biol. 2002, 319, 243–253.

39. Feliciano, G. T.; da Silva, A. J.; Reguera, G.; Artacho, E. Molecular and electronic structure of the peptide subunit of Geobacter sulfurreducens conductive pili from first principles. J Phys Chem A 2012, 116, 8023–8030.

40. Malvankar, N. S.; Vargas, M.; Nevin, K.; Tremblay, P. L.; Evans-Lutterodt, K.; Nykypanchuk, D.; Martz, E.; Tuominen, M. T.; Lovley, D. R. Structural basis for metallic-like conductivity in microbial nanowires. MBio 2015, 6, e00084.

41. Malvankar, N. S.; Vargas, M.; Nevin, K. P.; Franks, A. E.; Leang, C.; Kim, B. C.; Inoue, K.; Mester, T.; Covalla, S. F.; Johnson, J. P.; Rotello, V. M.; Tuominen, M. T.; Lovley, D. R. Tunable metallic-like conductivity in microbial nanowire networks. Nat Nanotechnol 2011, 6, 573–579.

42. Sepunaru, L.; Refaely-Abramson, S.; Lovrincic, R.; Gavrilov, Y.; Agrawal, P.; Levy, Y.; Kronik, L.; Pecht, I.; Sheves, M.; Cahen, D. Electronic transport via homopeptides: the role of side chains and secondary structure. J. Am. Chem. Soc. 2015, 137, 9617–9626.

43. Vargas, M.; Malvankar, N. S.; Tremblay, P. L.; Leang, C.; Smith, J. A.; Patel, P.; Snoeyenbos-West, O.; Nevin, K. P.; Lovley, D. R. Aromatic amino acids required for pili conductivity and long-range extracellular electron transport in Geobacter sulfurre- ducens. MBio 2013, 4, e00105–00113.

44. Spencer, R. K.; Li, H.; Nowick, J. S. X-ray crystallographic structures of trimers and higher-order oligomeric assemblies of a peptide derived from Abeta(17-36). J. Am. Chem. Soc. 2014, 136, 5595–5598.

45. Spencer, R. K.; Kreutzer, A. G.; Salveson, P. J.; Li, H.; Nowick, J. S. X-ray crystal-lographic structures of oligomers of peptides derived from beta-microglobulin. J. Am. Chem. Soc. 2015, 137, 6304–6311.

46. Spencer, R. K.; Nowick, J. S. A newcomer's guide to peptide crystallography. Isr. J. Chem. 2015, 55, 698–710.

47. Kabsch, W. Xds. Acta Crystallogr., Sect. D: Biol. Crystallogr. 2010, 66, 125–132.

48. Evans, P. R. An introduction to data reduction: space-group determination, scaling and intensity statistics. Acta Crystallogr., Sect. D: Biol. Crystallogr. 2011, 67, 282–292.

49. Evans, P. R.; Murshudov, G. N. How good are my data and what is the resolution? Acta Crystallogr., Sect. D: Biol. Crystallogr. 2013, 69, 1204–1214.

50. Grosse-Kunstleve, R. W.; Adams, P. D. Substructure search procedures for macromolecular structures. Acta Crystallographica Section D-Biological Crystallography 2003, 59, 1966–1973.

51. McCoy, A. J.; Storoni, L. C.; Read, R. J. Simple algorithm for a maximum-likelihood SAD function. Acta Crystallogr D Biol Crystallogr 2004, 60, 1220–1228.

52. Terwilliger, T. C.; Adams, P. D.; Read, R. J.; McCoy, A. J.; Moriarty, N. W.; Grosse-Kunstleve, R. W.; Afonine, P. V.; Zwart, P. H.; Hung, L. W. Decision-making in structure solution using Bayesian estimates of map quality: the PHENIX AutoSol wizard. Acta Crystallogr D Biol Crystallogr 2009, 65, 582–601.

53. Adams, P. D.; Afonine, P. V.; Bunkoczi, G.; Chen, V. B.; Davis, I. W.; Echols, N.; Headd, J. J.; Hung, L. W.; Kapral, G. J.; Grosse-Kunstleve, R. W.; McCoy, A. J.; Moriarty, N. W.; Oeffner, R.; Read, R. J.; Richardson, D. C.; Richardson, J. S.; Terwilliger, T. C.; Zwart, P. H. PHENIX: a comprehensive Python-based system for macro- molecular structure solution. Acta Crystallogr., Sect. D: Biol. Crystallogr. 2010, 66, 213–221.

54. Emsley, P.; Lohkamp, B.; Scott, W. G.; Cowtan, K. Features and development of Coot. Acta Crystallogr., Sect. D: Biol. Crystallogr. 2010, 66, 486–501.

55. McCoy, A. J.; Grosse-Kunstleve, R. W.; Adams, P. D.; Winn, M. D.; Storoni, L. C.; Read, R. J. Phaser crystallographic software. J. Appl. Crystallogr. 2007, 40, 658–674.

56. Dyer, K. N.; Hammel, M.; Rambo, R. P.; Tsutakawa, S. E.; Rodic, I.; Classen, S.; Tainer, J. A.; Hura, G. L. High-throughput SAXS for the characterization of biomolecules in solution: a practical approach. Methods Mol. Biol. 2014, 1091, 245–258.

57. Classen, S.; Hura, G. L.; Holton, J. M.; Rambo, R. P.; Rodic, I.; McGuire, P. J.; Dyer, K.; Hammel, M.; Meigs, G.; Frankel, K. A.; Tainer, J. A. Implementation and performance of SIBYLS: a dual endstation small-angle X-ray scattering and macro- molecular crystallography beamline at the Advanced Light Source. J. Appl. Crystallogr. 2013, 46, 1–13.

58. Putnam, C. D.; Hammel, M.; Hura, G. L.; Tainer, J. A. X-ray solution scattering (SAXS) combined with crystallography and computation: defining accurate macro- molecular structures, conformations and assemblies in solution. Q. Rev. Biophys. 2007, 40, 191–285.

59. Schneidman-Duhovny, D.; Hammel, M.; Tainer, J. A.; Sali, A. Accurate SAXS profile computation and its assessment by contrast variation experiments. Biophys. J. 2013, 105, 962–974.

60. Powell, A.; Leslie, H. Processing diffraction data with Mosflm. Evolving Methods for Macromolecular Crystallography 2007, 245, 41–51.

61. Walshaw, J.; Woolfson, D. N. Socket: a program for identifying and analysing coiled-coil motifs within protein structures. J. Mol. Biol. 2001, 307, 1427–1450.

62. Kelly, S. M.; Jess, T. J.; Price, N. C. How to study proteins by circular dichroism. Biochim. Biophys. Acta, Proteins Proteomics 2005, 1751, 119–139.

63. Hackel, M.; Hinz, H. J.; Hedwig, G. R. Partial molar volumes of proteins: amino acid side-chain contributions derived from the partial molar volumes of some tripeptides over the temperature range 10-90 degrees C. Biophys Chem 1999, 82, 35–50.

64. Testa, O. D.; Moutevelis, E.; Woolfson, D. N. CC+: a relational database of coiled-coil structures. Nucleic Acids Res. 2009, 37, D315–322.

65. Moutevelis, E.; Woolfson, D. N. A periodic table of coiled-coil protein structures. J. Mol. Biol. 2009, 385, 726–732.

66. Sanishvili, R.; Pennycooke, M.; Gu, J.; Xu, X.; Joachimiak, A.; Edwards, A. M.; Chris-tendat, D. Crystal structure of the hypothetical protein TA1238 from Thermoplasma acidophilum: a new type of helical super-bundle. J. Struct. Funct. Genomics 2004, 5, 231–240.

67. St Maurice, M.; Mera, P. E.; Taranto, M. P.; Sesma, F.; Escalante-Semerena, J. C.; Rayment, I. Structural characterization of the active site of the PduO-type ATP:Co(I)rrinoid adenosyltransferase from Lactobacillus reuteri. J. Biol. Chem. 2007, 282, 2596–2605.

68. Tanaka, Y.; Sasaki, T.; Kumagai, I.; Yasutake, Y.; Yao, M.; Tanaka, I.; Tsumoto, K. Molecular properties of two proteins homologous to PduO-type ATP:cob(I)alamin adenosyltransferase from Sulfolobus tokodaii. Proteins 2007, 68, 446–457.

CHAPTER 4:

Sequence Mutability and Tunable Stability of Phe-Ile Zipper Coiled-Coil Hexamers

4.1 SUMMARY

Coiled coils are a robust motif for exploring amino acid interactions, generating unique supramolecular structures, and expanding properties of biological based materials. A recently discovered antiparallel coiled-coil hexamer (ACC-Hex, peptide 1) exhibits a unique interaction in which Phe and Ile residues from adjacent α-helices interact to form a Phe-Ile zipper within the hydrophobic core. Analysis of the X-ray crystallographic structure of ACC-Hex suggests that the stability of the six-helix bun- dle relies on specific interactions between the Phe and Ile residues. The Phe-Ile zipper is unprecedented and represents a powerful tool for utilizing the Phe-Ile interactions to direct supramolecular assembly. To further probe and understand the limits of the Phe-Ile zipper, we designed peptide sequences with natural and unnatural amino acids placed at the Phe and Ile residue positions. Using size exclusion chromatography and small angle X-ray scattering, we found that the proper assembly of ACC-Hex from monomers is sensitive to subtle changes in side chain steric bulk and hydrophobicity introduced by mutations at the Phe and Ile residues positions. Of the sequence vari- ants that formed ACC-Hex, mutations in the hydrophobic core significantly affected the stability of the hexamer, from $\Delta G_u^W = 2$ to 8 kcal·mol^{-1}. Additional sequences were designed to further probe and enhance the stability of the ACC-Hex system by maximizing salt bridging between the solvent exposed residues. Finally, we expanded on the generality of the Phe-Ile zipper, creating a unique sequence that forms an antiparallel hexamer that is topologically similar to ACC-Hex but atomistically unique.

4.2 INTRODUCTION

Coiled coils are one of the most well studied classes of supramolecular structures and have served as useful tools for improving our understanding of the folding, assembly, and in- teractions of proteins.[1–7] Coiled coils involve the interaction of two or more α-helices to form defined oligomeric assemblies.[8] This assembly motif is observed across a wide range of natural structures, from DNA binding proteins to ion channels and protein-protein inter actions.[1,2,9–11] Combining the coiled-coil assembly motifs observed in natural proteins with computational design and structural simulations has led to an expansion of *de novo* coiled- coil peptides with diverse supramolecular properties including fiber formation, catalysis, drug delivery, tissue growth scaffolds, and enormous assemblies that rival the complexity and size of those formed by viral capsids.[12–17]

α-Helices, the coiled-coil monomer units, form regular structures where the side chains of constituent amino acid residues are displayed at regular intervals around the core of the helix. The side chain positions are repeated every seven residues, forming discrete ridges of repeating residues along the axis of the helix. In coiled-coil peptides, a seven residue pattern, with positions in the heptad described by positions *abcdefg*, is often repeated multiple times along the length of the helix. The residues at the a and d positions, or any i and i + 3 positions, are aligned along the same ridge of the helix. When aliphatic residues, such as Leu, are placed at the a or d positions, the helices assemble to form dimers or higher-ordered oligomers along this hydrophobic ridge.[18–20] The side chains of the Leu residues interdigitate along the helix ridge, creating a zipper-like motif, aptly called a 'leucine zipper', which helps stabilize the oligomer.[1,2]

The Leu zipper motif has proved useful for the design of *de novo* sequences that form dimers,[21–24] trimers,[7,25] tetramers,[26–28] pentamers,[29] hexamers,[30] and larger assemblies.[31]

The aliphatic zipper motif has served as a robust interaction interface to drive assembly of diverse coiled-coil oligomers, including parallel hexamers, representing a unique protein fold not found in nature (Fig 1A).[30] Aliphatic side chains are used in the vast majority of *de novo* hydrophobic zipper seams, and few coiled-coil designs have incorporated aromatic residues within the hydrophobic core of the coiled coils. In one such example, when phenylalanine residues are placed at the a and d positions of the heptad repeats, parallel pentamers and tetramers form (Fig 1B).[32] The phenylalanine residues cluster and form the hydrophobic seams of the oligomers, creating a "phenylalanine zipper" within the pentamers. We recently developed a *de novo* peptide sequence that alternates Phe residues at the a positions and aliphatic Ile at the d positions. Instead of forming parallel oligomers, this Phe-Ile com- bination assembles into an antiparallel coiled-coil hexamer (ACC-Hex), an unprecedented structure in natural proteins and one not predicted by peptide design algorithms (Fig 1C).[33] In contrast to the previous designs with all aliphatic or all aromatic residues at a and d positions, this Phe-Ile interface creates a pore-free, hydrophobic core with tightly interlocking bulky aromatic groups and aliphatic side chains.
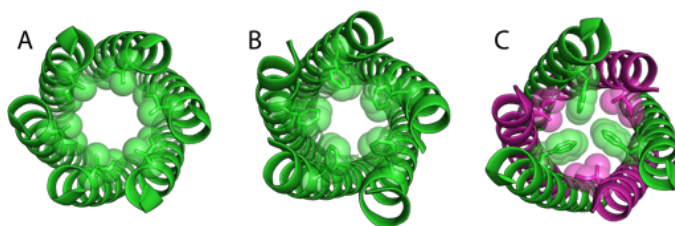
Figure 1: (A) Axial views of a coiled-coiled hexamer with Ile/Leu residues in the core (PDB 3R3K), (B) A coiled-coiled pentamer with Phe residues in the core (PDB 2GUV), (C) and an antiparallel coiled-coiled hexamer with Phe and Ile residues in the core (C, PDB 5EOJ). The first layer of hydrophobic residues are shown as sticks and spheres.

The X-ray crystallographic structure of ACC-Hex suggests it is assembled from three symmetric dimers. In each dimer, the monomers are oriented antiparallel to each other, with the C-terminus and N-terminus offset by 5 Å at each end. The offset of the α-helices permits the Phe residues at the a positions within the heptad sequence of one monomer to interact with Ile residues at the d positions of the adjacent monomer. This creates a zipperlike pattern of Phe and Ile residues along the intra-dimer interface (Figure 2). The hydrophobic cores of the parallel hexamers and parallel pentamers, constructed from aliphatic side chains or aromatic side chains, contain a small central pore that extends along the length of the oligomers.[30,32] The Phe-Ile zipper formed in the core of ACC-Hex however, creates a much more dense core and is devoid of a central pore (Fig 1). The exclusion of water and the formation of this dense hydrophobic core in ACC-Hex may be the driving force for the formation of ACC-Hex. These unique structural aspects of the ACC-Hex warrant further study, as do the interactions leading to their formation. In this work, we expand the set of natural and unnatural amino acids that drive assembly of ACC-Hex oligomers. Mutations of the a and d positions, as well as rearrangement of salt-bridging charged residues on the solvent exposed surface, provide insights into the side chain chemistry that determines ACC-Hex stability and assembly.

Ac-ELKAIAQE**F**KAIAKE**F**KAIAF$^\text{I}$EFKAIAQK-NH$_2$
abcdefgabcdefgabcdefgabcdefg
peptide **1**
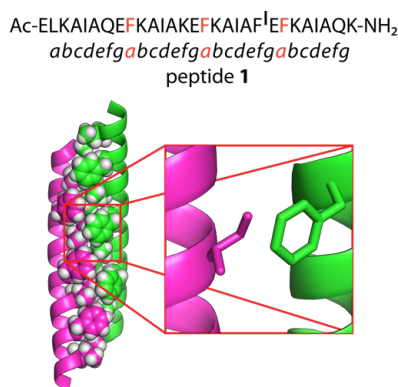
Figure 2: Amino acid sequence of peptide 1 and the X-ray structure showing the Phe-Ile zipper present in the antiparallel dimer formed by peptide 1.

4.3 RESULTS AND DISCUSSION

4.3.1 Impact of core residues on formation and stability of ACC-Hex:

From analysis of the X-ray structure of ACC-Hex, we focused our investigation of the stability of the six-helix bundle on the interactions between the Phe and Ile residues within the hydrophobic core. We synthesized variants in which the Phe residues at the a positions were mutated to Tyr, 4-methyl phenylalanine (Tol), or cyclohexyl alanine (Cha, peptides 2a–c, Table 1). In addition, we synthesized sequences in which the Ile residue at the d positions were changed to Val, Leu, or norleucine (Nle, peptides 3a–c, Table 1). The ACC- hex sequence was amenable to a majority of the mutations, with only peptides 2a and 3a not forming hexamers. We used a combinations of size exclusion chromatography (SEC) and SEC coupled small-angle X-ray scattering (SEC-SAXS) to study the oligomerization states of peptides 1-3. The differences in the stability of the oligomers formed by peptides 1-3 were studied by chemical denaturant titrations and monitored with circular dichroism (CD).

Table 1: Peptides **1** – **3**.

peptide	*a*	*d*	oligomeric state
1	Phe	Ile	hexamer
2a	Tyr	Ile	dimer
2b	Tol	Ile	hexamer
2c	Cha	Ile	hexamer
3a	Phe	Val	trimer
3b	Phe	Leu	hexamer
3c	Phe	Nle	hexamer

4.3.2 Oligomerization of peptides 1-3:

We designed peptides 2–3 to understand the structural relationship between the residues within the hydrophobic core and their impact on hexamer formation. Most of the peptides we designed formed hexamers and, in some instances, promoted hexamer formation. We used SEC as a preliminary measure of the oligomerization of peptides 1-3. Oligomeric states were determined by comparing elution profiles of peptides 2–3 to that of peptide 1 and molecular weight standards. Peptides 2b, 2c, 3b, and 3c eluted in similar volumes to that of peptide 1 (Figure 3). Peptides 2a and 3a precipitated in the buffer conditions; SEC of the supernatant showed much weaker signal and an indication of smaller oligomers, such as dimers or trimers. Peptide 2c exhibited a major peak at the peptide 1 hexamer elution volume, and a sizeable peak at an earlier

62

elution volume, consistent with the formation of a larger aggregate, such as a dimer of hexamers. There was no significant difference in the elution volumes of peptides that eluted near peptide 1.
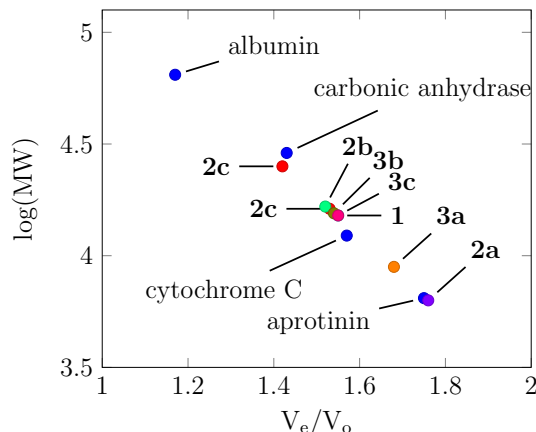

Figure 3: SEC results of peptides 1–3 and albumin, carbonic anhydrase, cytochrome C, albumin.

SEC-SAXS scattering profiles of the oligomers formed by peptides 1-3 confirmed their hexameric state in solution. We analyzed the scattering profile of peptide 1 using the pro- grams ATSAS and FoXS.[40,42,43] The analysis of the Guinier region of the scattering plot revealed a reciprocal Rg value of 17.99 Å and analysis of the Porod region revealed a real space Rg of 16.82 Å for peptide 1. Comparing the theoretical form factors of the crystallo- graphic monomer, dimer, and hexamer to that of the scattering profile of peptide 1 showed a poor correlation (χ 3.06, χ 1.90, χ 1.79, respectively, Figure 4). A composite of the con- tributions of the dimer and hexamer correlates better with the scattering profile of peptide 1 (χ 1.62, Figure 4), consistent with previous SAXS-only scattering data.[33] The scattering profiles of Leu and Nle mutations, peptides 3b and 3c, are similar to that of peptide 1, differing only in the linear contributions of the scattering profiles of dimer and hexamer components (Table 3).

Table 3: SAXS Results for Peptides **1** – **3**.

| peptide	Rg (reci) Å	Rg (real) Å	D_{max} Å	fit model	FoXS (χ)	ratio
1	17.99	16.82	44.98	hexamer + dimer	1.62	55 : 45
2a	–	–	–	–	–	–
2b	17.22	17.75	55.55	hexamer	1.04	100 : 0
2c	16.24	17.25	54.74	hexamer	1.21	100 : 0
3a	–	–	–	–	–	–
3b	18.94	18.44	53.09	hexamer + dimer	1.49	75 : 25
3c	19.96	23.92	95.01	hexamer + dimer	1.20	67 : 33

The scattering profiles of the Tol and Cha mutations at the a positions, peptides 2b and 2c, on the other hand, differ significantly from that of peptide 1 and correlate well with the theoretical scattering profile of the hexamer only (χ 1.04, χ 1.21, respectively). Figure 4 shows the scattering profile of peptide 2c and the theoretical scattering of the hexamer. The difference between the scattering profiles of peptides 2b and 2c and that of peptide 1, 3b, and 3b suggests that the equilibrium between dimer and hexamer is shifted further toward the hexamer for peptides 2b and 2c.
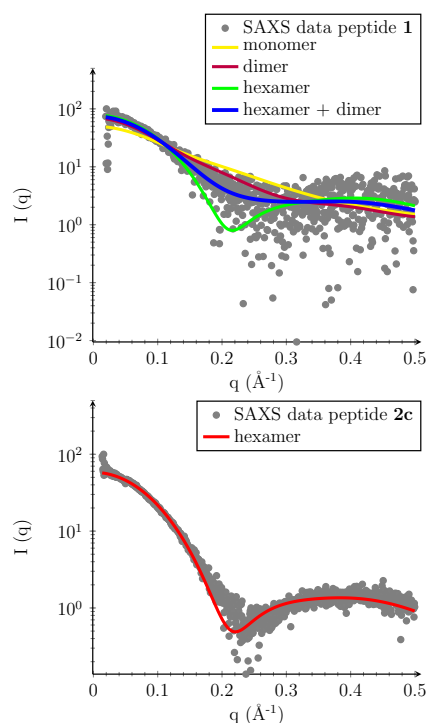
Figure 4: SEC-SAXS profile of peptide 1 eluted in 0.1 M potassium phosphate and theoretical scattering profiles for the monomer, dimer, hexamer, and dimer + hexamer of peptide 1. SEC-SAXS profile of peptide 2c eluted in 0.1 M potassium phosphate and the theoretical scattering profile of a hexamer.

4.3.3 The effects of a and d site mutations on the stability of peptides 1–3:

The SEC and SAXS results show that peptides 2b, 2c, 3b, and 3c form similar oligomers to that of peptide 1. CD spectroscopy of these peptides during chemical denaturation helped further characterize the impact of core substitution on the stability of the hexamers. At room temperature and in phosphate buffer, peptides 1, 2b, 2c, 3b, and 3c showed CD signatures consistent with an α-helix. Peptides 2a and 3a formed insoluble aggregates and stability measurements could not be performed. The remaining peptides were titrated with guanidinium chloride (Gdm-Cl) from 0-8 M while monitoring ellipticity at 222 nm to determine the free energies of unfolding in water (ΔG_u^w, Figure 5). The free energy values were determined by fitting the CD denaturation curves to either a 2-state model involving a native (N) and unfolded state (U) in equilibrium or 3-state model involving an intermediate state (I).[41,44] Free energies and m-values for peptides 1, 2b, 2c, 3b, and 3c are shown in Table 4.
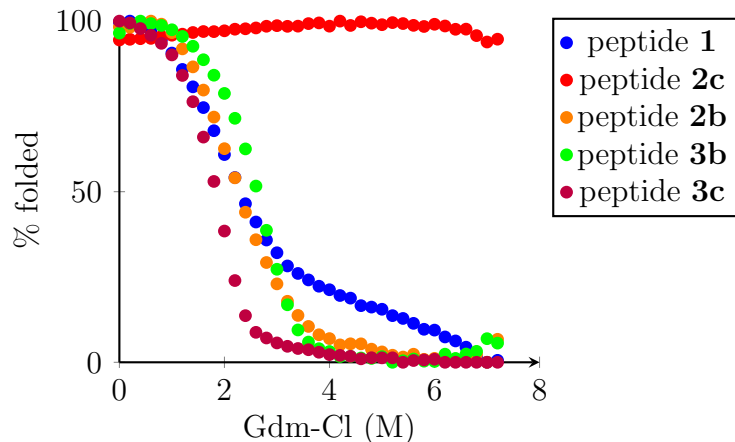
Figure 5: CD titration results of peptide 1, 2b, 2c, 3b, and 3c in 100 mM potassium phosphate titrated with guanidinum chloride (Gdm-Cl) 0-8 M. CD measurements were recorded at 222 nm wavelength and at a temperature of 20 °C.

Table 4: Gdm-Cl Titration Results for Peptides **1** − **3**.

peptide	fit model	ΔG_u^w kcal•mol^{-1}	m kcal•mol^{-1}•M^{-1}	$m_{N \to I}$ kcal•mol^{-1}•M^{-1}
1	3-state	2.65 ± 0.36	1.31 ± 0.14	1.17 ± 0.12
2a	–	–	–	–
2b	2-state	2.00 ± 0.13	1.00 ± 0.03	–
2c	2-state	7.86 ± 0.40	1.29 ± 0.07	–
3a	–	–	–	–
3b	3-state	4.08 ± 0.22	1.54 ± 0.05	2.89 ± 0.08
3c	3-state	3.86 ± 0.20	2.03 ± 0.11	2.01 ± 0.27

Combined with SEC and SEC-SAXS data, CD of the Gdm-Cl titrations provides insights into the stability determinants of the a and d positions. Substituting Phe at the a positions with Tyr prevented hexamer formation and promoted aggregation. The para-hydroxy substituent of the Tyr residue appears to prevent formation of the compact hydrophobic core, leading to the observed aggregation. The core may not form either because of the additional steric bulk of the para-hydroxy substituent or because of the introduction of a hydrophilic substituent. To test whether the steric bulk or increased hydrophilicity was preventing hexamer formation, we designed peptide 2b in which we replaced the Tyr residues with Tol residues. The 4-methyl substituent of Tol is comparable in size to that of the hydroxyl substituent on Tyr but is hydrophobic instead of hydrophilic. The extra steric bulk introduced by the Tol residue did not appear to disrupt the formation of the hydrophobic core and permitted hexamer formation. The increased hydrophobicity of the 4-methyl substituent at the a position (Δclog$_p$ 0.50) may shift the equilibrium of hexamer formation toward the hexamer, as observed in the SEC-SAXS data of peptide 2b, but its increased size relative to Phe may also reduce the stability of the hexamer by disrupting the tight packing of the core, as indicated by the lower ΔG_u^w value. These data suggest, therefore, that the relative hydrophilicity of the Tyr hydroxyl inhibits hexamer

assembly, possibly by impeding the elimination of water from the hydrophobic core during hexamer formation.

In the case of peptide 2c, Cha replaces Phe at the a positions, increasing hydrophobicity (Δclog$_p$ 1.23) and introducing a non-planar residue with additional steric bulk into the hydrophobic core. The increased steric bulk of Cha did not have the same slightly destabilizing effect as the Tol mutation. Rather, the introduction of the Cha residues in peptide 2c not only shifted the equilibrium toward hexamer formation, as observed in SEC-SAXS, but also created a hexamer that is incredibly stable to chemical denaturation (ΔG_u^w 7.86 kcal·mol^{-1}). [45]

Hexamer formation and stability was similarly sensitive to mutations at the d positions. Reducing the size and hydrophobicity at the d positions from Ile residues to Val residues (peptide 3a, Δclog$_p$ -0.53), amounting to a removal of a single methylene group from the Ile side chain, resulted in uncontrolled aggregation, similar to that of peptide 2a. These results indicate that the assembly of the hydrophobic core, via somewhat specific hydrophobic interactions, is crucial to the formation and stabilization of ACC-Hex. An increase in hydrophilicity or decrease in hydrophobicity of the residues within the hydrophobic core results in aggregation. The difference in hydrophobicity between Phe and Tyr is similar to the difference in hydrophobicity between Ile and Val (Δclog$_p$ -0.67 vs. Δclog$_p$ -0.53, respectively). These small changes in hydrophobicity are enough to disrupt hexamer formation. The X-ray structure of peptide 1 shows that the terminal methyl of the Ile residue forms van der Waal contacts with Phe residues in the dimer. The lack of these VDW contacts between Val and Phe residues is apparently sufficient to destabilize the dimer and resulting hexamer, inducing aggregation.

Other changes to the d positions were more subtle in their impact on hexamer stability. Mutating the Ile to Leu or Nle resulted in proper hexamer assembly and increased stability of the resulting hexamers to Gdm-Cl denaturant (4.08 and 3.86 vs 2.65 kcal·mol^{-1}, respectively). The Ile, Leu, and Nle residues are constitutional isomers with similar hydrophobicities. The differences in structure between the Ile, Leu, and Nle allow for different contacts between the side chains and the adjacent Phe residues. The side chains of both Leu and Nle are longer than the side chain of Ile, allowing the side chains of Leu and Nle to make additional contacts with the Phe residues, which may determine the improved stability of the hydrophobic core.

The d position mutations of peptides 3b and 3c had moderate effects on the ΔG_u^w values of the resulting hexamers. However, the CD titration curves of these peptides are best fit by a 3-state, rather than 2-state model, suggesting the presence of folded intermediate states in the denaturation mechanism. The m-values derived from the Gdm-Cl titrations of proteins have been shown to correlate with the change in accessible solvent area (ΔASA) between folded and unfolded states.[46,47] Figure 6 illustrates a few of the possible transitions that ACC-Hex may undergo as it denatures, going from hexamer to dimer to monomer to unfolded monomer. Calculated m-values based on ΔASA of the transitions are shown in Table 5. The $m_{N \to I}$, the m-value for the native to folded intermediate state transition, for peptide 1 is small, indicating that only a small change in ASA occurs between ACC-Hex and an intermediate stated distinguishable in CD. Previous SAXS data shows that ACC- Hex exists in fast equilibrium with dimers in solution even in the absence of denaturant.[33] The $m_{N \to I}$ value for peptide 1, therefore, is consistent with a transition from these dimers to folded monomers, and the global m-value corresponds to the transition from folded to unfolded monomer. For peptides 3b and 3c the $m_{N \to I}$ values are much larger, indicating a greater ΔASA transition. The ΔASA corresponding to the $m_{N \to I}$ value of peptide 3b suggests a hexamer to monomer transition as the first step in

denaturation, while peptide 3c may undergo a hexamer to dimer transition (2.89 vs 2.01 kcal·mol^{-1}). The second transition for peptide 3b would then involve the monomer to unfolded monomer transition while the second transition for peptide 3c undergoes a dimer to unfolded monomer transition (1.54 vs 2.03 kcal·mol^{-1}). These differences in the denaturation further delineate the structural differences between the Ile, Leu and Nle residues and the impact on the hydrophobic core of ACC-Hex. Assuming the denaturation steps are reversible, these results also suggest subtle differences in assembly mechanisms for the different ACC-Hex mutants.
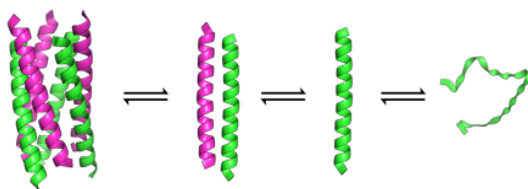
Figure 6: Possible transitions that ACC-Hex may undergo while denaturing; from hexamer to dimer to monomer to unfolded monomer.

Table 5: Calculated Changes in Accessible Solvent Area (ΔASA) and m-values.

transition	ΔASA (Å^2)	m_{calc} kcal•mol^{-1}•M^{-1}
hexamer to unfolded monomer	18,213	5.14
hexamer to monomer	9,495	3.13
hexamer to dimers	4,530	1.99
dimer to unfolded monomer	4,561	2.02
dimer to monomer	1,655	1.33
monomer to unfolded monomer	1,453	1.29

4.3.4 The impact of solvent exposed residues on ACC-Hex stability:

When first characterized, a surprising feature of the ACC-Hex structure was the arrangement of the charged residues that line the hydrophilic surface. Peptide 1 was designed as a variant of a parallel hexamer in which the solvent exposed residues participate in salt bridging to stabilize the structure. Instead, the antiparallel structure of ACC-Hex places similarly charged Lys residues near one another and Glu residues near one another. This arrangement creates a surface with stripes of large positive and negative charge density running along the central axis of the hexamer (Figure 7A). The unfavorable arrangement of these similarly charged residues is expected to destabilize the hexamer due to electrostatic repulsion and inhibit hexamer formation. To test whether the charged residues along the surface of peptide 1 contribute to destabilizing ACC-Hex, we designed peptide 4 which is identical to peptide 1 but each Glu and Lys position have been swapped. Combining peptide 1 and peptide 4 in a 1:1 mixture resulted in an increased

stability of the hexamer to Gdm-Cl denaturation (Figure 8). The crystal structure of a mixture of the two peptides is composed of hetero oligomers formed by peptides 1 and 4, and shows salt bridging between the oppositely charged Lys and Glu residues that line the solvent exposed surface (Figure 7B). The salt bridges formed between peptides 1 and 4 monomers are the likely driving force for hetero oligomer formation, and they may be responsible for the increase in observed solution stability of the hetero oligomer in the presence of Gdm-Cl.
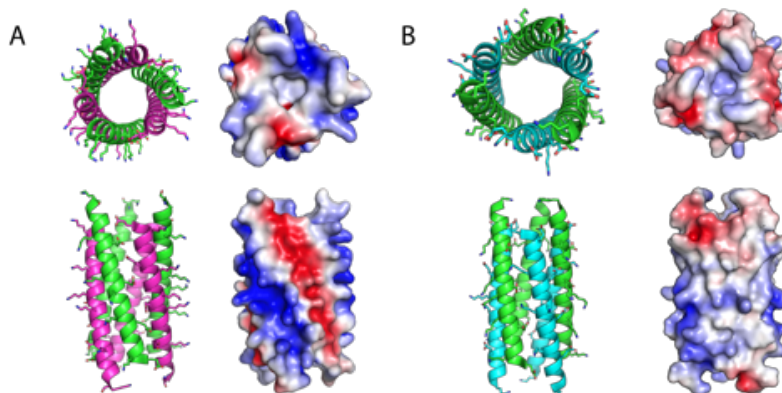
Figure 7: (A) Crystal structure and electrostatic surface of the hexamer formed by peptide 1. (B) Crystal structure and electrostatic surface of the hetero hexamer formed by peptides 1 and 4.

In the solid state, the hetero oligomer formed by peptides 1 and 4 appear to assemble in a 1:1 ratio (Figure 7B). Each dimer within the hexamer contains a single α-helix of peptide 1 and single α-helix of peptide 4. The hydrophobic surface of the hetero dimer is identical to the hydrophobic surface of the dimer formed by peptide 1. The hydrophilic surface however now contains salt bridges on the hetero dimer interface and on the interfaces between dimer units within the hetero hexamer. In solution, the hexamers are unlikely to be in a perfect 1:1 assembly of peptide 1 and peptide 4 due to monomer swapping between hexamers in equilibrium. This exchange and resulting partial loss of electrostatic stabilization accounts for the slight increase in stability of solutions of a mixture of the two peptides (Figure 8, Table 6). To promote the salt bridging on the ACC-Hex surface, we designed peptide 5, which maximizes salt bridging between oppositely charged residues within the antiparallel configuration. Peptide 5 exhibited extremely high resistance to denaturation and did not appear to denature at saturating concentrations of Gdm-Cl (Figure 8). The combination of salt bridging along the solvent exposed surface and the formation of the Phe-Ile zipper with the hydrophobic core generates an extremely stable oligomer. The fact that peptide 1 is reasonably stable to chemical denaturation, even without salt bridging and with the destabilizing effect of Glu-Glu and Lys-Lys electrostatic repulsion, indicates the stabilizing effect of the tight hydrophobic core of the Phe-Ile zipper.

Table 6: Gdm-Cl Titration Results for Peptides **1**, **4**, and **5** in Gdm-Cl.

peptide	fit model	ΔG_u^w kcal•mol^{-1}	m kcal•mol^{-1}•M^{-1}	$m_{N \to I}$ kcal•mol^{-1}•M^{-1}
1	3-state	2.65 ± 0.36	1.31 ± 0.14	1.17 ± 0.12
4	3-state	3.38 ± 0.69	2.72 ± 0.46	1.85 ± 0.43
1+4	3-state	5.47 ± 1.15	2.29 ± 0.50	2.08 ± 0.51
5	–	high	–	–

4.3.5 Alternative *de novo* sequence utilizing Phe-Ile zipper forms antiparallel coiled-coil hexamers:

Peptides 1–5 contain the same base sequence in which the large residues are at the a positions and the aliphatic residues are at the d positions. In ACC-Hex, the Phe residues project outward and lay over the Ile residues and the Ile residues are pointed toward the seam of the dimer interface. Switching the Phe and Ile positions, Phe at the d positions and Ile at the a positions, does not permit the formation of an antiparallel hexamer (data not shown). Mapping this sequence onto the X-ray structure of peptide 1 shows that the alignment and pitch of each helix in ACC-Hex forces the Phe residues of the a to d swapped monomer to adopt a conformation with significant steric clashing between adjacent monomers, preventing hexamer formation.
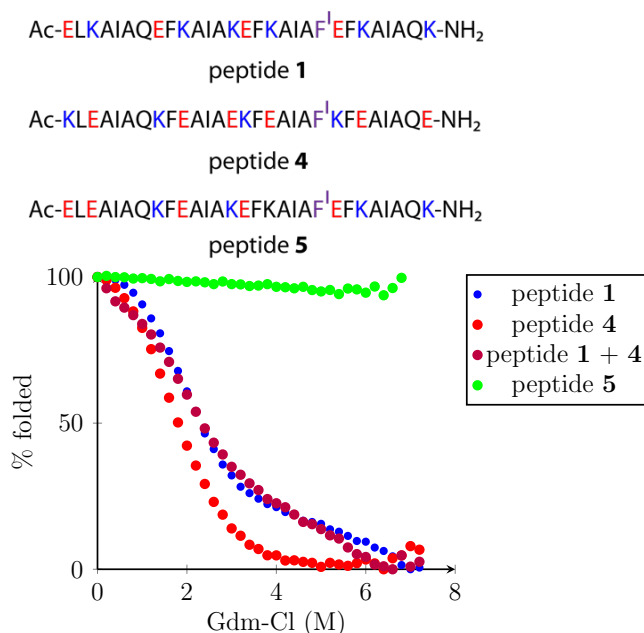

Figure 8: CD titration spectra of peptide 1, peptide 4, peptide 1 and 4 (1:1), and peptide 5 in 100 mM potassium phosphate with guanidinum chloride (Gdm-Cl) 0-8 M. CD measurements were recorded at 222 nm wavelength and at a temperature of 20 °C.

To further explore the general Phe-Ile zipper motif we designed peptide 6 in which the repeating begins at the d-position within the heptad repeat. This frame shift maintains the Phe residues at the a positions and Ile residues at the d positions and creates a unique peptide sequence. This also places the Ala residues at the e and g positions which has been shown to promote coiled-coil heptamer formation.[31] Peptide 6, however, formed hexamers and the X-ray crystal structure shows little difference in the size and shape of the antiparallel hexamer to that of ACC-Hex, with the exception of the hydrophobic core. The residues within the core of peptide 6 are frame shifted relative to ACC-Hex, starting the Phe-Ile pattern at the Phe residue instead of Ile within the hydrophobic core (Figure 9). The formation of ACC-Hex by peptide 6 suggests that the Phe-Ile zipper is a general interaction motif and a driving force for specific interaction and alignment of α-helices and controlled oligomerization.
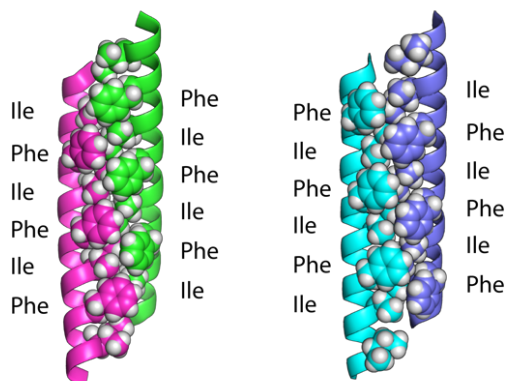
Figure 9: Antiparallel dimer interface formed in the X-ray structure of peptide 1 (left) and antiparallel dimer interface formed in the X-ray structure of peptide 6 (right).

4.4 CONCLUSIONS

The Phe-Ile zipper represents a general motif where large hydrophobic residues at a-positions selectively interact with aliphatic residues at the d-positions within a heptad repeat. The additional geometric constraints placed upon this arrangement, due to the nature of the side chains, permits only an antiparallel orientation of the helices. Even with these structural constraints, the Phe-Ile zipper motif permits a variety of unnatural and natural amino acid combinations. Manipulations of these residues combinations reveal the boundaries of this motif, with Val and Tyr variants unable to form hexamers and the Cha variant forming very stable hexamers. While other manipulations at the a and d positions did not appear to greatly affect the ability of the peptides to form hexamers, SEC-SAXS and CD titrations revealed subtle differences between the stabilities of these sequences.

The sequence and structure of peptide 1 was not predicted to form antiparallel hexamers. The antiparallel arrangement of the monomers within the hexamer prevents salt bridging of oppositely charged residues. Optimizing the sequence to permit salt bridging residues on the solvent exposed surface while in the antiparallel arrangement, peptide 5, generated hexamers that were extremely stable to denaturant. The generality of the Phe-Ile zipper is further expanded upon with peptide 6, forming an assembly nearly identical to that of peptide 1 but with a unique peptide sequence. Much like the Leu zipper motif, the Phe-Ile zipper motif can be envisioned to be a powerful tool in controlling molecular assemblies at the atomic level.

4.5 MATERIALS AND METHODS

Synthesis and purification of peptides 1–6: Peptides 1–6 were synthesized and purified according to methods described previously.[33]

Crystallization procedure for peptides 1 + 4 and peptide 6: Crystallization procedures were performed similarly to those described previously.[33–36] Crystallization conditions for peptide 1 + 4 and peptide 6 are shown in Table 2.

X-ray diffraction data collection, data processing, and structure determination for peptides 1 + 4 and peptide 6: X-ray diffraction data sets for peptides 1 + 4 and peptide 6 were collected at the Advanced Light Source (ALS) at the Lawrence Berkeley National Laboratory (Berkeley, California) on synchrotron beamline 8.2.1 at 1.00 Å wavelength with 0.5° rotation per image (Table 2). Diffraction data were scaled and merged using iMosflm and Aimless.[37,38]

Structure determination of peptides 1+ 4 and peptide 6: The electron density map of peptides 1 + 4 and peptide 6 was determined by single- anomalous diffraction (SAD) phasing techniques. Electron density map generation and refinement were performed similarly to previously published methods.[33–36] Table 2 shows the statistics of data collection and model refinement for peptides 1 + 4 and peptide 6.

Size-exclusion chromatography of peptides 1–6: The oligomerization of peptides 1–6 were analyzed by size-exclusion chromatography (SEC) at 5 °C in 100 mM potassium phosphate buffer at pH 7.4. Peptides 1-6 were dissolved in potassium phosphate buffer to a concentration of 1 mM and loaded onto a GE Superdex 75 10/300 GL column at a flow rate 0.8 mL/min. Chromatograms were recorded at 280 nm and normalized to the highest absorbance value. Standards (carbonic anhydrase, cytochrome C, and aprotinin) were eluted similarly to that of the peptides 1–6.

Size exclusion coupled small-angle X-ray scattering of peptides 1–3: Small-angle X-ray scattering (SAXS) profiles of peptides 1–3 were collected on SIBYLS beamline (12.3.1) at the Advanced Light Source (ALS) at the Lawrence Berkeley National Laboratory (Berkeley, California). Peptides 1–3 were dissolved in 100 mM potassium phosphate to a concentration of 1 mM and eluted on a Shodex KW402.5-4F at a rate of 0.4 mL/min. Samples were continuously exposed to the synchrotron source and profiles were collected every 2 seconds over a 25 min elution. Profiles containing the peptides of inter- est were merged to create a single SAXS profile. SAXS profiles were analyzed using the programs ATSAS and MultiFOXS.[39,40]

Circular dichroism of peptides 1–5: The conformation of peptides 1 were studied by circular dichroism (CD). Peptides 1–5 were dissolved in 100 mM postassium phophate buffer at pH 7.4 to a concentration of 40 μM. CD spectra were recorded on a Jasco J-810 Spectropolarimeter equipped with a Peltier thermoelectric temperature control device. The CD spectrum for peptides 1—5 were recorded between 200–260 nm wavelength, at 20 °C, and in a 1 cm path length cell.

Guanidinium titrations of peptides 1–5: Guanidinium chloride (Gdm-Cl) titrations of peptides 1–5 were performed using a Jasco ATS-429 titrator. Molar ellipticity was recorded at 222 nm wavelength. Each titration experiment was performed identically. A stock solution of 8M Gdm-

Cl in 100 mM potassium phosphate was prepared. The stock solution was added in 0.2 M increments to a solution of 40 μM peptide in 100 mM potassium phosphate at pH 7.4 and at 20 °C. After each addition, solutions were mixed for 90 seconds before recording ellipticity. For peptide 2c, additional titrations were performed at 60 °C, 70 °C, and 80 °C .

Titration curves were fitted to the following equations: $\Delta G_u = \Delta G_u{}^w - m \cdot D$

With $\Delta G_u = -RT \ln(K_D)$ and $m = \delta \Delta G_u / \delta D$, where D is the concentration of Gdm-Cl. For the two state model, curves were fit to the following equation:

$$\vartheta_{obs} = \frac{a + b*D + (c + d*D)e^{(-\Delta G_u{}^w + m*D)/RT}}{1 + e^{(-\Delta G_u{}^w + m*D)/RT}}$$

With a and c corresponding to the fractional amount of θ_N and θ_U for the folded and unfolded states, respectively. Values b and d corresponding to $(\Delta\theta_N/\Delta D)$ and $(\Delta\theta_U/\Delta D)$, respectively. For the 3-state model, involving an intermediate, curves were fit to the following equation:

$$\vartheta_{obs} = \frac{a + b*D + (c + d*D)*A*e^{(-\Delta G_u{}^w + m*D)/RT}}{1 + A*e^{(-\Delta G_u{}^w + m*D)/RT}}$$

with:

$$A = \frac{1}{1 + K_{01}*e^{(m_1*D/RT)}}$$

With K_{01} corresponding to the equilibrium constant for the folded (N) to intermediate (I) state and m_1 corresponding to the m-value for the folded (N) to intermediate (I).[41]

Table 2: Crystallographic Properties, Crystallization Conditions, and Data Collection and Model Refinement Statistics for Peptides **1** + **4** and Peptide **6**.

	peptide **1** + **4**	peptide **6**
PDB ID	5VTE	5WOJ
space group	$R32$	$R32$
a, b, c (Å)	48.97 48.97 141.82	52.56 52.56 93.04
α, β, γ (°)	90 90 120	90 90 120
peptide per asymmetric unit	2	2
crystallization conditions	0.1 M sodium formate, pH 6.75, 24% PEG 3350	0.1 M sodium formate, pH 6.5 35% PEG 3350
Data Collection[1]		
wavelength (Å)	1.00	1.00
resolution (Å)	47.27–2.02 (2.10–2.02)	40.89 – 2.201 (2.28–2.20)
total reflections	22746 (1266)	17753 (2079)
unique reflections	4228 (342)	2667 (300)
multiplicity	5.4	6.7
completeness (%)	93 (89)	99.9 (100)
mean I/σ	10.63 (3.76)	13.9 (5.53)
Wilson B-factor	20.58	32.30
R_{merge}	0.04 (0.09)	0.070 (0.285)
R_{measure}	0.06	0.076
$CC_{1/2}$	0.99 (0.97)	0.99 (0.96)
CC^*	1.00 (0.99)	1 (0.99)
Refinement		
R_{work}	21.73	22.87
R_{free}	24.73	27.95
number of non-hydrogen atoms	519	513
RMS_{bonds}	0.003	0.003
RMS_{angles}	0.59	0.76
Ramachandran		
favored (%)	100	100
outliers (%)	2.6	0
clashscore	0.00	0.00
average B-factor	29.66	47.94

1. Values for the highest resolution shell are show in parentheses.

4.6 REFERENCES

1. Landschulz, W. H.; Johnson, P. F.; McKnight, S. L. (1988) The leucine zipper: a hypothetical structure common to a new class of DNA binding proteins. Science 240, 1759–1764.
2. O'Shea, E. K.; Klemm, J. D.; Kim, P. S.; Alber, T. (1991) X-ray structure of the GCN4 leucine zipper, a two-stranded, parallel coiled coil. Science 254, 539–544.
3. Hadley, E. B.; Gellman, S. H. (2007) An antiparallel alpha-helical coiled-coil model system for rapid assessment of side-chain recognition at the hydrophobic interlace. Biopolymers 88, 586–586.
4. Hadley, E. B.; Testa, O. D.; Woolfson, D. N.; Gellman, S. H. (2008) Preferred side- chain constellations at antiparallel coiled-coil interfaces. P. Natl. Acad. Sci. U. S. A. 105, 530–535.
5. Grigoryan, G.; Keating, A. E. (2008) Structural specificity in coiled-coil interactions. Curr. Opin. Struct. Biol. 18, 477–483.
6. Grigoryan, G.; Degrado, W. F. (2011) Probing designability via a generalized model of helical bundle geometry. J. Mol. Biol. 405, 1079–1100.
7. Fletcher, J. M.; Boyle, A. L.; Bruning, M.; Bartlett, G. J.; Vincent, T. L.; Zaccai, N. R.; Armstrong, C. T.; Bromley, E. H.; Booth, P. J.; Brady, R. L.; Thomson, A. R.; Woolfson, D. N. (2012) A basis set of de novo coiled-coil peptide oligomers for rational protein design and synthetic biology. ACS Synth. Biol. 1, 240–250.
8. Crick, F. H. C. (1953) The packing of alpha-helices - simple coiled-coils. Acta Crystallographica 6, 689–697.
9. Tsuruda, P. R.; Julius, D.; Minor, J., D. L. (2006) Coiled coils direct assembly of a cold-activated TRP channel. Neuron 51, 201–212.
10. Mason, J. M.; Arndt, K. M. (2004) Coiled coil domains: stability, specificity, and biological implications. Chembiochem 5, 170–176.
11. Rose, A.; Meier, I. (2004) Scaffolds, levers, rods and springs: diverse cellular functions of long coiled-coil proteins. Cell Mol. Life Sci. 61, 1996–2009.
12. Dong, H.; Paramonov, S. E.; Hartgerink, J. D. (2008) Self-assembly of alpha-helical coiled coil nanofibers. J. Am. Chem. Soc. 130, 13691–13695.
13. Burgess, N. C.; Sharp, T. H.; Thomas, F.; Wood, C. W.; Thomson, A. R.; Zaccai, N. R.; Brady, R. L.; Serpell, L. C.; Woolfson, D. N. (2015) Modular design of self-assembling peptide-based nanotubes. J. Am. Chem. Soc. 137, 10554–10562.
14. Burton, A. J.; Thomas, F.; Agnew, C.; Hudson, K. L.; Halford, S. E.; Brady, R. L.; Woolfson, D. N. (2013) Accessibility, reactivity, and selectivity of side chains within a channel of de novo peptide assembly. J. Am. Chem. Soc. 135, 12524–12527.
15. Dube, N.; Seo, J. W.; Dong, H.; Shu, J. Y.; Lund, R.; Mahakian, L. M.; Ferrara, K. W.; Xu, T. (2014) Effect of alkyl length of peptide-polymer amphiphile on cargo encapsulation stability and pharmacokinetics of 3-helix micelles. Biomacromolecules 15, 2963– 2970.
16. Mi, L.; Fischer, S.; Chung, B.; Sundelacruz, S.; Harden, J. L. (2006) Self-assembling protein hydrogels with modular integrin binding domains. Biomacromolecules 7, 38–47.
17. Bale, J. B.; Gonen, S.; Liu, Y.; Sheffler, W.; Ellis, D.; Thomas, C.; Cascio, D.; Yeates, T. O.; Gonen, T.; King, N. P.; Baker, D. (2016) Accurate design of megadalton- scale two-component icosahedral protein complexes. Science 353, 389–394.
18. Nicholls, A.; Sharp, K. A.; Honig, B. (1991) Protein folding and association: insights from the interfacial and thermodynamic properties of hydrocarbons. Proteins 11, 281– 296.

19. Dill, K. A.; Chan, H. S. (1997) From Levinthal to pathways to funnels. Nat Struct Biol 4, 10–19.
20. Dill, K. A.; Ozkan, S. B.; Shell, M. S.; Weikl, T. R. (2008) The protein folding problem. Annu Rev Biophys 37, 289–316.
21. Adamson, J. G.; Zhou, N. E.; Hodges, R. S. (1993) Structure, function and application of the coiled-coil protein folding motif. Curr. Opin. Biotechnol. 4, 428–437.
22. Ogihara, N. L.; Ghirlanda, G.; Bryson, J. W.; Gingery, M.; DeGrado, W. F.; Eisen- berg, D. (2001) Design of three-dimensional domain-swapped dimers and fibrous oligomers. Proc. Natl. Acad. Sci. U. S. A. 98, 1404–1409.
23. Straussman, R.; Ben-Ya'acov, A.; Woolfson, D. N.; Ravid, S. (2007) Kinking the coiled coil–negatively charged residues at the coiled-coil interface. J. Mol. Biol. 366, 1232– 1242.
24. Steinkruger, J. D.; Woolfson, D. N.; Gellman, S. H. (2010) Side-chain pairing prefer- ences in the parallel coiled-coil dimer motif: insight on ion pairing between core and flanking sites. J. Am. Chem. Soc. 132, 7586–7588.
25. Schnarr, N. A.; Kennan, A. J. (2004) Strand orientation by steric matching: a designed antiparallel coiled-coil trimer. J. Am. Chem. Soc. 126, 14447–14451.
26. Stetefeld, J.; Jenny, M.; Schulthess, T.; Landwehr, R.; Engel, J.; Kammerer, R. A. (2000) Crystal structure of a naturally occurring parallel right-handed coiled coil tetramer. Nat. Struct. Biol. 7, 772–776.
27. Liu, J.; Deng, Y.; Zheng, Q.; Cheng, C. S.; Kallenbach, N. R.; Lu, M. (2006) A parallel coiled-coil tetramer with offset helices. Biochemistry 45, 15224–15231.
28. Sales, M.; Plecs, J. J.; Holton, J. M.; Alber, T. (2007) Structure of a designed, right- handed coiled-coil tetramer containing all biological amino acids. Protein Sci. 16, 2224– 2232.
29. Slovic, A. M.; Lear, J. D.; DeGrado, W. F. (2005) De novo design of a pentameric coiled- coil: decoding the motif for tetramer versus pentamer formation in water-soluble phospholamban. J. Pept. Res. 65, 312–321.
30. Zaccai, N. R.; Chi, B.; Thomson, A. R.; Boyle, A. L.; Bartlett, G. J.; Bruning, M.; Linden, N.; Sessions, R. B.; Booth, P. J.; Brady, R. L.; Woolfson, D. N. (2011) A de novo peptide hexamer with a mutable channel. Nat. Chem. Biol. 7, 935–941.
31. Liu, J.; Zheng, Q.; Deng, Y.; Cheng, C. S.; Kallenbach, N. R.; Lu, M. (2006) A seven- helix coiled coil. Proc. Natl. Acad. Sci. U. S. A. 103, 15457–15462.
32. Liu, J.; Zheng, Q.; Deng, Y.; Kallenbach, N. R.; Lu, M. (2006) Conformational transi- tion between four and five-stranded phenylalanine zippers determined by a local packing interaction. J. Mol. Biol. 361, 168–179.
33. Spencer, R. K.; Hochbaum, A. I. (2016) X-ray Crystallographic Structure and Solu- tion Behavior of an Antiparallel Coiled-Coil Hexamer Formed by de Novo Peptides. Biochemistry 55, 3214–3223.
34. Spencer, R. K.; Li, H.; Nowick, J. S. (2014) X-ray crystallographic structures of trimers and higher-order oligomeric assemblies of a peptide derived from Abeta(17-36). J. Am. Chem. Soc. 136, 5595–5598.
35. Spencer, R. K.; Kreutzer, A. G.; Salveson, P. J.; Li, H.; Nowick, J. S. (2015) X-ray crystallographic structures of oligomers of peptides derived from beta-microglobulin. J. Am. Chem. Soc. 137, 6304–6311.
36. Spencer, R. K.; Nowick, J. S. (2015) A newcomer's guide to peptide crystallography. Isr. J. Chem. 55, 698–710.

37. Battye, T. G.; Kontogiannis, L.; Johnson, O.; Powell, H. R.; Leslie, A. G. (2011) iMOSFLM: a new graphical interface for diffraction-image processing with MOSFLM. Acta Crystallogr. D Biol. Crystallogr. 67, 271–281.
38. Evans, P. R.; Murshudov, G. N. (2013) How good are my data and what is the resolution? Acta Crystallogr., Sect. D: Biol. Crystallogr. 69, 1204–1214.
39. Putnam, C. D.; Hammel, M.; Hura, G. L.; Tainer, J. A. (2007) X-ray solution scattering (SAXS) combined with crystallography and computation: defining accurate macromolecular structures, conformations and assemblies in solution. Q. Rev. Biophys. 40, 191–285.
40. Schneidman-Duhovny, D.; Hammel, M.; Tainer, J. A.; Sali, A. (2013) Accurate SAXS profile computation and its assessment by contrast variation experiments. Biophys. J. 105, 962–974.
41. Soulages, J. L. (1998) Chemical denaturation: potential impact of undetected intermediates in the free energy of unfolding and m-values obtained from a two-state assumption. Biophys. J. 75, 484–492.
42. Petoukhov, M. V.; Franke, D.; Shkumatov, A. V.; Tria, G.; Kikhney, A. G.; Gajda, M.; Gorba, C.; Mertens, H. D.; Konarev, P. V.; Svergun, D. I. (2012) New developments in the ATSAS program package for small-angle scattering data analysis. J. Appl. Crystal- logr. 45, 342–350.
43. Dyer, K. N.; Hammel, M.; Rambo, R. P.; Tsutakawa, S. E.; Rodic, I.; Classen, S.; Tainer, J. A.; Hura, G. L. (2014) High-throughput SAXS for the characterization of biomolecules in solution: a practical approach. Methods Mol. Biol. 1091, 245–258.
44. Santoro, M. M.; Bolen, D. W. (1992) A test of the linear extrapolation of unfolding free energy changes over an extended denaturant concentration range. Biochemistry 31, 4901–4907.
45. Peptide 2c resisted denaturation up to the highest Gdm-Cl concentration tested at room temperature (Figure 5) and did not fully denature in >7 M Gdm-Cl below 60 °C. The ΔG_u^w and m-value for peptide 2c was determined at 60 °C, 70 °C, and 80 °C and averaged.
46. Myers, J. K.; Pace, C. N.; Scholtz, J. M. (1995) Denaturant m values and heat capacity changes: relation to changes in accessible surface areas of protein unfolding. Protein Sci. 4, 2138–2148.
47. Accessible solvent area (ASA) was calculated in PyMol. Calculated m-values were determined with the following equation $m_{calc} = 953 + 0.23 \cdot (\Delta ASA)$.[46]

CHAPTER 5

Electronic Conductivity in Coiled-Coil Peptide Nanofibers and Gels

5.1 SUMMARY

Examples of long-range electronic conductivity are rare in biological systems. The observation of micrometer-scale electronic transport through protein wires produced by bacteria is therefore notable, providing an opportunity to study fundamental aspects of conduction through protein-based materials and natural inspiration for bioelectronics materials. Borrowing sequence and structural motifs from these conductive protein fibers, we designed self-assembling peptides that form electronically conductive nanofibers under aqueous conditions. Conductivity in these nanofibers is distinct for two reasons: first, they support electron transport over distances orders of magnitude greater than expected for proteins, and second, the conductivity is mediated entirely by amino acids lacking extended conjugation, π-stacking, or redox centers typical of existing organic and bio-hybrid semiconductors. Electrochemical transport measurements show that the fibers support ohmic electronic transport and a metallic-like temperature dependence of conductance in aqueous buffer. At higher solution concentrations, the peptide monomers form hydrogels, and comparisons of the structure and electronic properties of the nanofibers and gels highlight the critical roles of α-helical secondary structure and supramolecular ordering in supporting electronic conductivity in these materials. These findings suggest a structural basis for long-range electronic conduction mechanisms in peptide and protein biomaterials.

5.2 INTRODUCTION

Bioelectronic materials aim to interface synthetic electronic devices with biological systems, from biomolecules to cells, tissues, and entire organisms.[1] Such a union of solid-state and biological materials enables a broad range of applications such as wearable[2,3] or implantable devices,[4,5] portable and biocompatible power sources,[6–8] real-time and miniaturized sensors,[9,10] and bionic neural interfaces.[11,12] Finding ideal materials to bridge the biological-electronic interface remains an outstanding challenge.[13] Such a material should be biocompatible, multifunctional, and maintain proper function of the interacting biological system.[14] Proteins and peptides are ideal material building blocks for satisfying these criteria due to their properties of self-assembly and functional molecular recognition.[15–18] In addition, the chemical diversity and specificity of amino acid sequences can be designed to drive the formation of peptide nanostructures, such as wires and tubes.[19,20] These nanometer length scales are comparable to those of biological building blocks, promoting a more seamless integration at the bio-electronic interface than existing micrometer-scale electronic transducers.[17,21]

Processes of electron tunneling and transfer across individual enzymes are common in biology, [22,23] and electronic conductivity or tunneling in non-enzyme protein and peptide nanomaterials has been studied over short (~nm) distances.[24–26] Over much longer (~μm) distances, inherent electronic conductivity has been established in bacterial protein fiber appendages, called pili, of some anaerobic species.[27,28] Long-range electron transport in conductive pili represents natural inspiration for molecular bioelectronics design and a tunable synthetic platform for studying the electronic properties of conductive protein nanostructures.[27,29] Pili support charge transport through natural amino acid residues over micrometer-scale distances,[30,31] much farther than the angstrom to nanometer length scales associated with tunneling.[22,23,32] They are also are orders of magnitude more conductive than

amyloid[33] and π-stacked peptide fibers.[34] Unlike examples of long-range electron transport in natural[35] and synthetic assemblies of cytochromes, the conduction observed in pili is not redox-mediated,[28,36] and the exact mechanism of electron transport in these protein fibers is still a matter of debate.

π-stacked moieties are essential for long-range electron conductivity in synthetic peptide bio-organic hybrid nanostructures, in which peptides direct the self-assembly of small molecule semiconductors.[37,38] π-stacking amino acid side chains may be important in pili as well. The conductivity of *Geobacter sulfurreducens* Type IV pili, the most commonly studied conductive pilus system, is sensitive to mutations at aromatic residues,[39–41] and pilus conductivity correlates with aromatic amino acid content of pilin protein building blocks from different *Geobacter* species.[42] Some homology models suggest sufficiently small distances between aromatic residues in the pilus for π-stacking interactions,[29,43,44] but without a crystal structure, such a molecular arrangement has not been conclusively determined. On the other hand, some self-assembled peptide monolayers[24,45–47] and short peptide nanotubes[48] exhibit inherent conductivity over distances up to several nanometers without π-stacking. The composition of the side chains, hydrogen bonds, and an α-helical secondary structure have been identified as important factors contributing to the hopping and tunneling conductivity in these peptide systems over short distances.

Taking sequence and structural inspiration from *G. sulfurreducens* pili, we designed a self-assembling *de novo* peptide that forms electrically conductive nanofibers.[49,50] The peptide self-associates in solution to form coiled-coil hexamers, which were designed to add end-to-end and form elongated nanofibers. Both the peptide nanofibers and the *Geobacter* pili consist of α-helical monomer building blocks, and the crystal structure of the coiled-coil hexamer shows that the peptide oligomer clusters aromatic residues axially in their hydrophobic core.[49] Importantly, the spacing and arrangement of aromatic side chains preclude π-stacked electronic delocalization in proposed structure of the peptide nanofibers. Nonetheless, these nanofibers are conductive in ambient and wet conditions, and they exhibit metallic-like trends in electrochemical and temperature-dependent transport measurements. Comparison of the structure and conductance of fiber and gel morphologies formed by the peptide at different concentrations suggests that the supramolecular ordering of peptides within the nanofibers plays a critical role in supporting electronic transport. The observed properties and mutability of the peptide sequence suggests that this nanofiber system may serve as an experimental platform for exploring structure-property relationships in peptide and protein bioelectronics materials.

5.3 RESULTS AND DISCUSSION
### 5.3.1 Peptide Nanofiber Self-Assembly:
Peptide **1** (Fig. 1A) self-assembles to incorporate aromatic amino acids into the core of an antiparallel coiled-coil hexamer (ACC-Hex, PDB 5EOJ) structure, which it adopts in solid-state crystals and in solution.[49,50] Peptide **1** is capped with Glu and Lys residues to induce end-to-end electrostatic interactions and the formation of elongated fibers. The X-ray crystallographic structure shows that peptide **1** indeed crystallizes as stacked ACC-Hex building blocks, suggesting supramolecular assembly of fibers driven by these electrostatic interactions (Fig. 1B). Atomic force microscopy (AFM) imaging confirms the formation of nanofiber structures from peptide **1** in phosphate buffered saline (PBS) at 100-200 μM concentrations (0.03-0.06 % w/v), which form overnight and extend up to several microns in length (Fig. 2A). Height profiles of the observed nanofibers exhibit a minimum diameter of 2 nm (Fig. 2B), consistent with the diameter

of a single hexamer unit.[49] That this is the smallest diameter of nanofiber measured in the sample suggests that these nanofibers are composed of ACC-Hex building blocks, and that larger diameter fibers may be bundles of ACC-Hex nanofibers.
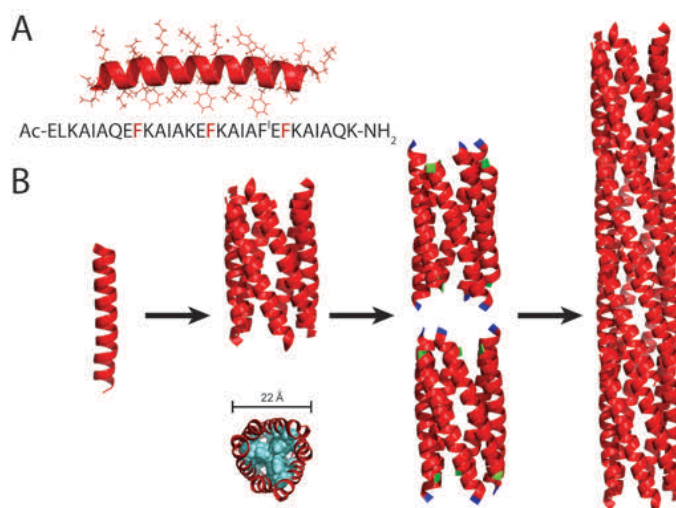
Figure 1. A) Peptide **1** monomer crystal structure and sequence. Red residues highlight the phenylalanines buried in the hydrophobic core; F^I denotes the iodo-phenylalanine on the solvent-exposed surface used for phasing in crystal structure determination. B) Proposed nanofiber self-assembly mechanism from X-ray crystal structures of peptide **1**. *Left to Right*: Peptide **1** monomer forms an antiparallel coiled-coil hexamer (ACC-Hex), shown in radial (top) and axial (bottom) projections; ACC-Hex stacks end-to-end *via* electrostatic interactions between the terminal glutamic acids (green) and amide lysines (dark blue) to form an elongated fiber. The hexamer and extended nanofiber have a predicted diameter of 22 Å filled with a tightly packed hydrophobic core of aromatic residues.
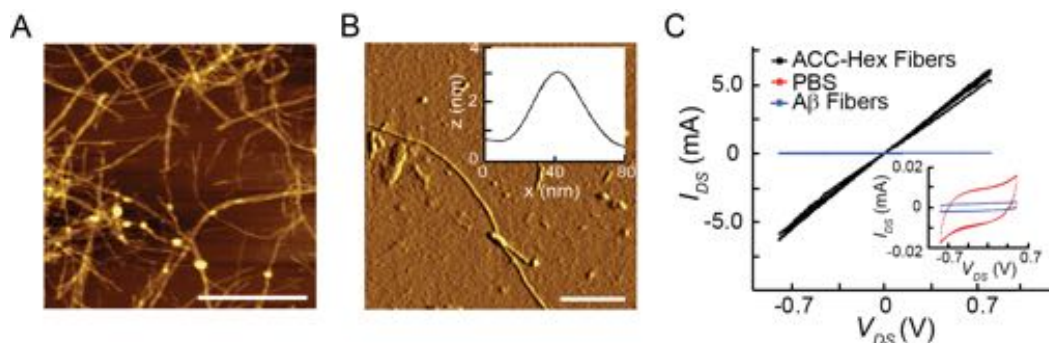

Figure 2. (A) Atomic force micrograph of a drop-cast film of ACC-Hex nanofibers. (B) AFM topographical image of a single ACC-Hex nanofiber. Inset shows a z-height line-scan across the fiber, indicating a fiber diameter of 2.3 nm. (C) Current-voltage (*I-V*) characteristics of ACC-Hex fibers, a dried buffer control (PBS), and amyloid-β (Aβ) fibers. Inset: close-up of PBS and Aβ *I-V*s. Scale bars are 5 μm and 500 nm in (A) and (B), respectively.

5.3.2 Electrical Conductivity of Peptide Nanofibers:

Films deposited from dried ACC-Hex nanofiber suspensions form dense percolation networks that exhibit long-range electronic conductivity. *I-V* characteristics of dried nanofiber films on interdigitated electrode devices exhibit linear behavior (Fig. 2C), with an average resistance of 188 ± 36 Ω (*n* = 6 independent samples). The measured resistance is relatively low for typical organic materials due to the large channel width and short channel length of the interdigitated devices used for electronic property characterization (see Methods). Films of amyloid beta fibers (Aβ), cast onto identical devices from an equivalent volume of solution and concentration of

protein, have a resistance of 1.0×10^8 Ω. The equivalent volume of PBS cast onto identical devices has a resistance of 1.5×10^9 Ω, indicating that any residual contamination from the casting solution contributes negligible conductance to the peptide **1** nanofiber films. Aβ fibers were used as a control material because they assemble with similar aspect ratios to ACC-Hex fibers and contain aligned aromatic residues.[51] The six orders of magnitude decrease in conductance of the Aβ compared to ACC-Hex nanofiber films suggests a primary role for the α-helical building blocks of ACC-Hex. α-helical secondary structure has been previously demonstrated to lower the energetic barrier for transport across short homopeptides.[24] Our results are consistent with these tunneling conduction experiments and the proposed importance of α-helices to conductivity in *G. sulfurreducens* pili.[28,43] Using an identical electrode geometry, our ACC-Hex nanofiber films exhibit comparable (~mA) current to pili films. 6.9 μg of ACC-Hex nanofibers yielded an average film resistance of 188 Ω, while 115 μg of purified *G. sulfurreducens* pili on the same devices had a resistance of 470 Ω.[28]

 Single fiber *I-V* characteristics of ACC-Hex nanofibers were used to confirm electronic conduction in the fiber component of the self-assembled peptide and to calculate values of electrical conductivity inherent to the nanofibers. Conductive probe AFM measurements of electron transport in individual ACC-Hex nanofibers show high conductivity values, with an average conductivity of 1.12 ± 0.77 S/cm ($n = 4$ independent nanofibers). Wild-type *G. sulfurreducens* pili have conductivities ranging from 0.188 ± 0.034 S/cm (pH 2) to 0.051 ± 0.019 S/cm (pH 7),[31] consistent with the relative resistances obtained from *I-V*s of the ACC-Hex nanofiber and pili films.
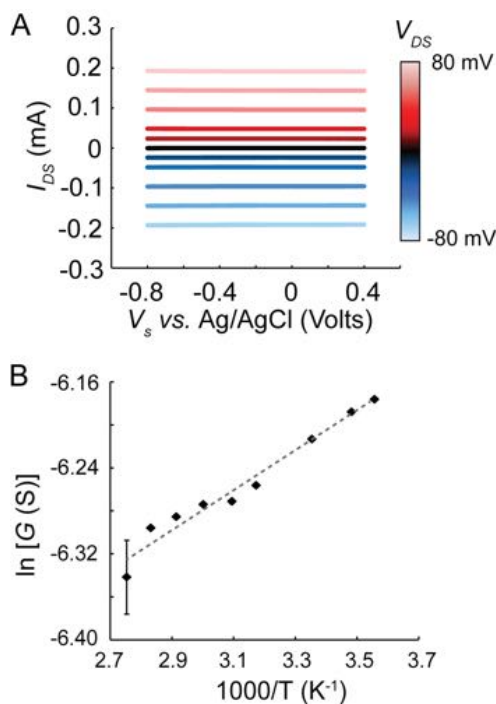
Figure 3. Electrochemical gating experiments of ACC-Hex fiber films (A) Source-drain current (I_{DS}) of ACC-Hex nanofiber films gated in solution (pH 7.0) with respect to a reference electrode (V_S). The source-drain voltage (V_{DS}) of each scan is indicated by the color scale on the right. (B) The average source-drain conductance (G) of peptide nanofiber films as a function of temperature at 10 different V_{DS} offsets (± 10 mV, ± 20 mV, ± 40 mV, ± 60 mV, and ± 80 mV). Error bars represent the standard deviation of measurements at all 10 V_{DS} values and are small as to be obscured by the data points at $T < 90$°C.

Electronic transport in ACC-Hex nanofibers was also characterized in aqueous solution by electrochemical gating measurements in a bipotentiostat setup. Bipotentiostat cyclic voltammetry distinguishes between redox-mediated and ohmic charge transport mechanisms in conductive channel materials.[28,52,53] Current through the ACC-Hex nanofiber channel is independent of gate potential and depends only on the source-drain potential, V_{DS} (Fig. 3A), indicative of band-like charge carrier conduction. The conductance of the nanofiber channels shows a weak dependence on pH and ionic strength, and it increases with decreasing temperature (Fig. 3B). The temperature-dependent behavior is also consistent with ohmic, or particle-like, charge conduction and is exclusive of thermally activated conduction mechanisms, such as charge hopping, in ACC-Hex nanofibers.

5.3.3 Peptide Hydrogel Formation and Rheological Properties:

Peptide **1** forms hydrogels at mM concentrations (above 0.1% w/v) after 20 min incubation at 70 °C. Visible gelation was observed at concentrations ranging from 0.1% to 5% w/v. Rheological studies were performed to measure the mechanical properties of the hydrogels (Fig. 4). Strain sweep experiments were performed to assess the storage modulus (G') and the loss modulus (G''), which measure the energy stored and dissipated upon application of oscillatory shear in the linear viscoelastic regime. When $G' >> G''$, the material is considered to behave like a viscoelastic solid, and when $G' << G''$, the material behaves like a viscoelastic liquid.[54] The magnitude of G' is also an indicator of the relative stiffness of the hydrogel.

Peptide **1** hydrogels demonstrate typical gel-like rheological behavior. G' is relatively constant and greater than G'' at low strain amplitudes, then at higher strains drops off quickly with increasing strain and crosses to a $G' < G''$ regime indicative of gel yielding (Fig. 4A). Also consistent with gel-like behavior, G'_0 (G' at 0.1% strain) increases with increasing concentration of peptide (Fig. 4B). The strain amplitude sweeps track the viscoelasticity of the various hydrogels. For the most robust gel (5% w/v), the critical strain γ_c occurs at a G' value of 160 Pa: below 3% strain, the structure is intact, as denoted by the strain independence of G' with $G' > G''$, suggesting a percolating stress-bearing network (Fig. 4A). Increasing the strain above γ_c disrupts the network structure, and the material eventually begins to resemble a viscous liquid at strains above the crossover point $G' = G''$. The value of γ_c increases with peptide concentration (Fig. 4A inset), indicating that the network structure responsible for load distribution increases in the presence of more material.[55]

The storage modulus G' of peptide gels follows a power law relationship with concentration, which is determined by factors such as fibril persistence length, fibril flexibility, distance between fibrils, and distance between fibril intersections, and which is directly related to the crosslinking or entanglement in the system.[56] In a crosslinked hydrogel, fibrils are linked by chemical bonds and the exponent n has a theoretical value of 2.5 for a dense crosslinking network.[56] n is predicted to have a value of 2.2 for entangled hydrogels[56] and 1.4 for strongly entangled hydrogels.[57] A value closer to $n = 1$, such as measured from the peptide **1** hydrogels ($n = 1.13$, Fig. 4B), indicates that the gels are semi-dilute viscoelastic solutions that are neither strongly entangled nor extensively crosslinked.[58] These structural characteristics are consistent with the short, rigid α-helical peptide **1** building block of the gels, the hydrophobic interactions driving oligomer and gel backbone assembly, and the lack of specific cross-linking moieties in the peptide **1** and ACC-Hex structures.
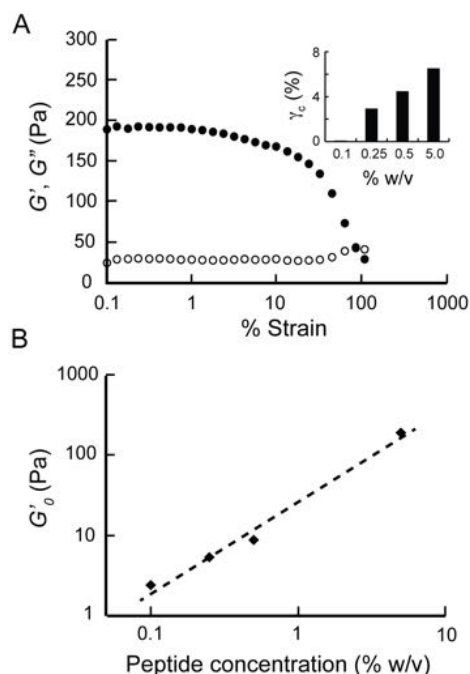
Figure 4. Oscillatory rheology measurements of peptide **1** hydrogels. (A) Representative strain sweep values of storage (G', filled circles) and loss (G'', open circles) moduli of the 5 % w/v hydrogel conducted at 0.1 Hz. Inset shows the critical strain, γ_c, *versus* concentration of peptide. (B) Storage modulus measured at 0.1% strain (G'_0) and 1 Hz, as a function of peptide concentration (% w/v). The slope of the fit line is 1.13.

5.3.4 Electronic Measurements of Peptide Hydrogels:

Films of dried hydrogels exhibit a surprising decrease in conductivity with increasing peptide concentration (Fig. 5A). Films cast from nanofibers solutions (0.03 % w/v) exhibit seven orders of magnitude greater conductance than those cast from equal volumes of 5% w/v peptide gels, despite the presence of more peptide material in films cast from higher concentration samples. The conductance of hydrated hydrogels was recorded by taking the inverse of resistance values obtained by electrical impedance spectroscopy (EIS) (Fig. 5B). Conductance through the material was determined by taking the inverse of the difference between impedance values at low frequencies, approaching DC conditions,[59,60] and the solution resistance (impedance value at high frequencies). The high frequency solution resistance values were negligible compared to the impedance values at low frequencies, approaching DC. As with the dried films, conductance through a fixed volume of nanofibers and hydrogel decreases precipitously with increasing peptide concentration. These data indicate that the peptide itself is not inherently conductive and suggest that the conductivity may be strongly dependent on the supramolecular structure present in highly ordered fiber morphology present at low peptide concentrations. SEM images confirm the lack of fiber morphology in peptide gels at concentrations above 0.1 % w/v (Fig. 5C), which instead form increasingly large and extended networks of clusters characteristic of hydrogel phase separation during sample desiccation.

5.3.5 Molecular Structure Insights into Peptide Nanofibers and Gels:

The solution dynamics and self-assembly of peptide **1** were investigated by molecular dynamics simulations using the coarse-grained MARTINI model for peptides in explicit water and ions. Simulation data show oligomer assembly structures and intermediates consistent with experimental results (Fig. 6). Firstly, the fast association of peptide **1** into dimers was observed

in equilibrium with ACC-Hex at ~ 10 µM (Fig. 6A-C). The presence of dimers was indicated experimentally by small-angle X-ray scattering profiles of peptide **1** at comparable concentrations, and by structural analysis of the ACC-Hex crystal structure.[49] Secondly, end-to-end association of individual ACC-Hex units was observed at higher concentrations (~ 100 µM, 0.03 %w/v), creating elongated structures suggestive of the initial stages of fiber assembly. The minimum diameter of observed peptide **1** fibers measured by AFM is approximately the ACC-Hex diameter (Fig. 2B), consistent with the end-to-end assembly process indicated by these MD data (Fig. 6D). Lastly, at mM concentrations (> 0.1 % w/v), simulation snapshots indicate a transition in supramolecular assembly of ACC-Hex building blocks into larger, branched structures (Fig. 6E). While the ACC-Hex building blocks are still stable at these concentrations, the hexamers no longer self-associate exclusively by end-to-end interactions, which would result in one-dimensional fiber growth. Rather, ACC-Hex units attach to ends and sides, creating continuous and branching junctions.
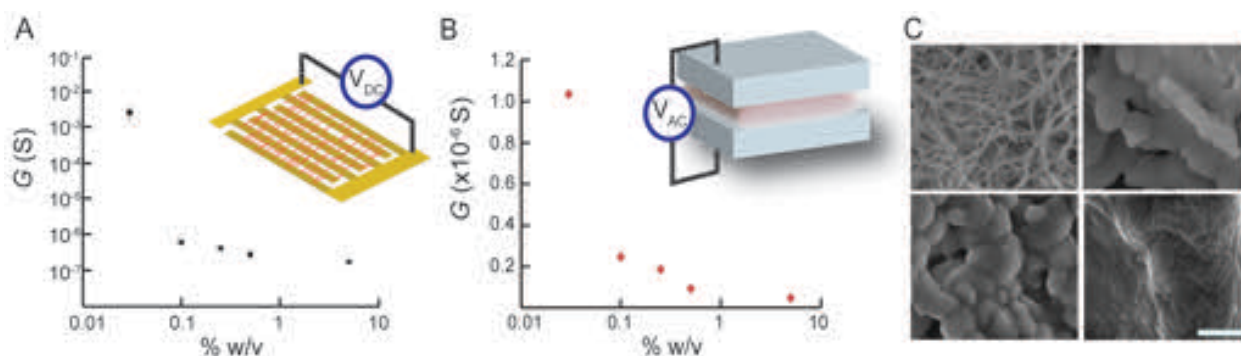

Figure 5. Conductance measurements of ACC-Hex nanofibers (0.03% w/v) and gels. (A) Conductance (*G*) of dried fibers and gels deposited from equivalent solution volumes onto interdigitated electrodes. Inset shows device schematic and example of fibers (red) bridging the interdigitated electrodes (gold). (B) Conductance approaching DC as determined by EIS in FTO sandwich electrodes (inset). (C) Scanning electron micrographs of ACC-Hex fibers (0.03% w/v) (*top left*), 0.25% hydrogel (*top right*), 0.5% hydrogel (*bottom left*), and 5% hydrogel (*bottom right*). Scale bar is 500 nm.

Fiber formation is experimentally observed between 100 and 200 µM (0.03 to 0.06% w/v), and these simulations demonstrate that within this range, the end-to-end axial association of ACC-Hex units represents the potential nucleation step of fiber formation. In contrast, at mM concentrations, the ACC-Hex building blocks associate *via* both lateral and axial interactions to form the branched network structure of the gel backbone. The simulations suggest that peptide **1** still assembles into ACC-Hex units at these high concentrations and bury Phe residues in the hydrophobic core of this gel network, but that the hexamer building blocks lack the axially aligned periodicity present at lower, fiber-forming concentrations of peptide. This structural change is observed in SEM preparations of the fibers and hydrogels (Fig. 5C) and is consistent with the rheological data (*G₀'* vs. concentration, Fig. 4B), which suggests that the peptide gel is weakly cross-linked and lacks chain entanglement. Both of these gel structure characteristics are expected from the short, rigid monomer of peptide **1** and the hydrophobic interactions holding them together in aggregates and the branched gel backbone.

Circular dichroism (CD) spectra of soluble ACC-Hex units, ACC-Hex nanofibers, and gels support the presence of intact oligomer units across all concentrations. CD spectra were acquired from solutions of different peptide concentrations that form isolated oligomers (ACC-Hex, 0.015 % w/v), fibers (0.03% w/v) or gels (0.1 and 5.0 % w/v) (Fig. 6F). In dilute solutions,

peptide **1** aggregates into ACC-Hex oligomers,[49] the CD spectrum of which (Fig. 6F) exhibits characteristic α-helical molar ellipticity minima around 208 nm and 220 nm.[61–64] As the peptide forms fibers and gels with increasing concentration, the 208 nm minimum disappears and the 220 nm minimum becomes increasingly red-shifted. These two distortions in the spectra are associated with chiral scattering due to the lateral aggregation of α-helices, further radial expansion of fiber bundles[62–64], and end-to-end assembly of the helices[65]. To verify that the 70 °C incubation used for gel formation does not preclude fiber assembly, we subjected a 0.03% w/v peptide sample, which forms fibers under standard aging conditions, to a 70 °C incubation and still observed aggregated fibers. The CD spectra, therefore, support the MD findings that the α-helical secondary structure and the ACC-Hex tertiary structure are maintained during the aggregation process associated with fiber and gel formation. In all, the structural data from rheological, molecular dynamics, and CD, in conjunction with electronic measurements suggest that the quaternary structure, *i.e.* the axial, end-to-end association of ACC-Hex units, of the nanofibers may be critical to their long-range electron conducting properties.
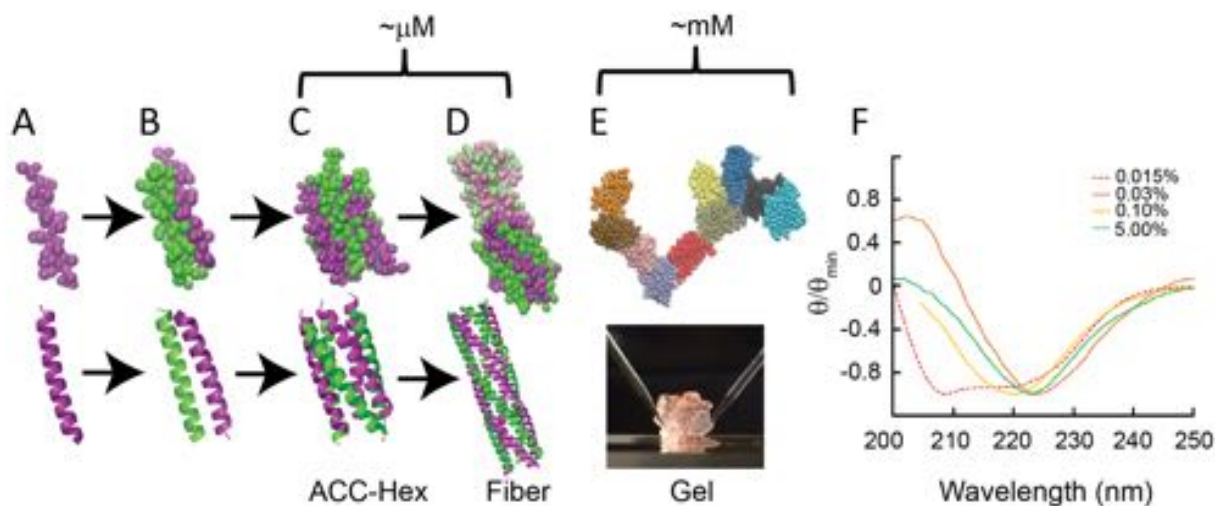
Figure 6. Assembly mechanism and structures of peptide **1** from simulations and CD spectra. (A-E) Molecular dynamics simulations (top) of peptide **1** self-assembly and the corresponding assemblies from the X-ray crystal structure (A-D bottom) or gel image (E bottom) of peptide **1**. All purple and all green colored peptides indicate α-helices oriented parallel to each other and antiparallel to the other color. At μM concentrations, peptide **1** forms ACC-Hex units (C), which are driven to stack end-to-end *via* electrostatic interactions (D). At mM concentrations (E), peptide **1** forms gels and a branched backbone structure composed of ACC-Hex units. In this simulation snapshot, peptide **1** monomers within the same hexamer are all colored identically. (F) Normalized CD spectra of soluble, isolated ACC-Hex oligomers (ACC-Hex, 0.015% w/v), fibrilized ACC-Hex (0.03 % w/v), and ACC-Hex gels at 0.1 and 5 % w/v peptide **1**.

While the exact mechanism of charge transport in our ACC-Hex nanofibers remains unknown, our data establish that they are electronically conductive and suggest structure-property relationships that distinguish these nanofiber materials from other conduction paradigms in organic conductors. The conduction mechanism in ACC-Hex nanofibers is likely to be distinct from the delocalized transport observed in explicitly π-stacked bio-hybrid systems, such as the peptide nanostructures and hydrogels formed by peptide-small molecule conjugates[38,66–68] and unnatural aromatic amino acids,[69] because the large spacing and off-angle packing of aromatic side chains in ACC-Hex preclude π-stacking interactions.[49] In addition, the electrochemical gating results and the temperature-dependence of conductance of the ACC-Hex

nanofibers show that charge transport along the nanofibers is not facilitated by a series of redox events, as is the case in ferrocene-coupled diphenylalanine nanowires,[70] amyloid fiber-conjugated cytochromes,[71] or cytochrome hopping in appendages of some electrogenic anaerobes.[35] In the bipotentiostat setup, redox-mediated conduction is facilitated through current exchange at the reduction potentials of the redox-active compound, manifesting as current peaks.[28,52,53] The ACC-Hex nanofiber films, on the other hand, demonstrate ohmic, particle-like transport of charge carriers, which varies linearly with the source-drain potential and is devoid of characteristic redox peaks. This ohmic conduction is insensitive to environmental changes, showing little dependence on pH and ionic strength, demonstrating that neither π-stacking nor redox hopping – or other thermally activated mechanisms – are necessary to facilitate charge transport over micrometer-scale distances in these peptide nanofibers.

Studies of *G. sulfurreducens* pili suggest the importance of aromatic amino acids to conductivity, with some structure homology models implying the presence of π–stacking along the length of the pili,[29,43,44] and experimental data showing correlations between aromatic content and conductivity.[39–41] However, to our knowledge there is no direct, spectroscopic evidence of electronic delocalization due to π orbital overlap in pili materials to date, and our results suggest that π-stacking is not present in the peptide nanofibers and therefore may not be necessary for long-range conduction in amino acid-based materials. Similarities in the ohmic charge transport behavior, the lack of redox-mediated conduction, and metallic-like temperature dependence observed in both ACC-Hex nanofiber and pili suggest other common factors that may contribute to long-range conductivity. *G. sulfurreducens* pili and ACC-Hex nanofibers are rich in aromatic residues and both comprise of α-helical monomers arranged into ordered fibers. Supramolecular ordering alone may not be sufficient to support electrical conductivity, as Type IV pili from other bacteria, which are presumably homologous structures,[72] exhibit substantial variation between species ranging from non-conductive to more conductive than *G. sulfurreducens* pili.[28,73,74] Other ordered protein and peptide materials, such as amyloid-like fibers, show little[75,76] or no conductivity.[28] Nonetheless, the correlation between conductivity and long-range order in the comparison between α-helical peptide nanofibers and gels in the present study demonstrates a critical role for supramolecular structure in supporting charge transport in these materials, even in the absence of electronic delocalization. Evidence of long-range electronic transport in amino acid nanomaterials, lacking both π electron overlap and redox centers, represents a distinct structural paradigm for electronic conduction in organic electronics, and ongoing studies are underway to identify key sequence and structural features supporting charge transport mechanisms in peptide nanofibers.

5.4 CONCLUSION

The present study demonstrates long-range electronic transport in peptide materials lacking the extended conjugation and π-orbital overlap of conventional organic semiconductors and metals. The supramolecular structure of the peptide nanofibers in this study precludes π orbital overlap between aromatic amino acid side chains, suggesting a mechanism of conduction distinct from the band conduction of periodic, π-stacked organic materials. Electrochemical and temperature-dependent transport data indicate ohmic behavior of charge carriers in this system, which is unexpected in a large unit cell, biological material. Our findings indicate that the supramolecular order and α-helical building blocks of the peptide nanofibers are critical structural features supporting the observed electronic conductivity. These data demonstrate electronic transport in synthetic peptides materials, with sequence and structural motifs borrowed from naturally

conductive bacterial protein fibers, that strongly depends on secondary and quaternary structure. These peptide nanofibers, with their mutable sequence elements, represent a promising experimental platform for further study of structure-property relationships in conductive amino acid materials. Their biocompatible composition and defined surface chemistry hold potential for application as ideal, naturally inspired bioelectronics interface materials. The peptide building blocks of these fibers suggest they can be synthesized by recombinant expression and incorporated as multifunctional material components of the growing synthetic biology toolbox.

5.5 MATERIALS AND METHODS
Peptide Material Preparation
Peptide Nanofiber and Hydrogel Preparation: Peptide **1** was synthesized as described previously.[49] A peptide seeding stock solution was made by dissolving lyophilized peptide in sterile filtered 1X PBS (Fisher) to a final concentration of 200 μM. The sample was vortexed and sonicated for 30 s each, and then incubated for a week at 37 °C prior to use.

Lyophilized peptide was dissolved in sterile filtered 1X PBS to a final concentration of 100 μM. Peptide seeding stock solution was added to a final concentration of 0.5% v/v. The sample was vortexed and sonicated for 30 s each and incubated overnight at 37 °C prior to use. Fiber formation of peptide **1** was verified by atomic force microscopy (AFM) imaging as described below.

For hydrogel formation, lyophilized peptide was dissolved in sterile filtered 1X PBS at concentrations of 0.1%, 0.25%, 0.5%, and 5% w/v. Samples were vortexed and sonicated for 30 s each and incubated at 70 °C for 20 min to induce gelation.

Amyloid-β (Aβ) Fiber Formation: Aβ 1-40 peptide was purchased from Sigma Aldrich for Aβ fiber formation. Lyophilized peptide was dissolved in 150 mM phosphate buffered saline (PBS) to a concentration of 100μM and incubated at 37° C for two weeks to form fibers. Fiber formation of Aβ peptide was verified using AFM imaging.

Material Characterization
AFM Sample Preparation and Imaging of Peptide Fibers: AFM characterization of sample morphology was conducted on silicon wafer chips. Prior to sample deposition, wafer chips were sonicated for 5 min each in acetone, isopropanol, and ultrapure water, followed by drying under nitrogen. Peptide fiber samples were drop cast onto freshly cleaned wafers and allowed to sit on the substrate for 2 min, upon which excess moisture was removed from the edges of the sample using a Kimwipe. The sample was then briefly rinsed with ultrapure water to remove salts and dried under nitrogen. AFM images were collected with an Asylum MFP3D operating in tapping mode under ambient conditions. Scans were rastered at 0.5 Hz using iridium-coated silicon probes (Asylum Research ASYELEC-01) with a tip radius of 28 nm and a resonant frequency of 70 kHz.

Rheology of Peptide Materials: All rheological experiments were performed with an AR-G2 Rheometer (TA Instruments) in a parallel plate configuration ($d = 25$ mm) at 25 °C with a gap height of 350 μm. A solvent trap was used to prevent evaporation over the course of the measurements. The storage G' and loss moduli G'' of the hydrogels were acquired as a function of strain amplitude from 0.1 to 100 % at an oscillating frequency of 1 Hz to estimate linear viscoelastic regime for hydrogels.

Circular Dichroism of Peptide Materials: The conformation of peptide **1** in fibers and gels was characterized by circular dichroism (CD) spectroscopy, as described previously.[49] Hydrogels of peptide **1** were prepared at concentrations of 0.1%, 0.25%, and 5% w/v in 1X PBS buffer at pH 7.4. The 0.03% w/v sample of peptide **1** was prepared under typical fiber forming conditions (seeded and incubated overnight at 37 °C). A fresh sample of non-fibrilized peptide **1** (50 μM, 0.015% w/v) was also tested. CD spectra were recorded on a Jasco J-810 spectropolarimeter equipped with a Peltier thermoelectric temperature control device. The 5% w/v sample was deposited on a quartz slide as a thin film and the ellipticity was measured between 190-250 nm at 20 °C. All other samples of peptide **1** were prepared in a quartz cuvette with a 1 mm path length and measured over the same range of wavelengths at 20 °C. The voltage of the photomutiplier tube (PMT) was tracked during the course of the CD measurement and spectra are truncated at wavelengths at which the PMT voltage exceeded 500 V.

Electronic Property Characterization

Device Preparation: Interdigitated electrodes were used for all DC measurements. Each electrode was comprised of 100 parallel 5 μm x 2 mm long bands with an intra-band spacing of 5 μm. Devices were photolithographically patterned onto Pyrex wafers with 60 nm Au and a 5 nm Ti adhesion layer deposited by electron beam evaporation. Devices were sonicated in washes of acetone, isopropanol, and ultrapure water to prior to use. Devices were individually tested for shorts prior to sample deposition.

Solid-State I-V Measurements of Peptide Films: For sheet resistance comparisons, 6.9 μg of ACC-Hex fibers and Aβ fibers were respectively drop cast onto interdigitated electrodes. Film were dried under laminar flow and rinsed with ultrapure water to remove salts. *I-V* measurements were performed with a Keithley Model 2612B Source Measure Unit. Current was monitored as a function of swept voltage from +0.8V to -0.8V under ambient conditions.
The electrical conductivities of ACC-Hex fibers and hydrogel samples were compared as a function of weight percentage. 20 μL of ACC-Hex fibers in the fibrilization solution (seeded, 0.03% w/v) and 20 μL of 0.1%, 0.25%, 0.5%, and 5% hydrogels were deposited onto separate interdigitated electrode devices. After air dying under laminar flow, dried films were rinsed with ultrapure water to remove salts. *I-V* measurements were performed as described above.

Single Fiber Conductive AFM Measurements: Prior to fiber deposition, glass slides were sonicated in acetone, isopropanol, and ultrapure water and plasma cleaned. Fibers were drop-cast onto cleaned glass slides and allowed to dry. Samples were rinsed with ultrapure water to remove salts and dried under N2. Electrode contacts (2 nm of chromium and 80 nm gold) were thermally evaporated onto the glass slide using a shadow mask. The electrodes were shorted to a grounding plate using silver paint and conductive AFM was performed using an Asylum MFP3D in ORCA mode with iridium-coated silicon probes (Asylum Research ASYELEC-01).
 Scans were first done in contact and current mode with a 5 V bias to determine the position of the edge of the electrode. The scan was then repeated in tapping mode to obtain better resolution of the fiber. The tip of the conductive probe was then positioned at various distances along the fiber, allowing for a two-point measurement between the patterned electrode and the tip. The current response at each position of the nanofiber was monitored as the voltage was swept between ± 5 V. Individual nanofiber conductivities were calculated from the distance-

dependent conductance values and the using the peak height of the nanofibers as measured by AFM as the diameter and assuming a cylindrical conduction cross section. Controls were performed on the gold electrode and on the insulating substrate. Fiber conductivity was determined as an average of 4 different fiber samples.

Electrochemical Conductance Measurements: For solution-gated measurements, 22-gauge solid core insulated wire leads were connected to the interdigitated source and drain electrodes using conductive silver epoxy (MG Materials). Exposed electrode and lead connections were sealed with waterproof silicone sealant (DAP All-Purpose Adhesive Sealant). ACC-Hex fibers were drop cast onto cleaned electrodes to deposit a total peptide mass of 6.9 μg and were air dried in a laminar flow hood.

Solution gating measurements were conducted in 0.1M phosphate-citrate buffer, and the pH was controlled by changing the ratios of constituent sodium phosphate dibasic (Na_2HPO_4) and sodium citrate ($Na_2C_6H_6O_7$). For ionic strength measurements, 0.2 M Na_2HPO_4 and 0.2M $Na_2C_6H_6O_7$ stocks were prepared and diluted with ultrapure water to achieve the appropriate ionic strength. Electrolyte solutions were degassed with 80% N_2 with 20% CO_2 prior to electrochemical cell assembly in a 100 mL aqueous electrochemical cell (Adam & Chittenden MFC 100.25.3), which was sealed with rubber septa. Titanium wire and microfit connectors were used to connect the electrochemical components to external leads (DigiKey).

Bipotentiostat cyclic voltammograms (CVs) were performed using two Gamry potentiostats (series PC14/300) connected with a bipotentiosat cable. In the bipotentiostat setup, described previously,[28,53,77] the source and drain are monitored as two independent working electrodes, referenced to the same saturated Ag/AgCl reference and sharing the same platinum wire (Sigma Aldrich) as a counter electrode. The source electrode was swept from -0.8 V to +0.4 V with respect to Ag/AgCl, at a scan rate of 10 mV/s. Simultaneously, the drain was swept at a fixed source-drain offset V_{DS} relative to the source, with respect to Ag/AgCl, at a scan rate of 10 mV/s. The background catalytic current was determined by conducting bipotentiostat CVs at V_{DS} = 0, and the background values were subtracted from nonzero offsets to obtain the conducting current I_{con}. The difference currents between the source and the drain, divided by a factor of two, were plotted as I_{DS}.

Temperature-Dependent Electrical Conductance Measurements: To assess the temperature-dependent electrical conductance of ACC-Hex fiber films, electrochemical cells were submerged in a stirred water bath with a metal thermocouple. A hot plate was used to heat the system and ice was added to the water bath to achieve cooling. Once the thermocouple registered a stable bath temperature for several minutes at each temperature set point, bipotentiostat chronoamperometry measurements were performed, wherein the source and drain currents were independently monitored while maintaining a fixed V_{DS} offset. Once steady-state currents were stable for 1 min, the currents were averaged and the steady-state conducting current was taken to be half the difference between the source and drain currents, which mirror each other with opposite polarity. The negligible background current at V_{DS} =0V was subtracted from the steady-state current, which was then divided by V_{DS} to obtain the conductance. Measurements were taken with V_{DS} values of 0 V, 10 mV, 20 mV, 40 mV, 60 mV, 80 mV, -10 mV, -20 mV, -40 mV, -60 mV, and -80 mV and were performed in 0.1 M phosphate citrate buffer at pH 7.0. Each data point in Fig. 3B is an average of the 10 bias offset measurements conducted at a single temperature with error bars representing the standard error.

Electrical Impedance Spectroscopy Measurements: For electrical impedance spectroscopy, a sandwich electrode was fabricated from two 2 cm x 2 cm plates of fluorine-doped tin oxide (FTO) coated glass sides (Sigma Aldrich). External leads were attached to the non-conductive backsides of the glass slides using silver epoxy, and silver paste (Ted Pella) was used to connect the leads to the conductive FTO film. Two 540 μm non-conductive spacers were used to insulate the conductive paste and separate the slides, which were then sealed using electrical tape and silicone epoxy. EIS measurements were performed in a Faraday cage and spanning a frequency range of 10 mHz to 100 MHz, with a fixed DC bias of 0 V and an AC perturbation of 10 mV.

Molecular Dynamics Simulations of Peptide Self-Assembly

The coarse grained (CG) MARTINI force field [78,79] was used for biomolecular simulations to model peptides at different concentrations in explicit solvent. The MARTINI model uses a four-to-one mapping in which four atoms and associated hydrogen atoms are represented by one CG bead to represent protein backbone and side chains. Water and ions (which were added to electronically neutralize the system) are treated explicitly at the same level of coarse-graining. Although MARTINI lacks some atomic detail given its coarse-grained nature, its force field has been undergone extensive parameterization based on comparison with experimental results. Since MARTINI requires that the secondary structure of a peptide needs to be provided *a priori* and is fixed during the simulation, the helical conformation from the X-ray crystal structure of peptide **1** was used.[49]

All molecular dynamics (MD) simulations were performed with the GROMACS simulation package in the NPT ensemble. The pressure and temperature were maintained using the Berendsen method at 1 bar and at different constant temperatures, ranging from 330 to 350 K. Initially, the first set of 20 independent simulations were performed on a system containing 50 dipeptides that were placed randomly within a cubic box of 55 nm and solvated in standard MARTINI CG water and ions. Once isolated peptides came together to form the first hexamer, after 20 μs in effective simulation time, the hexamer was extracted for the next set of simulations. 40 copies of the hexamer were randomly placed within a cubic box of either 25 or 55 nm, containing water and ions, for another 20 μs MD simulation at 1 bar. This set of simulations was conducted at different temperatures ranging from 300 to 320 K; these lower temperatures allowed for stability of the hexameric copies. Hexamers in a larger box and thus at a lower concentration came together to form linear fibers, whereas those in a smaller box and at a higher concentration came together to form branched structures at different temperatures.

5.6 REFERENCES

(1) Nicolini, C. From Neural Chip and Engineered Biomolecules to Bioelectronic Devices: An Overview. *Biosens. Bioelectron.* **1995**, *10*, 105–127.

(2) Kaltenbrunner, M.; Sekitani, T.; Reeder, J.; Yokota, T.; Kuribara, K.; Tokuhara, T.; Drack, M.; Schwödiauer, R.; Graz, I.; Bauer-Gogonea, S.; Bauer, S.; Someya, T. An Ultra-Lightweight Design for Imperceptible Plastic Electronics. *Nature* **2013**, *499*, 458–463.

(3) Lee, H.; Choi, T. K.; Lee, Y. B.; Cho, H. R.; Ghaffari, R.; Wang, L.; Choi, H. J.; Chung, T. D.; Lu, N.; Hyeon, T.; Choi, S.H.; Kim, D-H. A Graphene-Based Electrochemical Device with Thermoresponsive Microneedles for Diabetes Monitoring and Therapy. *Nat. Nanotechnol.* **2016**, *11*, 566–572.

(4) Liu, H.; Zhao, T.; Jiang, W.; Jia, R.; Niu, D.; Qiu, G.; Fan, L.; Li, X.; Liu, W.; Chen, B.; Shi, Y.; Yin, L.; Lu, B. Flexible Battery-Less Bioelectronic Implants: Wireless Powering and Manipulation by near-Infrared Light. *Adv. Funct. Mater.* **2015**, *25*, 7071–7079

(5) Jonsson, A.; Song, Z.; Nilsson, D.; Meyerson, B. A.; Simon, D. T.; Linderoth, B.; Berggren, M. Therapy Using Implanted Organic Bioelectronics. *Sci. Adv.* **2015**, *1*, 1–6.

(6) Luz, R. A. S.; Pereira, A. R.; de Souza, J. C. P.; Sales, F. C. P. F.; Crespilho, F. N. Enzyme Biofuel Cells: Thermodynamics, Kinetics and Challenges in Applicability. *ChemElectroChem* **2014**, *1*, 1751–1777.

(7) Slaughter, G.; Kulkarni, T. Highly Selective and Sensitive Self-Powered Glucose Sensor Based on Capacitor Circuit. *Sci. Rep.* **2017**, *7*, 1471.

(8) Falk, M.; Alcalde, M.; Bartlett, P. N.; De Lacey, A. L.; Gorton, L.; Gutierrez-Sanchez, C.; Haddad, R.; Kilburn, J.; Leech, D.; Ludwig, R.; Magner, E.; Mate, D.M.; Conghaile, P.Ó.; Ortiz, R.; Pita, M.; Pöller, S.; Ruzgas, T.; Salaj-Kosla, U.; Schuhmann, W.; Sebelius, F.; *et al*. Self-Powered Wireless Carbohydrate/Oxygen Sensitive Biodevice Based on Radio Signal Transmission. *PloS One* **2014**, *9*, e109104.

(9) Lafleur, J. P.; Jönsson, A.; Senkbeil, S.; Kutter, J. P. Recent Advances in Lab-on-a-Chip for Biosensing Applications. *Biosens. Bioelectron.* **2016**, *76*, 213–233.

(10) Medina-Sánchez, M.; Miserere, S.; Merkoçi, A. Nanomaterials and Lab-on-a-Chip Technologies. *Lab Chip* **2012**, *12*, 1932–1943.

(11) Liu, J.; Fu, T.-M.; Cheng, Z.; Hong, G.; Zhou, T.; Jin, L.; Duvvuri, M.; Jiang, Z.; Kruskal, P.; Xie, C.; Suo, Z.; Fang; Y.; Lieber, C.M. Syringe-Injectable Electronics. *Nat. Nanotechnol.* **2015**, *10*, 629–636.

(12) Oxley, T. J.; Opie, N. L.; John, S. E.; Rind, G. S.; Ronayne, S. M.; Wheeler, T. L.; Judy, J. W.; McDonald, A. J.; Dornom, A.; Lovell, T. J. H.; Steward, C.; Garrett, D.J.; Moffat, B.A.; Lui, E.H.; Yassi, N.; Campbell, B.C.V.; Wong, Y.T.; Fox, K.E.; Nurse, E.S.; Bennett, I.E.; *et al.* Minimally Invasive Endovascular Stent-Electrode Array for High-Fidelity, Chronic Recordings of Cortical Neural Activity. *Nat. Biotechnol.* **2016**, *34*, 320–327.

(13) Someya, T.; Bao, Z.; Malliaras, G. G. The Rise of Plastic Bioelectronics. *Nature* **2016**, *540*, 379–385.

(14) Zhang, A.; Lieber, C. M. Nano-Bioelectronics. *Chem. Rev.* **2016**, *116*, 215–257.

(15) Domigan, L. J. Proteins and Peptides as Biological Nanowires: Towards Biosensing Devices. *Methods Mol. Biol. Clifton NJ* **2013**, *996*, 131–152.

(16) Eakins, G. L.; Pandey, R.; Wojciechowski, J. P.; Zheng, H. Y.; Webb, J. E. A.; Valéry, C.; Thordarson, P.; Plank, N. O. V.; Gerrard, J. A.; Hodgkiss, J. M. Functional Organic Semiconductors Assembled *via* Natural Aggregating Peptides. *Adv. Funct. Mater.* **2015**, *25*, 5640–5649.

(17) Kasai, S.; Ohga, Y.; Mochizuki, M.; Nishi, N.; Kadoya, Y.; Nomizu, M. Multifunctional Peptide Fibrils for Biomedical Materials. *Biopolymers* **2004**, *76*, 27–33.

(18) Hauser, C. A. E.; Zhang, S. Designer Self-Assembling Peptide Nanofiber Biological Materials. *Chem. Soc. Rev.* **2010**, *39*, 2780–2790.

(19) Santis, E. D.; Ryadnov, M. G. Peptide Self-Assembly for Nanomaterials: The Old New Kid on the Block. *Chem. Soc. Rev.* **2015**, *44*, 8288–8300.

(20) Bai, Y.; Luo, Q.; Liu, J. Protein Self-Assembly *via* Supramolecular Strategies. *Chem. Soc. Rev.* **2016**, *45*, 2756–2767.

(21) Liu, J.; Xie, C.; Dai, X.; Jin, L.; Zhou, W.; Lieber, C. M. Multifunctional Three-Dimensional Macroporous Nanoelectronic Networks for Smart Materials. *Proc. Natl. Acad. Sci. U. S. A.* **2013**, *110*, 6694–6699.

(22) Gray, H. B.; Winkler, J. R. Long-Range Electron Transfer. *Proc. Natl. Acad. Sci. U. S. A.* **2005**, *102*, 3534–3539.

(23) Winkler, J. R.; Gray, H. B. Long-Range Electron Tunneling. *J. Am. Chem. Soc.* **2014**, *136*, 2930–2939.

(24) Sepunaru, L.; Refaely-Abramson, S.; Lovrinčić, R.; Gavrilov, Y.; Agrawal, P.; Levy, Y.; Kronik, L.; Pecht, I.; Sheves, M.; Cahen, D. Electronic Transport *via* Homopeptides: The Role of Side Chains and Secondary Structure. *J. Am. Chem. Soc.* **2015**, *137*, 9617–9626.

(25) Amdursky, N. Electron Transfer across Helical Peptides. *ChemPlusChem* **2015**, *80*, 1075–1095.

(26) Juhaniewicz, J.; Pawlowski, J.; Sek, S. Electron Transport Mediated by Peptides Immobilized on Surfaces. *Isr. J. Chem.* **2015**, *55*, 645–660.

(27) Malvankar, N. S.; Vargas, M.; Nevin, K. P.; Franks, A. E.; Leang, C.; Kim, B.-C.; Inoue, K.; Mester, T.; Covalla, S. F.; Johnson, J. P.; Rotello, V.M.; Lovley, D.L. Tunable Metallic-like Conductivity in Microbial Nanowire Networks. *Nat. Nanotechnol.* **2011**, *6*, 573–579.

(28) Ing, N. L.; Nusca, T. D.; Hochbaum, A. I. Geobacter Sulfurreducens Pili Support Ohmic Electronic Conduction in Aqueous Solution. *Phys. Chem. Chem. Phys.* **2017**, *19*, 21791–21799.

(29) Malvankar, N. S.; Vargas, M.; Nevin, K.; Tremblay, P.-L.; Evans-Lutterodt, K.; Nykypanchuk, D.; Martz, E.; Tuominen, M. T.; Lovley, D. R. Structural Basis for Metallic-like Conductivity in Microbial Nanowires. *mBio* **2015**, *6*, e00084-15.

(30) Reguera, G.; McCarthy, K. D.; Mehta, T.; Nicoll, J. S.; Tuominen, M. T.; Lovley, D. R. Extracellular Electron Transfer *via* Microbial Nanowires. *Nature* **2005**, *435*, 1098–1101.

(31) Adhikari, R. Y.; Malvankar, N. S.; Tuominen, M. T.; Lovley, D. R. Conductivity of Individual Geobacter Pili. *RSC Adv.* **2016**, *6*, 8354–8357.

(32) Amdursky, N.; Marchak, D.; Sepunaru, L.; Pecht, I.; Sheves, M.; Cahen, D. Electronic Transport *via* Proteins. *Adv. Mater.* **2014**, *26*, 7142–7161.

(33) Mercato, L. L. del; Pompa, P. P.; Maruccio, G.; Torre, A. D.; Sabella, S.; Tamburro, A. M.; Cingolani, R.; Rinaldi, R. Charge Transport and Intrinsic Fluorescence in Amyloid-like Fibrils. *Proc. Natl. Acad. Sci.* **2007**, *104*, 18019–18024.

(34) Creasey, R. C. G.; Shingaya, Y.; Nakayama, T. Improved Electrical Conductance through Self-Assembly of Bioinspired Peptides into Nanoscale Fibers. *Mater. Chem. Phys.* **2015**, *158*, 52–59.

(35) Pirbadian, S.; Barchinger, S. E.; Leung, K. M.; Byun, H. S.; Jangir, Y.; Bouhenni, R. A.; Reed, S. B.; Romine, M. F.; Saffarini, D. A.; Shi, L.; Gorby, Y.A.; Golbeck, J.H.; El-Naggar, M.Y. Shewanella Oneidensis MR-1 Nanowires Are Outer Membrane and Periplasmic Extensions of the Extracellular Electron Transport Components. *Proc. Natl. Acad. Sci.* **2014**, *111*, 12883–12888.

(36) Malvankar, N. S.; Tuominen, M. T.; Lovley, D. R. Lack of Cytochrome Involvement in Long-Range Electron Transport through Conductive Biofilms and Nanowires of Geobacter Sulfurreducens. *Energy Environ. Sci.* **2012**, *5*, 8651.

(37) Wall, B. D.; Zacca, A. E.; Sanders, A. M.; Wilson, W. L.; Ferguson, A. L.; Tovar, J. D. Supramolecular Polymorphism: Tunable Electronic Interactions within π-Conjugated Peptide Nanostructures Dictated by Primary Amino Acid Sequence. *Langmuir* **2014**, *30*, 5946–5956.

(38) Nalluri, S. K. M.; Shivarova, N.; Kanibolotsky, A. L.; Zelzer, M.; Gupta, S.; Frederix, P. W. J. M.; Skabara, P. J.; Gleskova, H.; Ulijn, R. V. Conducting Nanofibers and Organogels Derived from the Self-Assembly of Tetrathiafulvalene-Appended Dipeptides. *Langmuir* **2014**, *30*, 12429–12437.

(39) Malvankar, N. S.; Yalcin, S. E.; Tuominen, M. T.; Lovley, D. R. Visualization of Charge Propagation along Individual Pili Proteins Using Ambient Electrostatic Force Microscopy. *Nat. Nanotechnol.* **2014**, *9*, 1012–1017.

(40) Tan, Y.; Adhikari, R. Y.; Malvankar, N. S.; Pi, S.; Ward, J. E.; Woodard, T. L.; Nevin, K. P.; Xia, Q.; Tuominen, M. T.; Lovley, D. R. Synthetic Biological Protein Nanowires with High Conductivity. *Small* **2016**, *12*, 4481–4485.

(41) Vargas, M.; Malvankar, N. S.; Tremblay, P.-L.; Leang, C.; Smith, J. A.; Patel, P.; Synoeyenbos-West, O.; Nevin, K. P.; Lovley, D. R. Aromatic Amino Acids Required for Pili Conductivity and Long-Range Extracellular Electron Transport in Geobacter Sulfurreducens. *mBio* **2013**, *4*, e00105–e00113.

(42) Tan, Y.; Adhikari, R. Y.; Malvankar, N. S.; Ward, J. E.; Woodard, T. L.; Nevin, K. P.; Lovley, D. R. Expressing the Geobacter Metallireducens PilA in Geobacter Sulfurreducens Yields Pili with Exceptional Conductivity. *mBio* **2017**, *8*, e02203-16.

(43) Feliciano, G. T.; da Silva, A. J. R.; Reguera, G.; Artacho, E. Molecular and Electronic Structure of the Peptide Subunit of Geobacter Sulfurreducens Conductive Pili from First Principles. *J. Phys. Chem. A* **2012**, *116*, 8023–8030.

(44) Xiao, K.; Malvankar, N. S.; Shu, C.; Martz, E.; Lovley, D. R.; Sun, X. Low Energy Atomic Models Suggesting a Pilus Structure That Could Account for Electrical Conductivity of Geobacter Sulfurreducens Pili. *Sci. Rep.* **2016**, *6*, 23385.

(45) Pawlowski, J.; Juhaniewicz, J.; Tymecka, D.; Sek, S. Electron Transfer across α-Helical Peptide Monolayers: Importance of Interchain Coupling. *Langmuir* **2012**, *28*, 17287–17294.

(46) Atanassov, A.; Hendler, Z.; Berkovich, I.; Ashkenasy, G.; Ashkenasy, N. Force Modulated Conductance of Artificial Coiled-Coil Protein Monolayers. *Pept. Sci.* **2013**, *100*, 93–99.

(47) Morita, T.; Kimura, S. Long-Range Electron Transfer over 4 Nm Governed by an Inelastic Hopping Mechanism in Self-Assembled Monolayers of Helical Peptides. *J. Am. Chem. Soc.* **2003**, *125*, 8732–8733.

(48) Mizrahi, M.; Zakrassov, A.; Lerner-Yardeni, J.; Ashkenasy, N. Charge Transport in Vertically Aligned, Self-Assembled Peptide Nanotube Junctions. *Nanoscale* **2012**, *4*, 518–524.

(49) Spencer, R. K.; Hochbaum, A. I. X-Ray Crystallographic Structure and Solution Behavior of an Antiparallel Coiled-Coil Hexamer Formed by *de Novo* Peptides. *Biochem.* **2016**, *55*, 3214–3223.

(50) Spencer, R. K.; Hochbaum, A. I. The Phe-Ile Zipper: A Specific Interaction Motif Drives Antiparallel Coiled-Coil Hexamer Formation. *Biochem.* **2017**, *56*, 5300–5308.

(51) Lührs, T.; Ritter, C.; Adrian, M; Riek-Loher, D; Bohrmann, B.; Döbeli, H.; Schubert, D.; Riek, R.; 3D Structure Alzheimer's Amyloid-b(1-42) Fibrils. *Proc. Natl. Acad. Sci. USA* **2005**, *102*, 17342–17347.

(52) Yates, M. D.; Strycharz-Glaven, S. M.; Golden, J. P.; Roy, J.; Tsoi, S.; Erickson, J. S.; El-Naggar, M. Y.; Barton, S. C.; Tender, L. M. Measuring Conductivity of Living Geobacter Sulfurreducens Biofilms. *Nat. Nanotechnol.* **2016**, *11*, 910–913.

(53) Yates, M. D.; Golden, J. P.; Roy, J.; Strycharz-Glaven, S. M.; Tsoi, S.; Erickson, J. S.; El-Naggar, M. Y.; Barton, S. C.; Tender, L. M. Thermally Activated Long Range Electron Transport in Living Biofilms. *Phys. Chem. Chem. Phys.* **2015**, *17*, 32564–32570.

(54) Yan, C.; Pochan, D. J. Rheological Properties of Peptide-Based Hydrogels for Biomedical and Other Applications. *Chem. Soc. Rev.* **2010**, *39*, 3528–3540.

(55) Lyon, L. A.; Serpe, M. J. *Hydrogel Micro and Nanoparticles*; John Wiley & Sons, 2012.

(56) MacKintosh, F. C. Elasticity of Semiflexible Biopolymer Networks. *Phys. Rev. Lett.* **1995**, *75*, 4425–4428.

(57) Hinner, B. Entanglement, Elasticity, and Viscous Relaxation of Actin Solutions. *Phys. Rev. Lett.* **1998**, *81*, 2614–2617.

(58) Colby, R. H. Structure and Linear Viscoelasticity of Flexible Polymer Solutions: Comparison of Polyelectrolyte and Neutral Polymer Solutions. *Rheol. Acta* **2010**, *49*, 425–442.

(59) Rahman, A. R. A.; Justin, G.; Guiseppi-Elie, A. Bioactive Hydrogel Layers on Microdisk Electrode Arrays: Impedimetric Characterization and Equivalent Circuit Modeling. *Electroanalysis* **2009**, *21*, 1135–1144.

(60) Amirudin, A.; Thieny, D. Application of Electrochemical Impedance Spectroscopy to Study the Degradation of Polymer-Coated Metals. *Prog. Org. Coat.* **1995**, *26*, 1–28.

(61) Greenfield, N. J. Using Circular Dichroism Spectra to Estimate Protein Secondary Structure. *Nat. Protoc.* **2006**, *1*, 2876–2890.

(62) Pandya, M. J.; Spooner, G. M.; Sunde, M.; Thorpe, J. R.; Rodger, A.; Woolfson, D. N. Sticky-End Assembly of a Designed Peptide Fiber Provides Insight into Protein Fibrillogenesis. *Biochem.* **2000**, *39*, 8728–8734.

(63) Bromley, E. H. C.; Channon, K. J.; King, P. J. S.; Mahmoud, Z. N.; Banwell, E. F.; Butler, M. F.; Crump, M. P.; Dafforn, T. R.; Hicks, M. R.; Hirst, J. D.; Rodger, A.; Woolfson, D.N. Assembly Pathway of a Designed Alpha-Helical Protein Fiber. *Biophys. J.* **2010**, *98*, 1668–1676.

(64) Frost, D. W. H.; Yip, C. M.; Chakrabartty, A. Reversible Assembly of Helical Filaments by *de Novo* Designed Minimalist Peptides. *Biopolymers* **2005**, *80*, 26–33.

(65) Chin, D.-H.; Woody, R. W.; Rohl, C. A.; Baldwin, R. L. Circular Dichroism Spectra of Short, Fixed-Nucleus Alanine Helices. *Proc. Natl. Acad. Sci.* **2002**, *99*, 15416–15421.

(66) Xu, H.; Das, A. K.; Horie, M.; Shaik, M. S.; Smith, A. M.; Luo, Y.; Lu, X.; Collins, R.; Liem, S. Y.; Song, A.; Popelier, P.L.A.; Turner, M.L.; Xiao, P. Kinloch, I.A.; Ulijn, R.V. An Investigation of the Conductivity of Peptide Nanotube Networks Prepared by Enzyme-Triggered Self-Assembly. *Nanoscale* **2010**, *2*, 960–966.

(67) Ardoña, H. A. M.; Tovar, J. D. Peptide π-Electron Conjugates: Organic Electronics for Biology? *Bioconjug. Chem.* **2015**, *26*, 2290–2302.

(68) Ardoña, H. A. M.; Besar, K.; Togninalli, M.; Katz, H. E.; Tovar, J. D. Sequence-Dependent Mechanical, Photophysical and Electrical Properties of Pi-Conjugated Peptide Hydrogelators. *J. Mater. Chem. C* **2015**, *3*, 6505–6514.

(69) Ashkenasy, N.; Horne, W. S.; Reza Ghadiri, M. Design of Self-Assembling Peptide Nanotubes with Delocalized Electronic States. *Small* **2006**, *2*, 99–102.

(70) Wang, J.; Li, D.; Yang, M.; Zhang, Y. A Novel Ferrocene-Tagged Peptide Nanowire for Enhanced Electrochemical Glucose Biosensing. *Anal. Methods* **2014**, *6*, 7161–7165.

(71) Altamura, L.; Horvath, C.; Rengaraj, S.; Rongier, A.; Elouarzaki, K.; Gondran, C.; Maçon, A. L. B.; Vendrely, C.; Bouchiat, V.; Fontecave, M.; Mariolle, D.; Rannou, P.; Le Goff, A.; Duraffourg, N.; Holzinger, M.; Forge, V. A Synthetic Redox Biofilm Made from Metalloprotein–prion Domain Chimera Nanowires. *Nat. Chem.* **2017**, *9*, 157–163.

(72) Giltner, C. L.; Nguyen, Y.; Burrows, L. L. Type IV Pilin Proteins: Versatile Molecular Modules. *Microbiol. Mol. Biol. Rev. MMBR* **2012**, *76*, 740–772.

(73) Lampa-Pastirk, S.; Veazey, J. P.; Walsh, K. A.; Feliciano, G. T.; Steidl, R. J.; Tessmer, S. H.; Reguera, G. Thermally Activated Charge Transport in Microbial Protein Nanowires. *Sci. Rep.* **2016**, *6*, 23517.

(74) Walker, D. J.; Adhikari, R. Y.; Holmes, D. E.; Ward, J. E.; Woodard, T. L.; Nevin, K. P.; Lovley, D. R. Electrically Conductive Pili from Pilin Genes of Phylogenetically Diverse Microorganisms. *ISME J.* **2017**.

(75) Amit, M.; Cheng, G.; Hamley, I. W.; Ashkenasy, N. Conductance of Amyloid β Based Peptide Filaments: Structure–function Relations. *Soft Matter* **2012**, *8*, 8690–8696.

(76) Kalyoncu, E.; Ahan, R. E.; Olmez, T. T.; Seker, U. O. S. Genetically Encoded Conductive Protein Nanofibers Secreted by Engineered Cells. *RSC Adv.* **2017**, *7*, 32543–32551.

(77) Snider, R. M.; Strycharz-Glaven, S. M.; Tsoi, S. D.; Erickson, J. S.; Tender, L. M. Long-Range Electron Transport in Geobacter Sulfurreducens Biofilms Is Redox Gradient-Driven. *Proc. Natl. Acad. Sci.* **2012**, *109*, 15467–15472.

(78) Marrink, S. J.; Risselada, H. J.; Yefimov, S.; Tieleman, D. P.; de Vries, A. H. The MARTINI Force Field: Coarse Grained Model for Biomolecular Simulations. *J. Phys. Chem. B* **2007**, *111*, 7812–7824.

(79) Monticelli, L.; Kandasamy, S. K.; Periole, X.; Larson, R. G.; Tieleman, D. P.; Marrink, S.-J. The MARTINI Coarse-Grained Force Field: Extension to Proteins. *J. Chem. Theory Comput.* **2008**, *4*, 819–834.

CHAPTER 6

Enzymatic Electrocatalysis on Conductive Peptide Scaffolds

6.1 SUMMARY

Peptide materials may be a promising scaffold for enzyme immobilization; however the non-conductive nature of most peptide and protein materials limits their utilization in electrocatalysis setups requiring direct electron transfer. Here we demonstrate that conductive peptide nanofibers, known as ACC-Hex, are capable of facilitating direct electron transfer to immobilized enzyme. We use cyclic voltammetry and electrical impedance spectroscopy to show that these electronically-conductive peptide fibers can enhance the electroactive surface area of glassy carbon electrodes and participate in single and multi-electron transfer processes. We also demonstrate that ACC-Hex fibers are capable of achieving direct electron transfer with laccase enzyme immobilized on the fiber surface. Furthermore, laccase immobilized on ACC-Hex can form a third generation electrochemical sensor, capable of detecting catechol with a minimum detection limit of ~5 μM. Our results demonstrate that peptide materials can be compatible scaffolds for enzyme immobilization and are capable of achieving direct electronic communication with the enzyme active site. This posits the possibility of bioelectrodes and biosensors composed entirely of biological components.

6.2 INTRODUCTION

Enzymes are highly efficient catalysts for a variety of chemical processes. They can achieve higher substrate and product specificities than conventional catalysts, reducing the amount of unwanted side reactions and processing steps associated with compound synthesis. Enzymatically synthesized products can be utilized in a wide range of sectors, such as energy[1–3], pharmaceuticals[4,5], and food production[6]. Beyond electrocatalysis, enzymes can also be useful for sensing applications[7,8]. Their highly selective affinity for specific biomarkers make them excellent biosensor components for disease detection[9,10]. They can also aid in environmental remediation by not only detecting pollutants but electrocatalytically degrading those compounds into non-polluting components[11].

Attaching enzymes to compatible solid supports enhances their stability and reusability. Immobilization can provide resistance to environmental factors such as solvent environment, temperature, and pH, which would otherwise denature unbound enzyme[12,13]. Additionally, immobilization can enhance reaction kinetics and allows for easier product or analyte separation, which in turn enhances the enzyme reusability. Some immobilization strategies retain certain enzymatic functions in organic solvent[14,15], allowing for more seamless integration of biocatalytic steps with upstream and downstream synthetic chemistry processes.

Nevertheless, selecting the immobilization material is not trivial, as the properties of the immobilized enzyme are dictated by the interaction between the enzyme and the support [16]. Although there is no universal support system for all enzymes and applications, peptides and proteins have several ideal attributes as immobilization substrates. Peptides and proteins can participate a variety of sequence-dependent covalent and noncovalent chemical modifications for enzyme attachment, using amino acids with orthogonal bioconjugate chemistries such as cysteines and lysines[17]. Sequences can also be screened and optimized for specific enzymatic interactions[18], using well-established methods for high yield and combinatorial synthesis[19,20].

Peptides and proteins are capable of self-assembling into a variety of high aspect ratio nanostructures[21–23], whose geometries can be selected for based on the enzyme and application[24]. Physical entrapment within a gel matrix offers stabilization without chemical modifications to the enzyme, minimizing changes to the enzyme structure[25]. Conversely, if functionality can be improved by increasing the rigidity of the structure, covalent immobilization via multiple points of contact may enhance enzymatic performance, and fiber meshes or nanotubes with large internal surface areas may be preferable[26]. Furthermore, solid binding peptides can be incorporated into enzymatic sequences to promote binding and enzymatic function at organic and inorganic interfaces[27,28].

Additionally, several groups have shown that incorporating amino- or amino acid-terminated monolayers in enzyme immobilization strategies may help support direct electron transfer (DET) between the enzyme and electrode surface through favorable interactions with or around the active site of the enzyme[29–31]. DET eliminates the need for an electron mediator to shuttle electrons between the electrode and enzyme[32], removing the diffusion limitations associated with mediator-based transport and enhancing the kinetics of the system[33]. DET also reduces the electrochemical potential electrocatalytic activity, bringing it closer to redox potential of the enzyme itself and reducing the likelihood of unwanted side reactions in the process[34]. In order for DET to occur, the scaffold must be conductive, retain functionality of the immobilized enzyme, and position the active site of the enzyme, which is typically deeply buried[32], in close enough proximity to support fast electron transfer to the electrode. Although peptide and protein interfaces can help maintain enzyme functionality and structure[35,36], their largely insulating nature limits their applications in DET arrangements to short-sequence monolayer coatings[29,37], requires recombinant expression of the linkage near the active site[31,37,38], or requires the incorporation of a conductive element, such as carbon nanotubes[26] or metals[39].

Recently, we developed a *de novo* peptide which self-assembles into electronically-conductive nanofibers[40]. In the present study, we show that these conductive peptide nanofibers are promising scaffolds for immobilized enzyme electrocatalysis. The nanofibers conduct electronic charge with negligible contribution from ion-coupled transport mechanisms, and films of the nanofibers substantially increase the electroactive surface area of electrochemical electrodes with little effect on redox reaction reversibility. These peptides exhibit promising properties as enzyme scaffolds, as demonstrated by reversible electrocatalytic reactions of catechol oxidation and 1,2-benzoquinone reduction via immobilized laccase.

6.3 RESULTS AND DISCUSSION
6.3.1 Electronic Conductivity in Aqueous Salt Solutions:
While ACC-Hex nanofiber conductivity was previously demonstrated to be robust over a variety of pH and ionic strength conditions, the possibility of proton- or ion-mediated transport had not yet been ruled out. Here, electrical impedance spectroscopy (EIS) measurements of ACC-Hex nanofibers in different electrolyte environments was used to quantify the contribution of various counterions to electronic conductivity (Fig. 1).ACC-Hex nanofibers were assembled from a bioinspired *de novo* peptide sequence, as previously described[40]. These nanofibers were cast into films on interdigitated devices to test for an ionic contribution to conduction to determine if their properties in a biosensing configuration would be sensitive to environmental conditions. Circuit modeling of the impedance signal allows for a determination of the capacitive, inductive, and resistive processes occurring across the cell. Charge transport through a network of ACC-Hex nanofibers bridging two electrodes can be modeled as a Randles circuit (Fig. 1 *inset*), where R_{CT}

represents the ionic conductivity of the electrolyte solution, R_{CT} represents the electron charge transfer resistance, and C_{dl} is the double layer capacitance. These elements can be identified on a Nyquist plot (Fig. 1B) of the data, where impedance is plotted as a function of imaginary Z"(ω) versus real Z'(ω) components. R_{CT} represents the diameter of the semicircle. Measurements were taken between the source and drain electrodes so that R_{CT} would correspond to charge transfer through the fiber network.
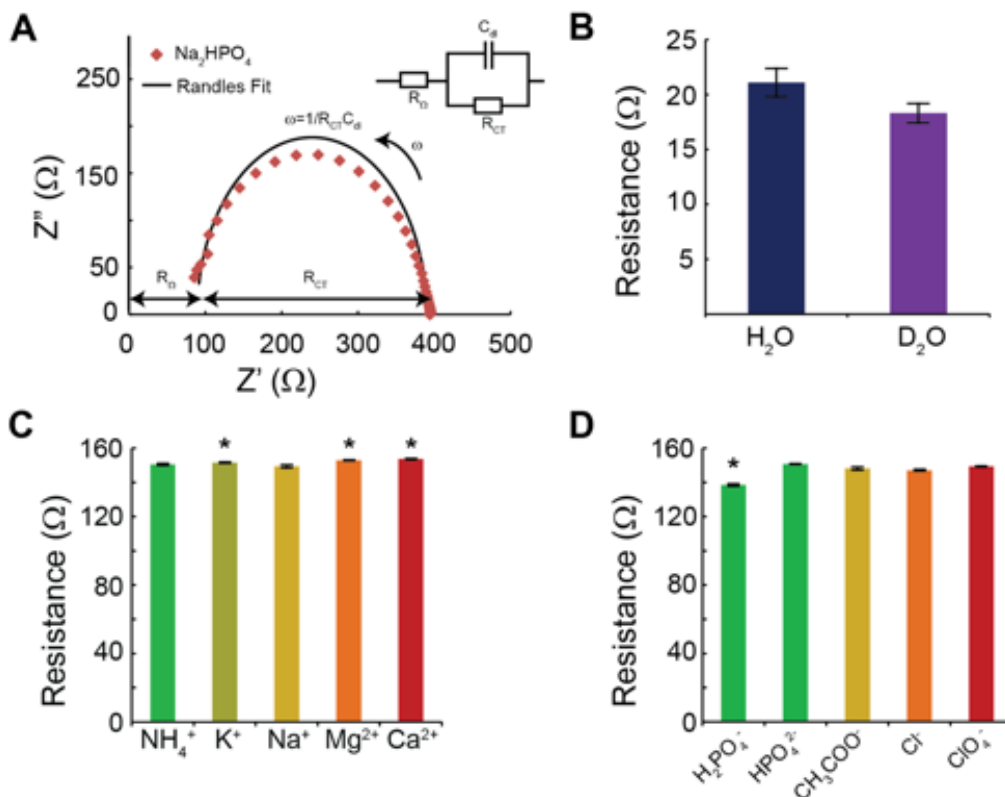
Figure 1: (A) Representative Nyquist spectra of impedance through ACC-Hex nanofiber films in 0.1M Na_2HPO_4 (dashed trace) with a Randles circuit model (inset) fit (solid trace). R_{CT} and R_s can be obtained through model fitting. (B) Impedance of ACC-Hex nanofiber films in H_2O and D_2O (n=5 measurements), determined from Randles circuit fitting of Nyquist impedance spectra. Impedance of ACC-Hex nanofiber films in (C) 0.1 M cation solutions with Cl^- as the counterion and (D) 0.1 M anion solutions with Na^+ as the counterion (n=8 measurements). Film resistances in K^+, Mg^{2+}, and Ca^{2+} have p-values of 0.08, 0.016, and 0.028, respectively, with respect to Na^+(NaCl). Film resistance in $H_2PO_4^-$ has a p-value of 0.0002 with respect to Cl^- (NaCl). Hofmeister ions are arranged in order of structure-ordering (green) to structure disordering (red).

To test for proton conductivity, the resistance of nanofiber films was compared in ultrapure water and D_2O solutions (Fig. 1A). If protons were facilitating transport, the change to a heavier isotope should slow charge transport kinetics and thus increase the measured impedance. However, the average impedance was slightly lower, though not statistically significantly so, in D_2O than in water and therefore indicates a lack of involvement of protons in the transport mechanism. To assess the potential contribution of other lyotropic effects, the nanofiber film impedance was measured in 0.1M solutions of Hofmeister series ions (Fig. 1C). The Hofmeister series[41,42] ranks anions and cations based on their ability to stabilize (or destabilize) protein structure, based on an empirical and qualitative ranking of precipitation effects on egg white proteins. It correlates with

the kosmotropic (enhances the hydrogen bonding of water) and chaotropic (disrupts the hydrogen bonding of water) classification of ions[43], such that chaotropic cations and kosmotropic anions stabilize protein structure, while kosmotropic cations and chaotropic anions destabilize protein structure. The small changes in resistance and lack of clear trends between Hofmeister ranking and film impedance suggests that the electrolyte does not participate in charge transfer. This observation was also consistent at lower ionic strengths. Although many biological redox charge transport chains involve proton or ion-coupled electron transfer, these findings suggest that charge conduction through the fibers is purely electronic. This is consistent with previous electrochemical, temperature dependence, and pH studies[40] suggesting that conduction through the fibers is not redox-mediated and supports a band-like mechanism of charge transport.

6.3.2 Electrochemical Behavior of ACC-Hex Nanofibers:

ACC-Hex nanofibers were dried onto GCEs to test for their ability to enhance the electroactive surface area via transferring the reversible single electron oxidation and reduction of 1mM methylviolagen (MV) according to the following reaction:

$$MV^{2+} + e^- \leftrightarrow MV^{+\cdot} \qquad \text{(Eq. 1)}$$

Larger oxidation and reduction peaks were observed with increasing number of sequential deposition of ACC-Hex from solution, relative to bare, unmodified GCE (Fig. 2). Based on the Randles-Sevcik equation, the peak currents can be used to estimate the change in electroactive surface area upon ACC-Hex fiber deposition:

$$i_p = 0.4463nFAC\left(\frac{nFvD}{RT}\right)^{1/2} \qquad \text{(Eq. 2)}$$

Here is i_p the peak current, n is the number of electrons transferred in the redox event (n=1), F is the Faraday constant, A is the electrode area (cm^2), C is the concentration of redox species, v is the scan rate, D is the diffusion coefficient, R is the gas constant, and T is temperature. Assuming all other values constant, the change in i_p (Fig. 2A) indicates that the electroactive surface area increased by 72.9%, 80.9%, and 97.4% relative to the unmodified GCE upon deposition of 40, 80, and 160 μL ACC-Hex fibers, respectively (the increase with drying of 160 μL of PBS on the GCE was 13.5%). The peak currents are also proportional to the square root of scan rate, consistent with a fast, reversible, and diffusion-limited redox process (Fig. 2B). These findings suggest that ACC-Hex enhances the electroactive surface area of GCE with a negligible change in electron transfer kinetics.

To analyze charge transfer from the electrode interface to redox species in solution, electrical impedance spectroscopy (EIS) was conducted in three-electrode mode, using a Ag/AgCl reference electrode, a Pt wire counter electrode, and 10 mM [Fe(CN)$_6$]$^{3-/4-}$ (1:1) as a redox probe (Fig. 3). In this setup, the resistance and capacitive elements can be modeled as a modified Randles circuit, where R_{CT}, R_Ω, and C_{dl} still compose the semicircle in the Nyquist plot, but with an additional element, the Warburg impedance, Z_w, which manifests as a linear tail on the Nyquist plot and is associated with a diffusion limited electron-transfer process. For semi-infinite (unrestricted) linear diffusion, the slope of the Warburg tail is 1. The ACC-Hex modified GCE has a significantly smaller semicircle than the unmodified electrode, confirming the increase in the electroactive surface area observed in the MV redox experiment. Additionally, the Warburg tail of the modified electrode exhibited a near unity slope of 0.998 (R^2 = 0.9997), compared to the slope of the unmodified electrode, with a slope of 0.559 (R^2 = 0.9997). This enhanced diffusion process may be attributed to increased overall redox activity due to the enhanced electroactive surface area[44].
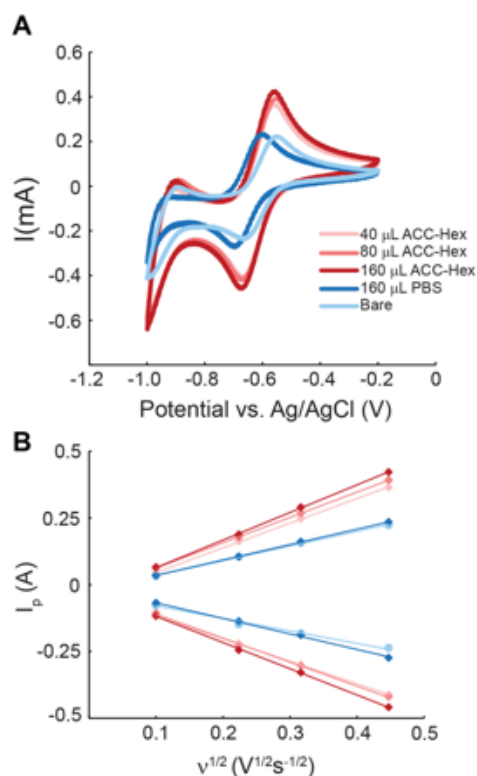
Figure 2: (A) ACC-Hex Nanofibers can be used to enhance the electroactive surface area of GCEs, as demonstrated by enhanced oxidation and reduction peaks in the presence of 1 mM methylviolagen. (B) Peak current versus scan rate show that the reversibility of the oxidation and reduction reactions are not adversely affected by the presence of ACC-Hex nanofibers.
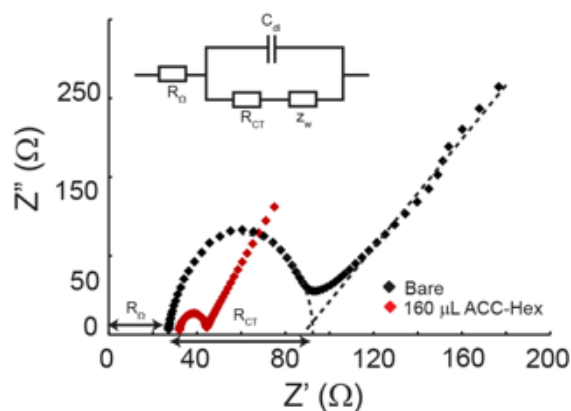

Figure 3: Electrochemical impedance spectra (Nyquist plots) of bare and modified ACC-Hex nanofiber electrodes in 0.1M KCl with 10 mM $K_3[Fe(CN)^6]$ modeled as a modified Randles circuit (inset).

### 6.3.3 Catechol Redox Reactions on Laccase-Modified Electrodes:

ACC-Hex nanofibers on GCEs were modified with laccase enzyme (*Trametes versicolor*) to demonstrate their potential as a biocompatible peptide scaffold for enzymatic electrocatalysis. Laccase (lac) belongs to a family of multicopper oxidases, having several copper ions spectroscopically distinguished as type-1 (T1), type-2 (T2), and binuclear type-3 (T3), where T2/T3 form a trinuclear cluster[45]. Lac is capable of oxidizing a range of aromatic compounds and some inorganic ions at the T1 copper site coupled to the reduction of molecular oxygen to water

99

at the T2/T3 site[46,47]. Although the active site of lac is deeply buried[48], direct electron transfer (DET) has been demonstrated to/from lac-modified electrodes[49–52]. Efficient DET depends on several factors, including the electrode material and the enzyme orientation relative to the electrode surface; namely, DET will only occur if tunneling from the active site to the electrode is both possible and more energetically favorable than alternative mediator-facilitated pathways[32,53,54].
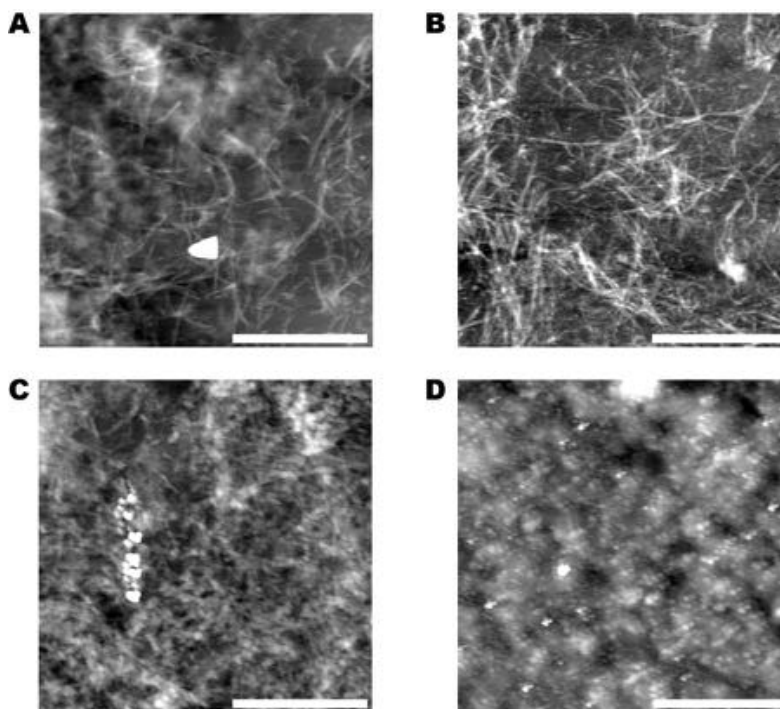

Figure 4: AFM of a single (A) and double (B) layer of ACC-Hex nanofibers and fibers with laccase before (C) and after (D) crosslinking with glutaraldehyde. Scale bars are 1 μm.

In our demonstration, we used ACC-Hex nanofibers to see if we could achieve DET between a conductive peptide scaffold to/from the enzyme. While ACC-Hex nanofibers were not designed with specific protein binding sequences, the solvent exposed Lys groups on ACC-Hex are potential crosslinking sites for enzyme immobilization via glutaraldehyde. GCEs were modified with ACC-Hex nanofiber and lac and crosslinked with glutaraldehyde (Fig. 4A-C) to create surfaces capable of electrochemical detection of phenolic compounds. In the absence of oxygen or other soluble redox mediators, GCE coated with ACC-Hex and glutaraldehyde-crosslinked lac (ACC-Hex+lac+xlink) exhibit redox peaks associated with DET between the electrode and lac (Fig. 5). The peak current is proportional to the scan rate (Fig.5, inset), confirming that this electron transfer is occurring between surface-confined, rather than diffusible, lac and the modified electrode. The slight asymmetry between the absolute oxidation and reduction current slopes (41.4 and 38.8 $\mu A \cdot s \cdot V^{-1}$, respectively) and the peak splitting with scan rate suggest that the electron transfer reaction is quasi-reversible. It may be possible to further enhance DET, improve reaction reversibility, and eliminate the need for crosslinking treatments by tuning the peptide scaffolding sequence to select for optimal enzyme orientation and attachment[18].
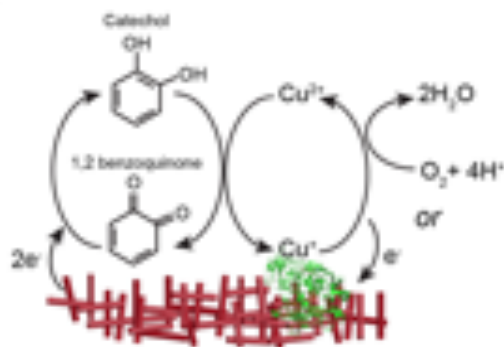
Figure 5: Scheme of proposed electron transfer mechanism of catechol oxidation and reduction in lac-ACC-Hex modified biosensor (GCE with ACC-Hex + lac + xlink), with lac either reducing the ACC-Hex modified GCE through DET or using oxygen as an electron acceptor.

Lac has been used in several biosensor applications to test for the phenolic substrate catechol[49,55,56], which is a byproduct of industrial processes and has high environmental toxicity. GCE modified with ACC-Hex and lac was tested for its ability to electrochemically detect catechol. In this configuration (Fig. 6), lac oxidizes catechol to 1,2-benzoquinone, coupled to either the reduction of molecular oxygen or through DET to the electrode surface. At reducing potentials, the 1,2-benzoquinone is subsequently reduced back to catechol through a two electron process at the modified electrode surface. Since laccase is attached to the ACC-Hex fiber scaffold through non-specific crosslinking, we expected that laccase is randomly-orientated on the conductive surface. Any DET exchange observed is therefore only sampling of the laccase with T1 metal centers localized within tunneling distances from the conductive support (i.e. within 6.5 Å for *Trametes versicolor* laccase[57]). Laccase with metal centers oriented beyond tunneling distances from the scaffold would likely transfer electrons to the T2/T3 sites and participate in native O_2 reduction instead[57].
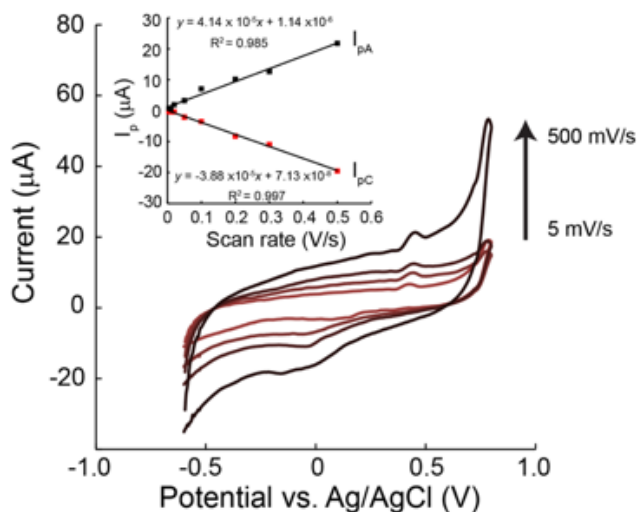
Figure 6: Cyclic voltammograms of GCE modified with ACC-Hex + lac + crosslink at different scan rates in 0.1 M phosphate buffer, pH 6.5. Peak current versus scan rate (inset).

ACC-Hex+lac+xlink modified electrodes exhibit enhanced catechol oxidation and 1,2-benzoquinone reduction peaks than controls (Fig. 7), including bare, unmodified GCE (Fig. 7A).

In the absence of lac, GCE modified with ACC-Hex only or ACC-Hex crosslinked with glutaraldehyde (ACC-Hex, ACC-Hex+xlink; Fig. 7B&C, respectively) both show limited activity towards catechol oxidation and 1,2-benzoquinone reduction. Lac alone crosslinked on the GCE surface (lac+xlink, Fig. 7D) had little redox activity under the same conditions. The reduction reaction is expected to occur non-specifically on the modified or unmodified electrode surface, irrespective of the presence of lac, as lac only catalyzes the oxidation of catechol. The greater reduction currents of the ACC-Hex+lac+xlink modified electrodes may thus attributed to the enhanced electroactive surface area of ACC-Hex electrodes and the higher concentrations of 1,2-benzoquinone produced locally at the ACC-Hex+lac+xlink surfaces.
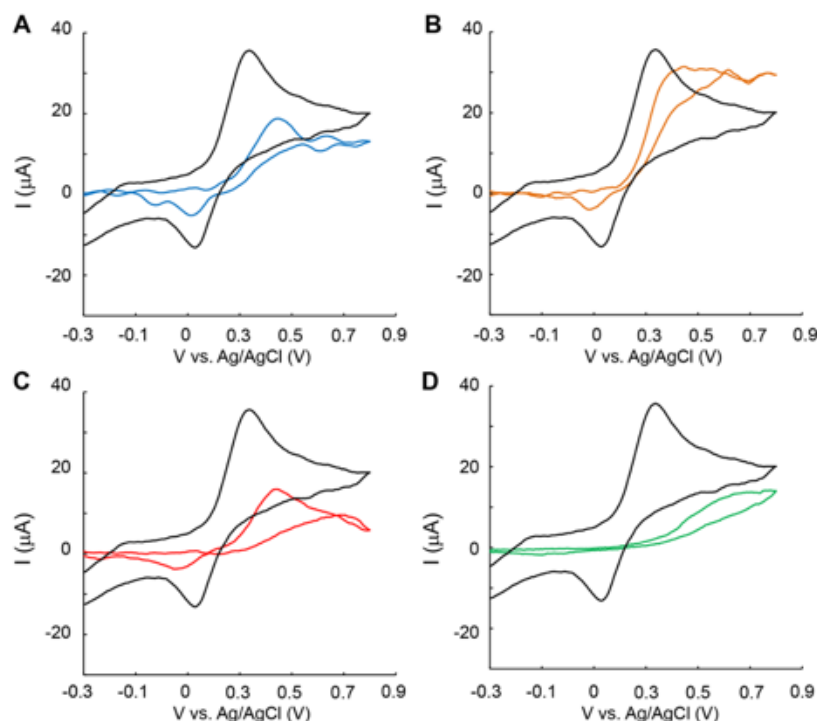

Figure 7: Background-subtracted cyclic voltammograms of GCE modified with ACC-Hex + lac + xlink (black) compared to (A) bare GCE, (B) GCE with ACC-Hex, (C) GCE with ACC-Hex + xlink, and (D) GCE with lac + xlink in 50 µM catechol, 0.1M phosphate buffer pH 6.5 at a scan rate of 50 mV/s.

Of the configurations tested, GCE modified with lac+xlink (Fig. 7D) has the smallest catechol oxidation and 1,2-benzoquinone reduction peaks. These electrodes also have wider peak splitting between reduction and oxidation peaks, suggesting that the efficiency and reversibility of catechol oxidation and reduction are adversely affected by this surface modification. Since lac is nonconductive[44,55,58], these diminished currents may be due to a reduction in the electroactive surface area of the GCE due to passivation by crosslinked lac. On the other hand, ACC-Hex + lac + xlink modified GCE has the largest oxidation and reduction currents and the least peak splitting of the electrode surfaces tested. These metrics suggest that the nanofiber support is critical to preserving the functionality of lac as well as the conductivity of the electrode surface after deposition of insulating lac. The decrease in electrocatalytic activity of the lac+xlink surface could also be a result of poor DET efficiency from unmodified GCEs[59,60], but further studies are required to support this hypothesis.

The crosslinking treatment does not significantly affect the amount of electroactive surface available. However, crosslinking may slightly enhance nonspecific 1,2-benzoquinone reduction at the ACC-Hex-modified electrode surface. The reduction peak associated with 1,2-benzquinone reduction at the ACC-Hex+lac+xlink modified GCE surface has a linear relationship with initial catechol concentration and can therefore be used to detect catechol in solution, with a minimum concentration detection of 5.3 µM (Fig. 8). This value is determined from the x-intercept of the linear fit, which has an R^2 value of 0.993. The oxidation peak associated with catechol oxidation, however, has a much higher detection limit, with linearity dropping off below 50 µM concentrations. This difference may be attributed to competing oxidation reactions, since catechol can be oxidized by both lac and the electrode surface, and because lac can be oxidized by molecular oxygen around those potentials. Conversely, 1,2-benzoquinone generated by proximal catechol oxidation is only reduced at the electrode or modified electrode surface.

$$y = -7.00 \times 10^{-7}x + 3.69 \times 10^{-7}$$
$$R^2 = 0.993$$
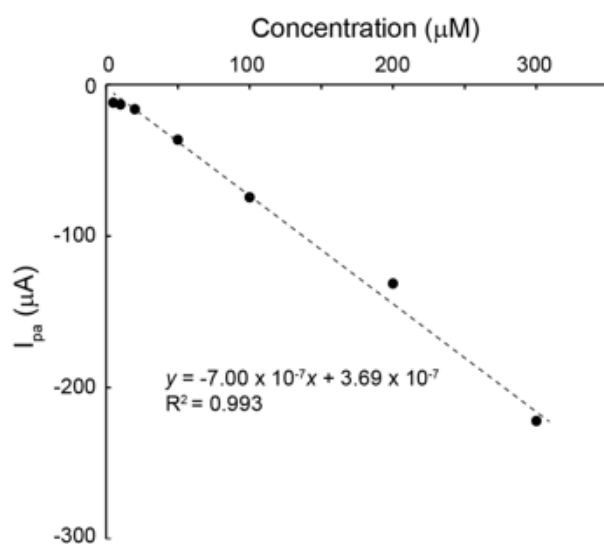
Figure 8: Calibration plot for catechol detection, based on 1,2-benzoquinone reduction at the ACC-Hex+lac+xlink modified GCE surface.

6.4 CONCLUSIONS

In this study, we characterized the electrical conductivity and electrochemical properties of ACC-Hex peptide nanofibers and demonstrated their ability to function as electroactive and enzyme-compatible bioelectronic materials. Electrochemical measurements confirm that ACC-Hex fibers conduct electronic charge and can be used to increase the electrochemically active surface area of GCEs, indicating that they are appropriate materials for enzymatic electrocatalysis applications. ACC-Hex fibers demonstrate reversibility for both single- and multi-electron redox reactions, as well as the ability to function as a conductive biomaterial scaffold for non-specific laccase immobilization. Future work will study the molecular nature of the interface between ACC-Hex fibers and redox enzymes and could include the design of solvent-exposed specific binding domains for reagent-free enzyme immobilization. Moreover, the effects of enzyme proximity and orientation on DET to/from these peptide scaffolds will help determine whether they support more efficient coupling between their biomolecular components and associated enzyme active sites. More broadly, these peptides represent a set of biological

materials that may be integrated into autonomously generated bioelectronic devices by engineered organisms.

6.5 MATERIALS AND METHODS

Peptide Material Preparation.

ACC-Hex nanofibers were prepared from synthesized peptide (Ac-ELKAIAQEFKAIAKEFKAIAFEFKAIAQK-NH$_2$)[61], as described previously[40]. Briefly, lyophilized peptide was dissolved in sterile filtered 1X PBS to a final concentration of 100 μM and seeded with a 200 μM stock concentration of pre-formed fibrilized peptide (0.5% v/v). The sample was vortexed and sonicated for 30 s each and incubated overnight at 37° C prior to use.

EIS through Peptide Films.

Interdigitated electrodes were used for impedance measurements characterizing current through the fiber network. Each electrode consisted of 100 parallel 5 μm x 2 mm long bands, with an intraband distance of 5 μm. Electrode patterns were photolithographically patterned onto Pyrex wafers and 60 nm Au and a 5 mm Ti adhesion layer were deposited by electron beam evaporation. Devices were sonicated in washes of acetone, isopropanol, and ultrapure water prior to use. 22-gauge solid core insulated wire leads were connected to the source and drain electrodes using conductive silver epoxy (MG Materials). Devices were individually tested for shorts prior to sample deposition. ACC-Hex fibers were drop cast onto cleaned electrodes to deposit a total peptide mass of 6.9 μg and were dried under vacuum. Exposed electrode and lead connections were sealed with waterproof silicone sealant (DAP All-Purpose Adhesive Sealant). Prior to use, devices were rinsed with ultrapure water to remove salts and dried with air.

Impedance measurements were conducted in ultrapure water, D$_2$O (Sigma Aldrich) or 0.1 M electrolyte buffer. Impedance was swept from 10 mHz to 100 MHz, with a fixed DC bias of 0 V and an AC perturbation of 10 mV between the source and drain electrodes. Between each measurement, the interdigitated electrode was rinsed in 2 vials of ultrapure water and dried under air flow to remove salts. The device was tested in a randomly-selected order of electrolyte solutions and then the electrolyte order was reversed. This was repeated 4 times, for a total of 8 impedance measurements per electrolyte. Impedance data was fit to a Randles circuit using Gamry software. The film resistance was taken to be the R_{CT} value from modeling.

Glassy Carbon Electrode Preparation and Determination of Electroactive Surface Area.

Glassy carbon rods (Alfa Aesar) were polished with 0.3 μm and 0.05 μm alumina polish on felt pads. GCEs were sonicated in ultrapure water for 5 minutes prior to use. After cleaning, all bare electrodes were tested in 1 mM MV, 50 mM phosphate buffer (pH 6.5) with 50 mM KCl to obtain baseline measurements of electroactive surface area via I_{pa} and Ipc. For the ACC-Hex nanofiber-modified GCEs, ACC-Hex nanofibers were deposited onto the electrode and dried under vacuum. The electrodes were manually rotated, and fibers were deposited in intervals to help promote a more even distribution of fibers on the curved electrode surface.

For determining the effect of ACC-Hex nanofibers on electroactive surface area, a single GCE was tested in 1 mM MV after every 40 μL of fiber deposition. Scans were performed in degassed solution with N$_2$ sparging, at 50 mV/s over a range of -0.2 V to -1 V vs. Ag/AgCl, with Pt wire as the counter electrode. After performing the MV test, the GCE was thoroughly rinsed in ultrapure water and dried under air before the next round of ACC-Hex nanofiber deposition. The peak oxidation (I_{pa}) and reduction (I_{pc}) currents obtained after subsequent depositions were

compared to those obtained at the bare GCE interface, and the average ratio was taken to be the percent change in electroactive surface area.

EIS of GCE.
Impedance measurements were conducted in 10 mM $[Fe(CN)_6]^{3-/4-}$ (1:1) in 0.1 M KCl, in a three electrode setup, with the GCE as the working electrode, Ag/AgCl as the reference electrode, and Pt wire as the counter electrode. Impedance was swept from 10 mHz to 100 MHz, with a fixed DC bias of -0.25 V vs Ag/AgCl and an AC perturbation of 10 mV.

Enzyme Immobilization.
Laccase from *Trametes versicolor* (Sigma) was dissolved in 0.1 M phosphate buffer pH 6.5 at a concentration of 50 mg/mL. 10 µL of enzyme solution was dropcast onto GCE modified with 160 µL of previously deposited and dried ACC-Hex nanofibers and allowed to dry overnight at 4º C. Crosslinking was performed by submerging the modified GCE in a stirred solution of 10% v/v glutaraldehyde in 0.1 M phosphate buffer pH 6.5 for 40 min at 4 ºC. After crosslinking, GCEs were rinsed in milipore to remove salts and unattached enzyme. Enzyme modified electrodes were used immediately after crosslinking.

Cyclic Voltammetry.
Cyclic voltammetry experiments were performed in 0.1 M phosphate buffer pH 6.5. Scans were swept from 0.8 V to -0.6 V vs. Ag/AgCl, using a Pt wire counter electrode, at scan rates of 5 mV/s, 10 mV/s, 20 mV/s, 50 mV/s, 100 mV/s, 200 mV/s, and 500 mV/s. CVs were collected with 0 and 50 µM catechol concentrations to obtain background-subtracted plots. Studies for catechol turnover were performed in stirred solutions. The catechol calibration plot was determined using 10, 20, 50, 100, 200, and 300 µM concentrations of catechol and measuring the I_{pc} associated with 1,2-benzoquinone reduction.

AFM Imaging.
ACC-Hex nanofibers and ACC-Hex nanofibers with enzyme were imaged on silicon wafer chips. Prior to sample deposition, wafer chips were sonicated for 5 min each in acetone, isopropanol, and ultrapure water, followed by drying under nitrogen and oxygen plasma cleaning. ACC-Hex nanofiber samples were dropcast onto freshly cleaned wafers and dried under vacuum. After drying, salts were removed through rinsing. A reduced concentration of enzyme (0.5 mg/mL) was used for AFM imaging and prepared in ultrapure water (Barnstead E-Pure). Crosslinking was performed by adding 5 µL of 10% v/v glutaraldehyde in 0.1 M phosphate buffer pH 6.5 at 4 ºC. Excess glutaraldehyde and salts were rinsed after 40 min, prior to imaging. Samples were dried in air and imaged with an Asylum MFP3D operating in tapping mode, under ambient conditions. Scans were rastered at 1Hz using iridium-coated silicon probes (Asylum Research ASYELEC.01-R2).

6.6 REFERENCES

(1) Yadav, R. K.; Baeg, J.-O.; Oh, G. H.; Park, N.-J.; Kong, K.; Kim, J.; Hwang, D. W.; Biswas, S. K. A Photocatalyst–Enzyme Coupled Artificial Photosynthesis System for Solar Energy in Production of Formic Acid from CO2. *J. Am. Chem. Soc.* **2012**, *134* (28), 11455–11461.

(2) Zhu, Z.; Tam, T. K.; Sun, F.; You, C.; Zhang, Y.-H. P. A High-Energy-Density Sugar Biobattery Based on a Synthetic Enzymatic Pathway. *Nat. Commun.* **2014**, *5*, 3026.

(3) Bandodkar, A. J.; You, J.-M.; Kim, N.-H.; Gu, Y.; Kumar, R.; Mohan, A. M. V.; Kurniawan, J.; Imani, S.; Nakagawa, T.; Parish, B.; et al. Soft, Stretchable, High Power Density Electronic Skin-Based Biofuel Cells for Scavenging Energy from Human Sweat. *Energy Environ. Sci.* **2017**, *10* (7), 1581–1589.

(4) Bornscheuer, U. T.; Huisman, G. W.; Kazlauskas, R. J.; Lutz, S.; Moore, J. C.; Robins, K. Engineering the Third Wave of Biocatalysis. *Nature* **2012**, *485* (7397), 185–194.

(5) Nature-Inspired Enzymatic Cascades to Build Valuable Compounds. *Biotechnol. Adv.* **2015**, *33* (5), 394–411.

(6) Fernandes, P. Enzymes in Food Processing: A Condensed Overview on Strategies for Better Biocatalysts. *Enzyme Res.* **2010**, *2010*.

(7) Reuel, N. F.; McAuliffe, J. C.; Becht, G. A.; Mehdizadeh, M.; Munos, J. W.; Wang, R.; Delaney, W. J. Hydrolytic Enzymes as (Bio)-Logic for Wireless and Chipless Biosensors. *ACS Sens.* **2016**, *1* (4), 348–353.

(8) Njagi, J.; Chernov, M. M.; Leiter, J. C.; Andreescu, S. Amperometric Detection of Dopamine in Vivo with an Enzyme Based Carbon Fiber Microbiosensor. *Anal. Chem.* **2010**, *82* (3), 989–996.

(9) Rocchitta, G.; Spanu, A.; Babudieri, S.; Latte, G.; Madeddu, G.; Galleri, G.; Nuvoli, S.; Bagella, P.; Demartis, M. I.; Fiore, V.; et al. Enzyme Biosensors for Biomedical Applications: Strategies for Safeguarding Analytical Performances in Biological Fluids. *Sensors* **2016**, *16* (6).

(10) Sekretaryova, A. N.; Beni, V.; Eriksson, M.; Karyakin, A. A.; Turner, A. P. F.; Vagin, M. Y. Cholesterol Self-Powered Biosensor. *Anal. Chem.* **2014**, *86* (19), 9540–9547.

(11) Goradel, N. H.; Mirzaei, H.; Sahebkar, A.; Poursadeghiyan, M.; Masoudifar, A.; Malekshahi, Z. V.; Negahdari, B. Biosensors for the Detection of Environmental and Urban Pollutions. *J. Cell. Biochem. 119* (1), 207–212.

(12) Guzik, U.; Hupert-Kocurek, K.; Wojcieszyńska, D. Immobilization as a Strategy for Improving Enzyme Properties-Application to Oxidoreductases. *Mol. Basel Switz.* **2014**, *19* (7), 8995–9018.

(13) Rodrigues, R. C.; Ortiz, C.; Berenguer-Murcia, Á.; Torres, R.; Fernández-Lafuente, R. Modifying Enzyme Activity and Selectivity by Immobilization. *Chem. Soc. Rev.* **2013**, *42* (15), 6290–6307.

(14) Truppo, M. D.; Strotman, H.; Hughes, G. Development of an Immobilized Transaminase Capable of Operating in Organic Solvent. *ChemCatChem* **2012**, *4* (8), 1071–1074.

(15) Li, H.; Moncecchi, J.; Truppo, M. D. Development of an Immobilized Ketoreductase for Enzymatic (R)-1-(3,5-Bis(Trifluoromethyl)Phenyl)Ethanol Production. *Org. Process Res. Dev.* **2015**, *19* (7), 695–700.

(16) Hoarau, M.; Badieyan, S.; Marsh, E. N. G. Immobilized Enzymes: Understanding Enzyme – Surface Interactions at the Molecular Level. *Org. Biomol. Chem.* **2017**, *15* (45), 9539–9551.

(17) Spicer, C. D.; Davis, B. G. Selective Chemical Protein Modification. *Nat. Commun.* **2014**, *5*, 4740. https://doi.org/10.1038/ncomms5740.

(18) Fu, J.; Reinhold, J.; Woodbury, N. W. Peptide-Modified Surfaces for Enzyme Immobilization. *PLOS ONE* **2011**, *6* (4), e18692.

(19) Fodor, S. P.; Read, J. L.; Pirrung, M. C.; Stryer, L.; Lu, A. T.; Solas, D. Light-Directed, Spatially Addressable Parallel Chemical Synthesis. *Science* **1991**, *251* (4995), 767–773.

(20) Pang, Y.; Liu, J.; Qi, Y.; Li, X.; Chilkoti, A. A Modular Method for High Yield Synthesis of Site-Specific Protein–Polymer Therapeutics. *Angew. Chem. Int. Ed Engl.* **2016**, *55* (35), 10296–10300.

(21) Panda, J. J.; Chauhan, V. S. Short Peptide Based Self-Assembled Nanostructures: Implications in Drug Delivery and Tissue Engineering. *Polym. Chem.* **2014**, *5* (15), 4418–4436.

(22) Matson, J. B.; Zha, R. H.; Stupp, S. I. Peptide Self-Assembly for Crafting Functional Biological Materials. *Curr. Opin. Solid State Mater. Sci.* **2011**, *15* (6), 225–235.

(23) Santis, E. D.; Ryadnov, M. G. Peptide Self-Assembly for Nanomaterials: The Old New Kid on the Block. *Chem. Soc. Rev.* **2015**, *44* (22), 8288–8300.

(24) Barbosa, O.; Torres, R.; Ortiz, C.; Berenguer-Murcia, Á.; Rodrigues, R. C.; Fernandez-Lafuente, R. Heterofunctional Supports in Enzyme Immobilization: From Traditional Immobilization Protocols to Opportunities in Tuning Enzyme Properties. *Biomacromolecules* **2013**, *14* (8), 2433–2462.

(25) Koch-Schmidt, A.-C. Gel-Entrapment of Enzymes. In *Biomedical Applications of Immobilized Enzymes and Proteins*; Springer, Boston, MA, 1977; pp 47–67.

(26) Garcia, K. E.; Babanova, S.; Scheffler, W.; Hans, M.; Baker, D.; Atanassov, P.; Banta, S. Designed Protein Aggregates Entrapping Carbon Nanotubes for Bioelectrochemical Oxygen Reduction. *Biotechnol. Bioeng.* **2016**, *113* (11), 2321–2327.

(27) Care, A.; Petroll, K.; Gibson, E. S. Y.; Bergquist, P. L.; Sunna, A. Solid-Binding Peptides for Immobilisation of Thermostable Enzymes to Hydrolyse Biomass Polysaccharides. *Biotechnol. Biofuels* **2017**, *10* (1), 29.

(28) Care, A.; Bergquist, P. L.; Sunna, A. Solid-Binding Peptides: Smart Tools for Nanobiotechnology. *Trends Biotechnol.* **2015**, *33* (5), 259–268.

(29) Gupta, G.; Rajendran, V.; Atanassov, P. Laccase Biosensor on Monolayer-Modified Gold Electrode. *Electroanalysis* **2003**, *15* (20), 1577–1583.

(30) Vaz-Dominguez, C.; Campuzano, S.; Rüdiger, O.; Pita, M.; Gorbacheva, M.; Shleev, S.; Fernandez, V. M.; De Lacey, A. L. Laccase Electrode for Direct Electrocatalytic Reduction of O2 to H2O with High-Operational Stability and Resistance to Chloride Inhibition. *Biosens. Bioelectron.* **2008**, *24* (4), 531–537.

(31) Guan, D.; Kurra, Y.; Liu, W.; Chen, Z. A Click Chemistry Approach to Site-Specific Immobilization of a Small Laccase Enables Efficient Direct Electron Transfer in a Biocathode. *Chem. Commun.* **2015**, *51* (13), 2522–2525.

(32) Milton, R. D.; Minteer, S. D. Direct Enzymatic Bioelectrocatalysis: Differentiating between Myth and Reality. *J. R. Soc. Interface* **2017**, *14* (131).]

(33) Recent Advances on Developing 3rd Generation Enzyme Electrode for Biosensor Applications. *Biosens. Bioelectron.* **2016**, *79*, 386–397.

(34) Direct Electron Transfer between Heme-Containing Enzymes and Electrodes as Basis for Third Generation Biosensors. *Anal. Chim. Acta* **1999**, *400* (1–3), 91–108.

(35) Hickling, C.; Toogood, H. S.; Saiani, A.; Scrutton, N. S.; Miller, A. F. Nanofibrillar Peptide Hydrogels for the Immobilization of Biocatalysts for Chemical Transformations. *Macromol. Rapid Commun.* **2014**, *35* (9), 868–874.

(36) Yang, H.; Fung, S.-Y.; Pritzker, M.; Chen, P. Ionic-Complementary Peptide Matrix for Enzyme Immobilization and Biomolecular Sensing. *Langmuir* **2009**, *25* (14), 7773–7777.

(37) Lee, Y. S.; Baek, S.; Lee, H.; Reginald, S. S.; Kim, Y.; Kang, H.; Choi, I.-G.; Chang, I. S. Construction of Uniform Monolayer- and Orientation-Tunable Enzyme Electrode by a Synthetic Glucose Dehydrogenase without Electron-Transfer Subunit via Optimized Site-Specific Gold-Binding Peptide Capable of Direct Electron Transfer. *ACS Appl. Mater. Interfaces* **2018**, *10* (34), 28615–28626.

(38) Amir, L.; Carnally, S. A.; Rayo, J.; Rosenne, S.; Melamed Yerushalmi, S.; Schlesinger, O.; Meijler, M. M.; Alfonta, L. Surface Display of a Redox Enzyme and Its Site-Specific Wiring to Gold Electrodes. *J. Am. Chem. Soc.* **2013**, *135* (1), 70–73.

(39) Du, S.; Lazareck, A.; Kim, J. H.; Xu, J.; Yeh, J. I. Peptide Nanowires for Coordination and Signal Transduction of Peroxidase Biosensors to Carbon Nanotube Electrode Arrays. *Biosens. Bioelectron.* **2007**, *23* (4), 568–574.

(40) Ing, N. L.; Spencer, R. K.; Luong, S. H.; Nguyen, H. D.; Hochbaum, A. I. Electronic Conductivity in Biomimetic α-Helical Peptide Nanofibers and Gels. *ACS Nano* **2018**, *12* (3), 2652–2661.

(41) Hofmeister, F. Zur Lehre von der Wirkung der Salze. *Arch. Für Exp. Pathol. Pharmakol.* **1888**, *24* (4–5), 247–260. https://doi.org/10.1007/BF01918191.

(42) Hofmeister, F. Zur Lehre von der Wirkung der Salze. *Arch. Für Exp. Pathol. Pharmakol.* **1888**, *25* (1), 1–30.

(43) Tadeo, X.; López-Méndez, B.; Castaño, D.; Trigueros, T.; Millet, O. Protein Stabilization and the Hofmeister Effect: The Role of Hydrophobic Solvation. *Biophys. J.* **2009**, *97* (9), 2595–2603.

(44) Alarcón, G.; Guix, M.; Ambrosi, A.; Ramirez Silva, M. T.; Palomar Pardave, M. E.; Merkoçi, A. Stable and Sensitive Flow-through Monitoring of Phenol Using a Carbon Nanotube Based Screen Printed Biosensor. *Nanotechnology* **2010**, *21* (24), 245502.

(45) Jones, S. M.; Solomon, E. I. Electron Transfer and Reaction Mechanism of Laccases. *Cell. Mol. Life Sci. CMLS* **2015**, *72* (5), 869–883.

(46) Shleev, S.; Tkac, J.; Christenson, A.; Ruzgas, T.; Yaropolov, A. I.; Whittaker, J. W.; Gorton, L. Direct Electron Transfer between Copper-Containing Proteins and Electrodes. *Biosens. Bioelectron.* **2005**, *20* (12), 2517–2554.

(47) Solomon, E. I.; Baldwin, M. J.; Lowery, M. D. Electronic Structures of Active Sites in Copper Proteins: Contributions to Reactivity. *Chem. Rev.* **1992**, *92* (4), 521–542.

(48) Piontek, K.; Antorini, M.; Choinowski, T. Crystal Structure of a Laccase from the Fungus Trametes Versicolor at 1.90-A Resolution Containing a Full Complement of Coppers. *J. Biol. Chem.* **2002**, *277* (40), 37663–37669.

(49) Palanisamy, S.; Ramaraj, S. K.; Chen, S.-M.; Yang, T. C. K.; Yi-Fan, P.; Chen, T.-W.; Velusamy, V.; Selvam, S. A Novel Laccase Biosensor Based on Laccase Immobilized Graphene-Cellulose Microfiber Composite Modified Screen-Printed Carbon Electrode for Sensitive Determination of Catechol. *Sci. Rep.* **2017**, *7*, 41214.

(50) Meredith, M. T.; Minson, M.; Hickey, D.; Artyushkova, K.; Glatzhofer, D. T.; Minteer, S. D. Anthracene-Modified Multi-Walled Carbon Nanotubes as Direct Electron Transfer Scaffolds for Enzymatic Oxygen Reduction. *ACS Catal.* **2011**, *1* (12), 1683–1690.

(51) Direct Electron Transfer Reactions of Laccases from Different Origins on Carbon Electrodes. *Bioelectrochemistry* **2005**, *67* (1), 115–124.

(52) Wang, X.; Latonen, R.-M.; Sjöberg-Eerola, P.; Eriksson, J.-E.; Bobacka, J.; Boer, H.; Bergelin, M. Direct Electron Transfer of Trametes Hirsuta Laccase in a Dual-Layer Architecture of Poly(3,4-Ethylenedioxythiophene) Films. *J. Phys. Chem. C* **2011**, *115* (13), 5919–5929.

(53) Ivnitski, D. M.; Khripin, C.; Luckarift, H. R.; Johnson, G. R.; Atanassov, P. Surface Characterization and Direct Bioelectrocatalysis of Multicopper Oxidases. *Electrochimica Acta* **2010**, *55* (24), 7385–7393.

(54) Babanova, S.; Matanovic, I.; Chavez, M. S.; Atanassov, P. Role of Quinones in Electron Transfer of PQQ–Glucose Dehydrogenase Anodes—Mediation or Orientation Effect. *J. Am. Chem. Soc.* **2015**, *137* (24), 7754–7762.

(55) Qu, J.; Lou, T.; Wang, Y.; Dong, Y.; Xing, H. Determination of Catechol by a Novel Laccase Biosensor Based on Zinc-Oxide Sol-Gel. *Anal. Lett.* **2015**, *48* (12), 1842–1853.

(56) Rodríguez-Delgado, M. M.; Alemán-Nava, G. S.; Rodríguez-Delgado, J. M.; Dieck-Assad, G.; Martínez-Chapa, S. O.; Barceló, D.; Parra, R. Laccase-Based Biosensors for Detection of Phenolic Compounds. *TrAC Trends Anal. Chem.* **2015**, *74*, 21–45.

(57) Ulyanova, Y.; Babanova, S.; Pinchon, E.; Matanovic, I.; Singhal, S.; Atanassov, P. Effect of Enzymatic Orientation through the Use of Syringaldazine Molecules on Multiple Multi-Copper Oxidase Enzymes. *Phys. Chem. Chem. Phys.* **2014**, *16* (26), 13367–13375.

(58) Chawla, S.; Rawal, R.; Kumar, D.; Pundir, C. S. Amperometric Determination of Total Phenolic Content in Wine by Laccase Immobilized onto Silver Nanoparticles/Zinc Oxide Nanoparticles Modified Gold Electrode. *Anal. Biochem.* **2012**, *430* (1), 16–23.

(59) Liu, Y.; Zhang, J.; Cheng, Y.; Jiang, S. P. Effect of Carbon Nanotubes on Direct Electron Transfer and Electrocatalytic Activity of Immobilized Glucose Oxidase. *ACS Omega* **2018**, *3* (1), 667–676.

(60) Oztekin, Y.; Ramanaviciene, A.; Yazicigil, Z.; Solak, A. O.; Ramanavicius, A. Direct Electron Transfer from Glucose Oxidase Immobilized on Polyphenanthroline-Modified Glassy Carbon Electrode. *Biosens. Bioelectron.* **2011**, *26* (5), 2541–2546.

(61) Spencer, R. K.; Hochbaum, A. I. X-Ray Crystallographic Structure and Solution Behavior of an Antiparallel Coiled-Coil Hexamer Formed by de Novo Peptides. *Biochem.* **2016**, *55* (23), 3214–3223.

CHAPTER 7

Collaborations and Transitions

Prof. Rein Ulijn (CUNY-ASRC): Dynamic electronic characterization of "living" assembly/disassembly conjugated organic-oligopeptide gels. This project studies the structural and electronic property dynamics of active and dissipative assembly materials composed of semiconducting small molecules conjugated to short peptide sequences. Enzymatic reactions at the flanking amino acids result in changes in polarity that drive self-assembly of conductive nanostructures. We use methods for electronic and electrochemical characterization of hydrated biomaterials to track structural changes via changes in material conductivity. These materials are targeted at transient electronic interfaces for neuronal stimulation. This collaboration has yielded one publication to date and is now funded by NSF-CHE Macromolecular, Supramolecular and Nanochemistry program.

Dr. Ron Zuckermann (Director, Biological Nanostructures Facility, Molecular Foundry, LBNL): Electrical conductivity measurements and structure modeling of peptoid nanostructures. Peptoids are peptide-mimetic polymers with similar defined side chain chemistry and secondary structure. We measure conductivity of aromatic containing peptoids and molecular dynamics modeling techniques employed in the lab have been used to help understand the formation of secondary structure in supramolecular peptoid materials. This collaboration has yielded one publication to date.

Prof. Ed Egelman (UVA): Cryo-electron microscopy of protein and peptide nanofibers. Our collaboration with Prof. Egelman focuses on developing structure-property relationships in conductive biological materials. Cryo-EM is uniquely suited to determine the atomic-scale structure of protein and peptide supramolecular fibers because these materials are too high molecular weight to crystallize for conventional X-ray crystallographic structure insight. The Egelman lab uses cryo-EM to elucidate structural features of our synthetic peptide fibers and of native conductive protein fibers isolated from bacteria and targeted mutant strains. This collaboration has produced one publication and the native protein fiber work is now supported by DOE-BES Physical Biosciences program.

Prof. Ehud Gazit (University of Tel Aviv): Electron transport in self-assembled oligopeptide nanostructures. The Gazit lab designs short peptides that self-assemble into molecularly ordered nanostructures with inherent conductivity or with directing groups for the assembly or precipitation of conductive materials. We use methods developed as part of the present AFOSR project to characterize the electronic and electrostatic properties of these materials for bioinspired electronics applications. This collaboration has produced one paper to date.

Prof. Doug Clark (UC Berkeley) & Prof. Dominic Glover (UNSW Sydney): Electorchemical and transport measurements of self-assembled cytochrome fibers. γ-prefoldin (gPFD), from a thermophilic archeon, self-assembles into molecular wires hundreds of nm in length. The Clark and Glover lab have engineered the protein to direct the assembly of c-type cytochromes along the fiber axis. We characterize the electrochemical and electron transport properties of these engineered cytochrome wires with an eye towards biogenic synthesis of conductive biological

circuit components. One manuscript has been recently submitted on this collaborative project, which also includes structural studies by cryo-EM from Prof. Ed Egelman's lab.

Other collaborations and scientific transitions: We have collaborated on molecular dynamics simulations of peptide self-assembly with Prof. Hung Nguyen (UC Irvine), which resulted in one publication. We work with Dr. Ich Tran (Surface Characterization Facility, UC Irvine) to do X-ray photoelectron spectroscopy measurements of peptide crystals for band gap determination. We have conducted peptide oligomer monolayer conductance measurements with our conductive peptides in collaboration with Prof. David Cahen (Weizmann Institute of Science, Israel). We developed a general method for high-throughput size exclusion chromatography-small-angle X-ray scattering for soluble aggregate structure insights in collaboration with Dr. Greg Hura (Advanced Light Source, LBNL).

CHAPTER 8

Publications and Patents

Publications from work supported by the present award:

9. Wang, F., Gu, Y., O'Brien, J.P., Yi, S.M., Yalcin, S.E., Srikanth, V., Shen, C., Vu, D., Ing, N.L., **Hochbaum, A.I.***, Egelman, E.H.*, Malvankar, N.S.* (2019) Structure of microbial nanowires reveals stacked hemes that transport electrons over micrometers. *Cell*, *177*, 361-369.
^Featured in Nature Chemical Biology, New York Times

8. Guterman, T., Ing, N.L., Fleischer, S., Rehak, P., Basavalingappa, V., Hunashal, Y., Dongre, R., Raghothama, S., Král, P., Dvir, T., **Hochbaum, A.I.**, Gazit, E.* (2019) Electrical conductivity, selective adhesion, and biocompatibility in bacterial-inspired peptide-metal self-supporting nanocomposites. *Adv. Mater.*, *31*, 1807285.

7. Ing, N.L., El-Naggar, M.Y., **Hochbaum, A.I.*** (2018) Going the distance: long-range conductivity in protein and peptide bioelectronic materials (Review Article). *J. Phys. Chem. B*, *122*, 10403.
^ACS Editor's Choice Article

6. Edison, J.R., Spencer, R.K., Butterfoss, G.L., Hudson, B., **Hochbaum, A.I.**, Paravastu, A.K., Zuckermann, R.N., Whitelam, S.* (2018) Conformations of peptoids in nano sheets result from the interplay of backbone energetics and intermolecular interactions. *Proc. Natl. Acad. Sci. USA*, *115*, 5647.

5. Kumar, M., Ing, N.L., Narang, V., Wijerathne, N., **Hochbaum, A.I.**, Ulijn, R.V.* (2018) Amino Acid-Encoded Biocatalytic Self-Assembly Enables the Formation of Transient Conducting Nanostructures. *Nat. Chem.*, *10*, 696.

4. Ing, N. L., Spencer, R. K., Luong, S. H., Nguyen, H. D., **Hochbaum, A.I.*** (2018) Electrical Conductivity in Biomimetic a-Helical Peptide Nanofibers and Gels. *ACS Nano*, *12*, 2652.

3. Spencer, R.K., **Hochbaum, A.I.*** (2017) The Phe-Ile Zipper: A Specific Interaction Motif Drives Antiparallel Coiled-Coil Hexamer Formation. *Biochemistry*, *56*, 5300.

2. Ing, N.L., Nusca, T.D., **Hochbaum, A.I.*** (2017) *Geobacter sulfurreducens* Pili Support Ohmic Electronic Transport in Aqueous Solution. *Phys. Chem. Chem. Phys.*, *19*, 21791.

1. Spencer, R.K., **Hochbaum, A.I.*** (2016) X-Ray Crystallographic Structure and Solution Behavior of an Antiparallel Coiled Coil Hexamer Formed by *de Novo* Peptides. *Biochemistry*, *55*, 3214.

Patents from work supported by the present award:
None

CHAPTER 9

Presentations and Awards

Invited presentations on work supported by this award:

06/2019 **Gordon Research Conference**, Bioelectronics, Proctor Academy, Andover, NH.
04/2019 **Boston University**, Biological Physics, Boston, MA.
04/2019 **University of Massachusetts, Amherst**, Institute for Applied Life Sciences, Amherst, MA.
04/2019 **Massachusetts Institute of Technology**, Program in Polymers and Soft Matter, Cambridge, MA.
03/2019 **Institute for Atomic and Molecular Physics (AMOLF)**, Amsterdam, Netherlands.
03/2019 **Electromicrobiology,** Aarhus University, Denmark. (keynote speaker).
10/2018 **International Society for Microbial Electrochemistry and Technology** –North American meeting, University of Minnesota. St. Paul, MN.
09/2018 **California State University Los Angeles,** Department of Chemistry, Los Angeles, CA.
08/2018 **SPIE, international society for optics and photonics**, Optics + Photonics: Organic and Hybrid Sensor and Bioelectronics, San Diego, CA.
07/2018 **University of Fribourg**, Adolph Merkel Institute, Fribourg, Switzerland.
02/2018 **Emory University,** Department of Chemistry, Atlanta, GA.
11/2017 **University of Southern California,** Department of Materials Science and Engineering.
09/2017 **Asilomar Bioelectronics Symposium**, Pacific Grove, CA.
04/2017 **Washington University in St. Louis**, Institute of Materials Science and Engineering, St. Louis, MO.
03/2017 **California State University, Long Beach,** Department of Physics, Long Beach, CA.
11/2016 **University of California, San Diego,** Department of Nanoengineering.
11/2016 **City University of New York**, Advanced Science Research Center, New York, NY.
10/2016 **International Society for Microbial Electrochemistry and Technology** – 3rd North American meeting, Stanford University, Stanford, CA.
09/2016 **University of Tel Aviv**, Department of Molecular Microbiology and Biotechnology**,** Tel Aviv, Israel.
09/2016 **Weizmann Institute of Science**, Department of Materials and Interfaces, Rehovot, Israel.
08/2016 **American Chemical Society**, National Meeting, Philadelphia, PA.
04/2016 **Lawrence Berkeley National Laboratory**, Molecular Foundry, Berkeley, CA.
02/2016 **Army Research Laboratory**, Adelphi, MD.
12/2015 **Materials Research Society**, Fall Meeting, Boston, MA.

Contributed presentations and posters on work supported by this award:

08/2018 **BASF North American Research Forum**, Iselin, NJ.
06/2018 **Gordon Research Conference**, Bioinspired Materials, Les Diableret, Switzerland.
03/2018 **American Chemical Society**, Spring National Meeting, COLL: Fundamental Research in Colloids, Surfaces & Nanomaterials, New Orleans, LA.

02/2018 **Gordon Research Conference**, Chemistry and Biology of Peptides, Ventura, CA.
08/2017 **10th Peptoid Summit**, Lawrence Berkeley National Lab, Berkeley, CA.
11/2016 **Materials Research Society** Fall Meeting, Symposium BM6: Fabrication, Characterization and Applications of Bioinspired Nanostructured Materials, Boston, MA.
10/2016 **Advanced Light Source User Meeting**, Lawrence Berkeley National Lab, Berkeley, CA.
08/2016 **Molecular Foundry User Meeting**, Lawrence Berkeley National Lab, Berkeley, CA.

Awards on work supported by this award:
None